NOAA Technical Memorandum ERL AOML-67

JOINT CGS-AOML ACOUSTICAL BOTTOM ECHO-FORMATION RESEARCH II: FIELD EXPERIMENT RESULTS AND RECOMMENDATIONS FOR ECHO-SOUNDER DESIGN

Thomas L. Clarke
John R. Proni
Lloyd C. Huff

Atlantic Oceanographic and Meteorological Laboratory
Miami, Florida
July 1988

NOAA Technical Memorandum ERL AOML-67

JOINT CGS-AOML ACOUSTICAL BOTTOM ECHO-FORMATION RESEARCH II: FIELD EXPERIMENT RESULTS AND RECOMMENDATIONS FOR ECHO-SOUNDER DESIGN

Thomas L. Clarke
John R. Proni
Lloyd C. Huff

Atlantic Oceanographic and Meteorological Laboratory
Miami, Florida
July 1988

UNITED STATES
DEPARTMENT OF COMMERCE

C.William Verity
Secretary

NATIONAL OCEANIC AND
ATMOSPHERIC ADMINISTRATION

William E. Evans
Under Secretary for Oceans
and Atmosphere/Administrator

Environmental Research
Laboratories

Vernon E. Derr,
Director

NOTICE

Mention of a commercial company or product does not constitute an endorsement by NOAA Environmental Research Laboratories. Use for publicity or advertising purposes of information from this publication concerning proprietary products or the tests of such products is not authorized.

For sale by the National Technical Information Service, 5285 Port Royal Road
Springfield, VA 22161

TABLE OF CONTENTS

LIST OF FIGURES

LIST OF FIGURES (continued)

ABSTRACT

Field experiments were conducted to test and verify a mathematical model that has been developed to assess the effects of bottom roughness and material properties on bottom echo shape. The physical basis of the model is reviewed and model output is presented.

The experiments were conducted in lower Chesapeake Bay and involved taking high resolution acoustic data at a number of frequencies and taking supporting sediment samples. A unique, high resolution bottom profiler was used to measure bottom roughness profiles for input to the model. While model predictions were in general agreement with the data, fine structure was observed in the echoes that could not be explained by the existing model.

An extension to the model has been developed that is able to account for this structure. The essential ingredient of this extension is to consider bottom surface scattering as arising from a number of statistically independent patches within the transducer beam. This revised model should lead to improved predictions of bottom echo waveforms for echo-sounder design.

The algorithm developed for removing ship motion from the observations suggests a design for a new type of echo-sounder detector circuit based on an energy threshold. This circuit could be easily implemented with modern digital signal processing (DSP) circuits, and it might be suitable for retro-fitting to existing echo-sounders.

INTRODUCTION

In 1985 a joint program to improve the science of acoustic echo sounding was established between the Charting and Geodetic Services (C&GS) branch of the NOS, then under the direction of Admiral Bossler, and the Ocean Acoustics Division (OAD) of Atlantic Oceanographic and Meteorological Laboratory under the direction of Dr. Hugo Bezdek.

This program was a combination of theory and experiment designed to better define the nature of acoustic echoes from typical ocean bottoms. A better understanding of these echoes would lead to design of better performing echo sounders for use in operational charting.

The additional possibility of extracting useful bottom information from reflected acoustic pulse waveforms has been demonstrated by many experimenters. Dodds (1984) bases bottom type discrimination on analysis of frequencies in the range 1 to 10 kHz generated by an impulsive sound source. Meng and Guan (1984) utilize higher frequencies in the 100 kHz range to establish statistical discriminators. Reliable discrimination in this higher range offers the possibility of adding remote acoustical bottom characterization to a conventional echo-sounder.

The ability to remotely determine bottom types acoustically depends on the acoustical properties of the sediments. That is, the bulk sound speed, the bulk attenuation, and the bulk scattering properties are the crucial factors in echo formation. While the acoustic properties have intrinsic interest for many applications, the navigationally significant quantities are mechanical such as shear strength. It is the mechanical properties that determine the ability of the bottom to impede the motion of shipping. Fortunately, marine sediments tend to form a one-dimensional continuum (Bachman, 1985), that is, acoustic properties correlate with sediment type which is in turn correlated with mechanical properties. Thus, measurements of

bulk acoustic properties provide a means to effectively estimate the strength of sediments.

OLD THEORY

A convenient mathematical model has been developed (Clarke et al., 1985) to assess the effects of bottom characteristics such as surface roughness and material properties on bottom echo shape. This model incorporates the effects of scattering from surface roughness, and of volume scattering from within the volume of the sediment.

Standard echo-sounding geometry is assumed. The acoustic transducer which emits sound of wavelength λ is located distance R (the depth) from the sea bed. The bulk acoustic properties of the sea bed enter the model through the bulk reflection coefficient $\mathcal{R}$ for sound incident on the bed from water. The roughness of the bed is described by an RMS height variation η and a correlation length L. This statistical roughness reduces the magnitude of the coherent bottom echo component and scatters energy into a reverberant tail whose decay time is determined by a combination of sea-bed slope, η/L, depth R, and transducer beam angle. The coherent echo reduction factor is $\exp(-\phi^2)$ where $\phi = 4\pi/\lambda$ is the nondimensionalized surface roughness. For roughness much greater than a wavelength, $\phi >> 1$, almost all the echo energy is reverberant.

Figure 2 shows the model results in the form of contour plots of acoustic intensity versus time and frequency. Time is measured in milliseconds from the first echo return. The case shown is for a sandy bottom (400 μ diameter) and for $\eta = 1$ cm and $L = 10$ cm. These parameters would correspond to a gently rippled bottom. For low frequencies less than 20 kHz, the .2 msec transmitted waveform is mirrored in the contours of the echo waveform. The

Echo Sounding Geometry Assumed in Model

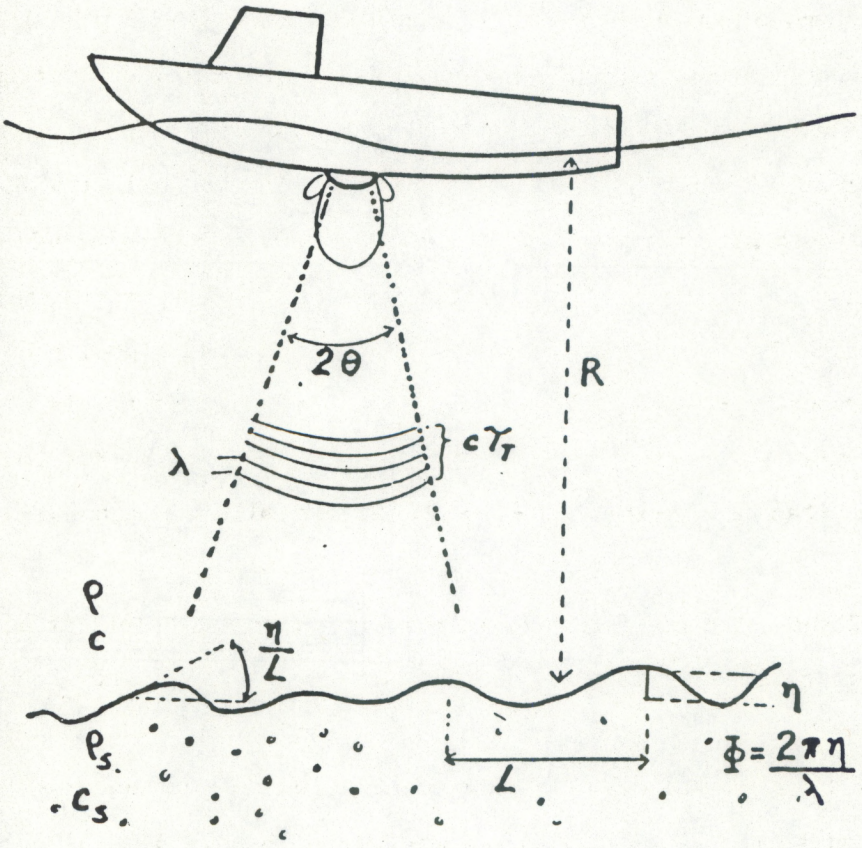

Figure 1. Drawing defining quantities in bottom echo formation model.

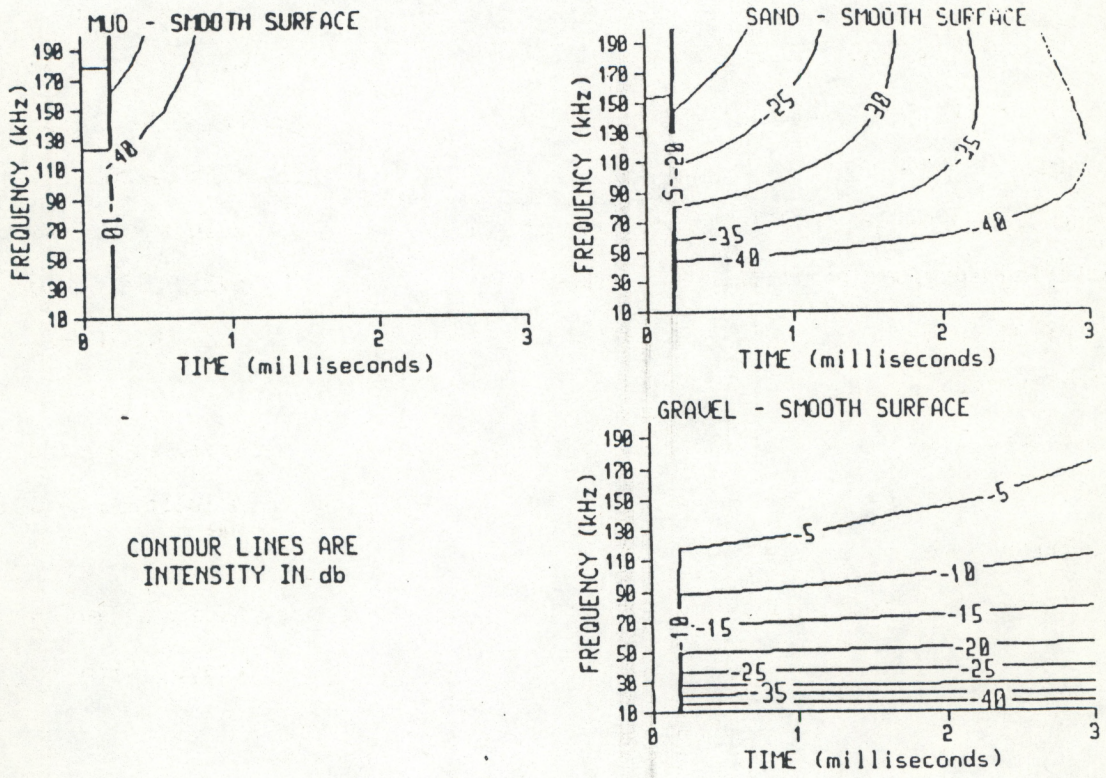

Figure 2. Contour plots of acoustic intensity predicted by OAD model.

mirrored pulse rapidly diminishes above 20 kHz as ϕ increases, and the echo becomes a reverberant tail approximately 1 msec long.

The fraction $(1-\mathcal{R}_-)$ of sound that penetrates the sea bed is scattered from the granularity of the sediment and is also rapidly absorbed by viscous losses (Biot absorption). The sound scattered from beneath the sea bed is highly frequency dependent. The QAD model uses Rayleigh theory which predicts a fourth power dependence on frequency for the sediment scattering. Empirical values are used for the Biot absorption. The results can be visualized from Figure 2. In case the sea bed is smooth, e.g., η = 1 mm, then the echo for 200 μ sand is very similar to that for a rough surface as shown in Figure 1. For both sand and 20 μ mud, the mirrored transmitted pulse is visible at all frequencies for both sediments and only drops off a little at 200 kHz; surface scattering effects are negligible at all but the highest frequencies. The big differences between the two sediments are in the volume scattering reverberant tails. The granularity of the sand produces a large scattering tail. It is this tail that is the basis for discrimination of bottom types.

Figure 3 shows the major portions of the echo waveform as related to the model. The rectangular mirror image of the transmitted pulse is followed by a reverberant tail.

This reverberant tail is made up of two components, a surface scattering component with relative amplitude $\mathcal{R}_-(1-\exp(-\phi^2))$ which decays with a characteristic time

$$\tau_s = (\eta/L)^2 \, R/2c. \qquad (1)$$

The characteristic decay time is determined only by the geometry of the propagation through the water depth, and surface slope, and is thus

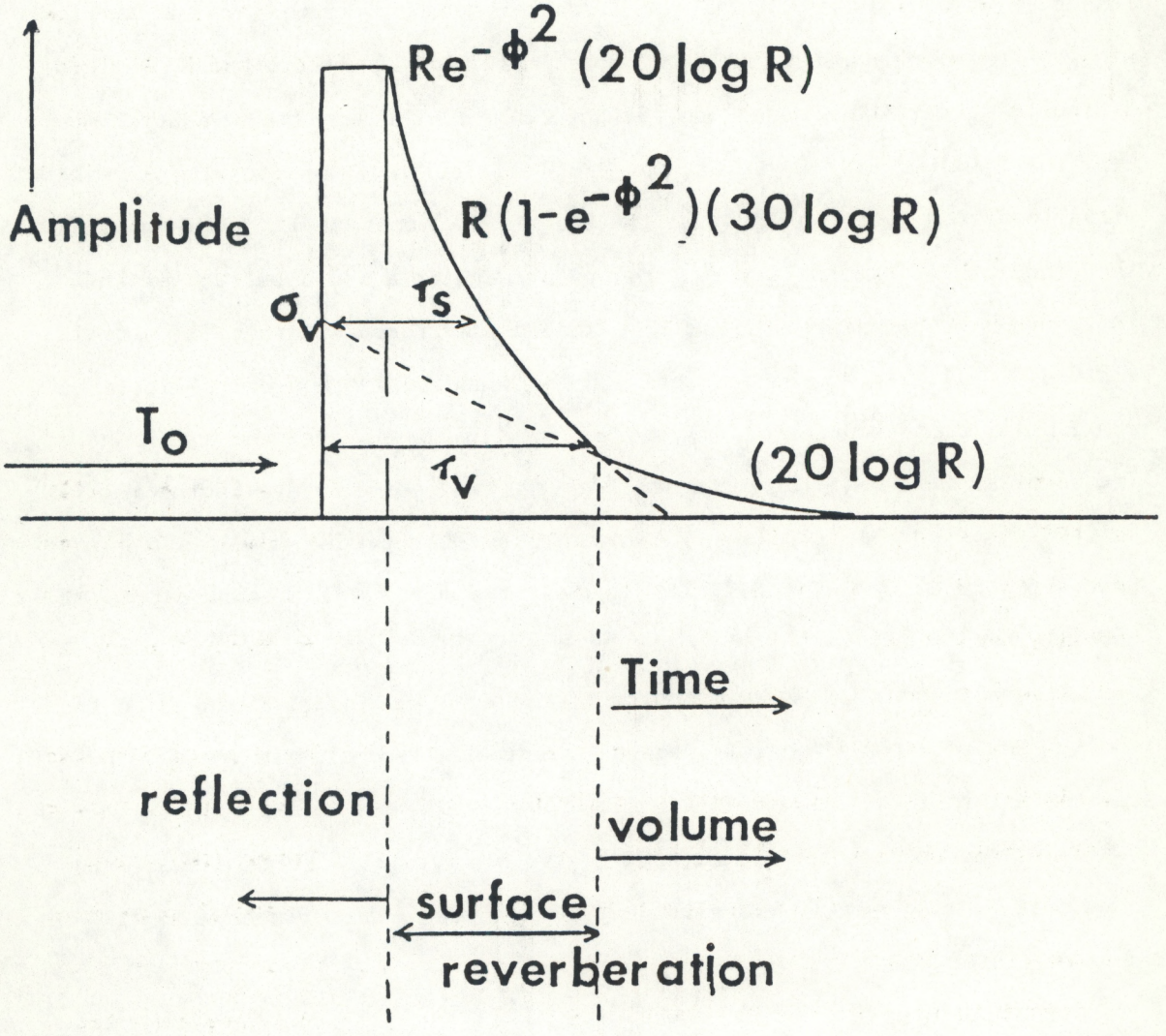

Figure 3. Major components of waveform as identified in the OAD echo formation model.

essentially frequency independent. Additionally, the decay time can be influenced by the transducer beam pattern. See (Clarke and Proni, 1986) for details.

The sound that penetrated the bottom gives rise to the volume scattering tail which has a characteristic decay time τ_s which is determined by the Biot characteristics of the sediment. This component is highly frequency dependent due to variation of absorption and scattering with frequency. The field experiment of the summer of 1986 was designed to test the validity of the model and to determine the feasibility of separating these two reverberant components by using transmissions at multiple frequencies.

EXPERIMENT EQUIPMENT

During the field experiment in the Chesapeake, echo data from a variety of bottoms at a wide range of frequencies was taken. This data was digitized and recorded on floppy disks. These disks have been read here in AOML and the quality of the data confirmed. Analysis of bottom sediment samples taken at the time has been completed.

The four locations in Chesapeake were as shown in Figure 4, a site in the Little Creek Harbor (LC), a site near the south Bay Bridge Tunnel (BT), a site near Thimble Shoal Channel (TS), and a site in the Middle Ground (MG) area.

A calibration experiment was conducted at the Dodge Island ship base in which echoes were recorded from the sea-surface using exactly the same equipment as used in the Chesapeake. Gravity and box cores were also taken along with echoes from the bottom at Dodge Island to give another bottom type. This data has also been analyzed.

Figure 5 shows the electronic equipment used to record bottom echo signals. A Datasonics DFT-210 was used to energize the transducers and then receive the echoes. A switching arrangement was used to select from two of 9

Figure 4. Map of the field experiment area.

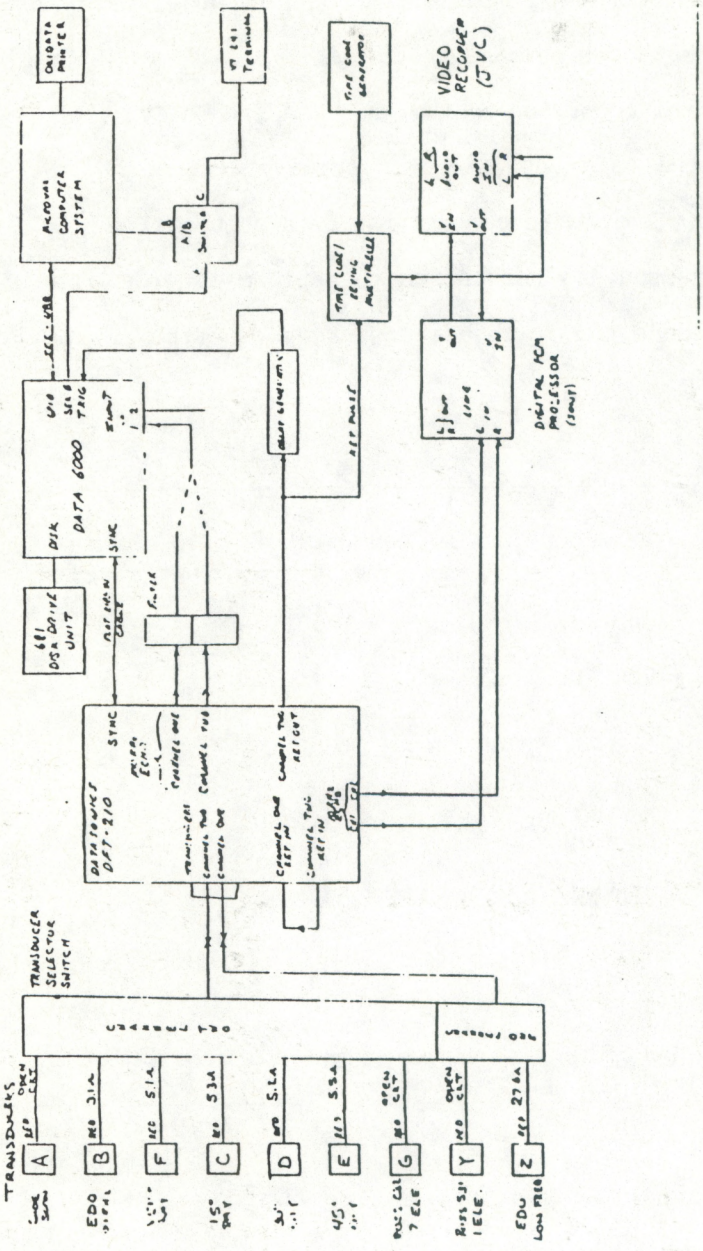

Figure 5. Diagram of data acquisition system used in field experiment.

transducers. An Analogics Data 6000 was used as a high speed analog to digital front end for a MicroVax computer system which recorded the digitized data on its internal hard disk. After data was recorded from a site it was dumped onto floppy disks for permanent storage.

A Sony PCM digital recording system was used with a JVC video recorder to provide back-up to the Data 6000/Microvax primary recorder. Switching and timing elements were provided to control the data acquisition.

The array of transducers was chosen to explore as wide a combination of frequencies, beam widths and incidence angles as practical. The transducers were as follows:

Letter in Diagram	Frequency	Beam Width	Angle
A	380 kHz	≈ 1x50°	0°
B	200 kHz	10°	0°
F	200 kHz	3°	0°
C	200 kHz	3°	15°
D	200 kHz	3°	30°
E	200 kHz	3°	45°
G	60-120 kHz	≈ 10°	0°
Y	60-120 kHz	≈ 25°	0° failed
Z	10-50 kHz	≈ 20°	0°

The QAD MicroVAX has been used to develop signal detection and averaging algorithms in preparation for comparing the experimental results to the model output. A Hilbert transform technique has been found useful for demodulating the signal. In this technique, the analytic signal is formed by taking the

existing signal as the real part, and by using the Hilbert transform of the signal as the imaginary part. The amplitude of this analytic signal is then the detected waveform. This technique is much better than the simple square and average used in the field to obtain a quick look at the data. At Dodge Island, the square and average showed the primary frequency waveform at the lower frequencies such as 10 kHz because the situation was so stationary. The Hilbert transform detector "interpolates" across the primary waveform producing a smooth envelope.

The major problem in analyzing the echo waveforms recorded in the field was to remove ship motion. Unfortunately, this is somewhat of a "cart and horse" problem. To remove ship motion, the variable part of the delay between the transmitted pulse and the start of the echo must somehow be extracted from the signal and removed. This is, of course, just the problem that this study is supposed to help solve. If we can remove ship motion with a simple operation on the echo, then the bottom depth can be determined by the same operation.

A technique has been found, however, that seems to effectively remove the variable part of the bottom echo delay. If the instantaneous acoustic intensity (normalized voltage squared) of the jth echo is written as $I_j(t+t_{jd})$, where the time delay t_{jd} varies from echo to echo and is due to ship motion, then t_{jd} is effectively removed by aligning the individual echoes so that the running integral of intensity of each echo crosses a threshold at a fixed time. This threshold is different for each pulse and is set to 1% of the integrated intensity (energy) in the pulse. That is, for each pulse t_{jd} is estimated as that value for which

$$\int_0^{t_{jd}} I_j(t)dt = .01 \int_0^{\infty} I_j(t)dt. \qquad (2)$$

To determine the actual surface profile of the bottom for input to the model calculations, a unique high-resolution bottom profiler was developed. This profiler is described in more detail elsewhere (Dammann, 1987, in preparation), but it consisted essentially of a self-propelled trolley carrying a precision echo-sounder down a 10 meter rigid track.

The trolley unit contained a stepping motor that was controlled from the surface so that its rotation could be precisely controlled. The motor was geared to a pulley sprocket which engaged a roller-chain that stretched the length of the track. By controlling the motor, the trolley position was very precisely known.

Attached to the trolley was a 3 MHz acoustic transceiver that functioned as a precision echo-sounder with a resolution of less than a centimeter. Because of the high-frequency and narrow beam of the unit, the problems associated with regular echo-sounders were avoided.

Figure 7 shows output from this precision profiler unit. Plotted is bottom depth as a function of horizontal position. Note the fine detail visible in the plot.

To provide information about the sediment at each site, bottom samples were taken, and analyzed in the laboratory. Depending on the nature of the bottom, a grab sample, box core or piston core was used. The samples were analyzed for grain size, porosity and mineral type. A copy of the geological analysis performed by the Ocean Chemistry Division of AOML is included as an appendix.

The five sites contained substantially different sediments so that the goal of sampling a wide variety of bottom types was reached. As might be expected, the Little Creek Harbor site was almost a pure mud with only a slight admixture of sand. The Bay Bridge sight was a firm sandy material, whereas the Thimble Shoal Channel site was coarse sand, almost gravel. The

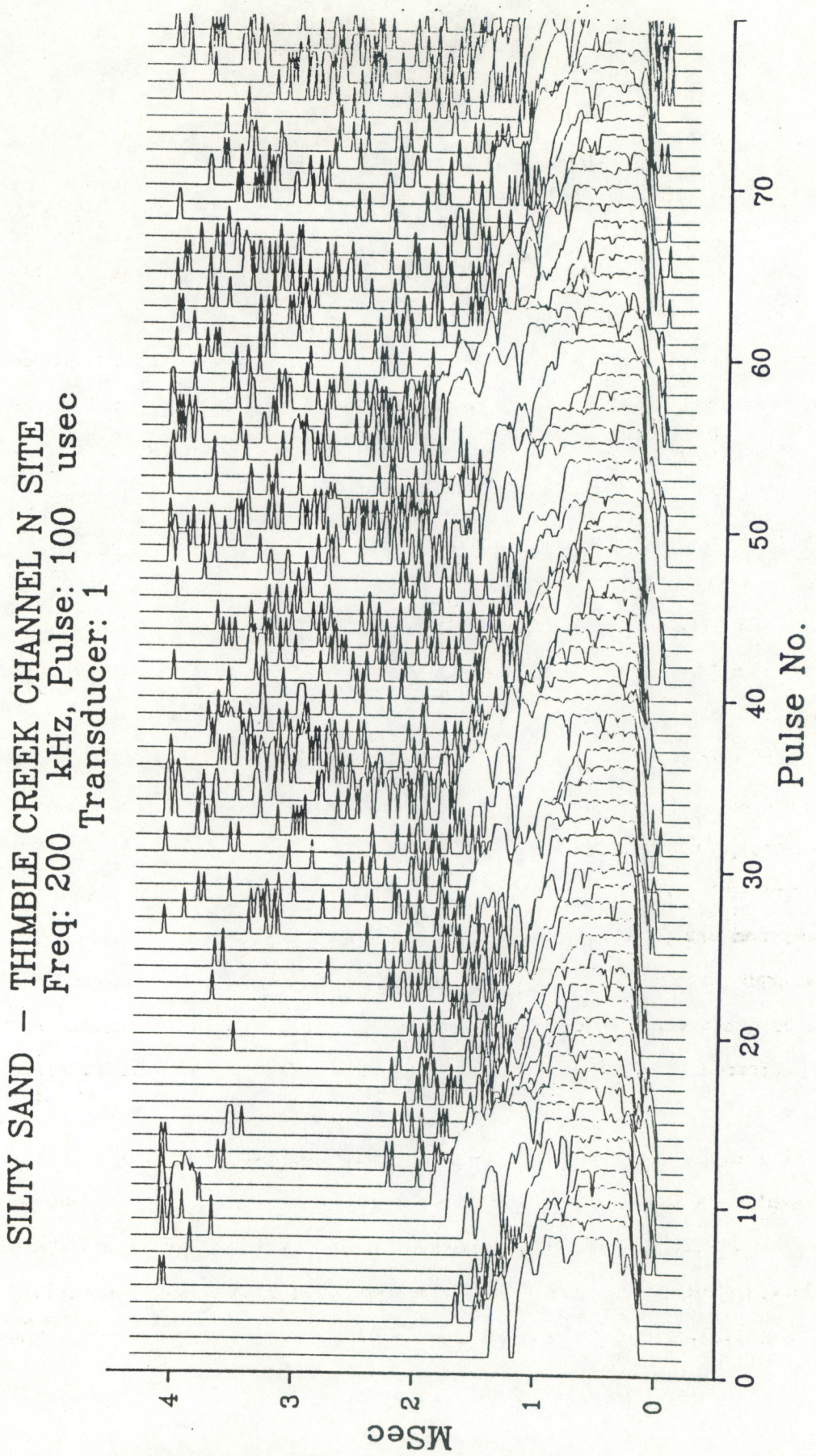

Figure 6. Waterfall plot showing unprocessed echo waveforms from field experiment.

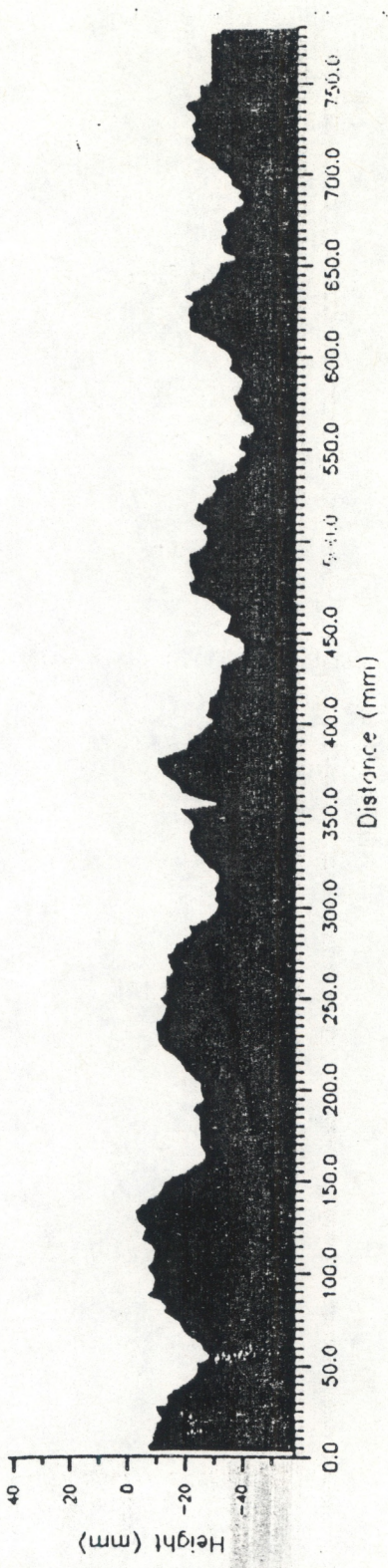

Figure 7. Typical trace of height versus distance taken by precision bottom profiler.

Middle Ground site was a mixture of silt and sand, as was the Dodge Island site.

The result of processing a set of echo waveforms is seen in Figure 8. This averaged echo waveform is from the Thimble Channel site data set. Waveforms for six distinct frequencies are shown in the figure. There is a systematic variation of overall shape with frequency somewhat in accord with the predictions of the model.

Figure 9 shows the model waveforms predicted on the basis of the observed sediment characteristics and surface profile at the Bay Bridge site. While there is an overall match to the pattern of change in waveform with frequency, the predicted pulse width is much narrower. These observed waveforms are much broader than the predictions, and contrary to the prediction, are broader at the lower frequencies than at the higher. There is also a suggestion of some periodicity in the way the waveforms decay. The 60 kHz and 120 kHz waveform in particular seem to show some ringing at times beyond 1 msec.

In order to explain this disagreement, an attempt was first made to refine the theory upon which equation (2) is based.

NEW THEORY

The derivation of the theoretical model was looked at in greater detail in order to identify terms that might have been neglected which can explain this oscillatory behavior.

The derivation of the model begins with the parabolic (or small angle) approximation to the exact acoustic Helmholtz equation. The parabolic approximation is well established in the underwater acoustic literature and is not the source of difficulty. Within this approximation the acoustic pressure, p, received at the transducer is given by

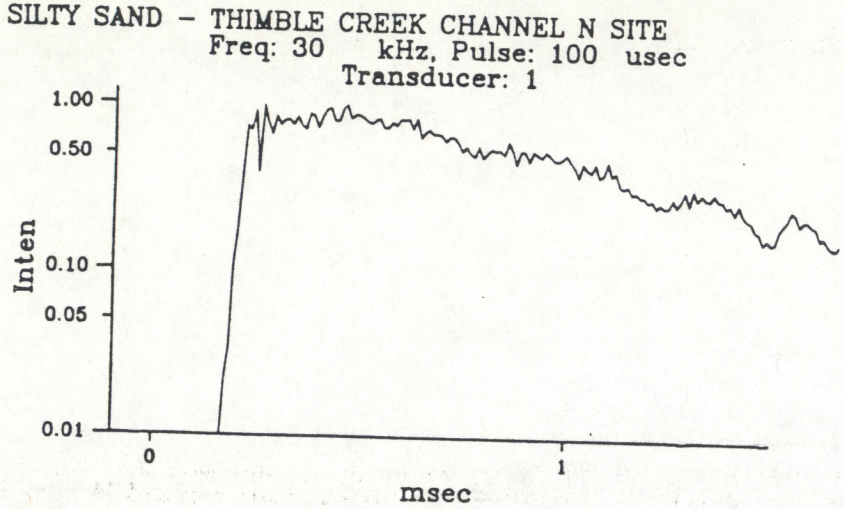

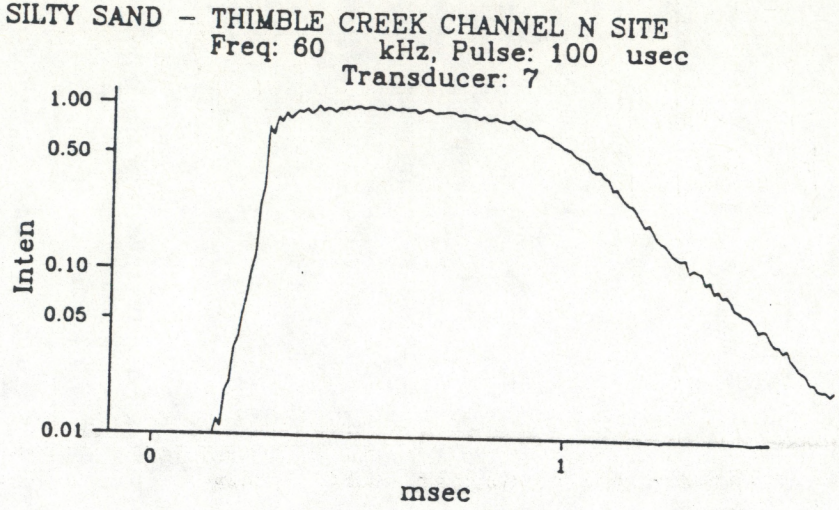

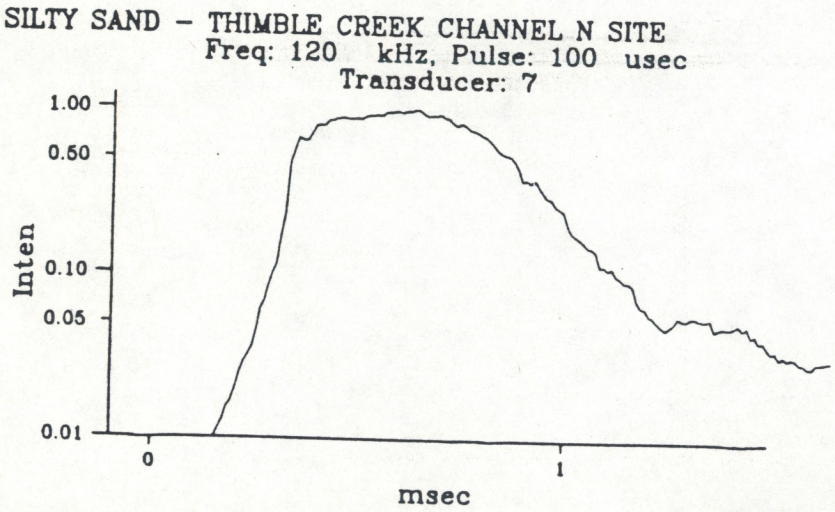

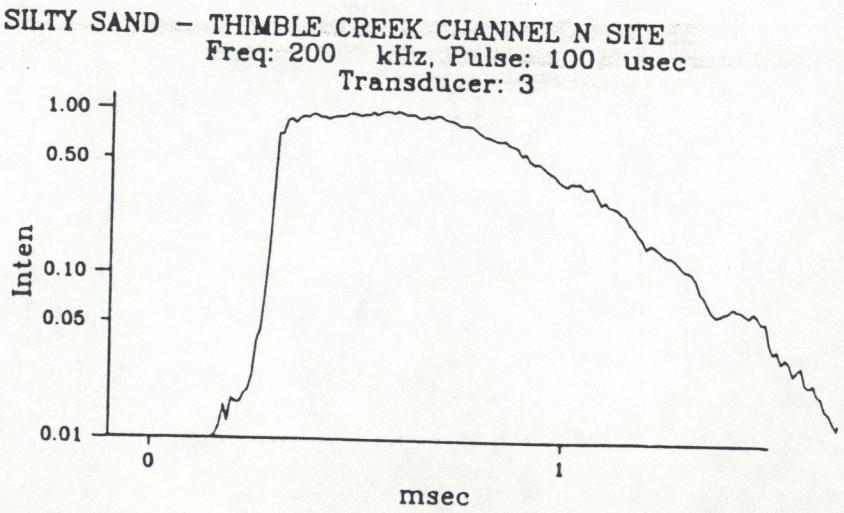

Figure 8. Sample waveforms observed from Thimble Channel site.

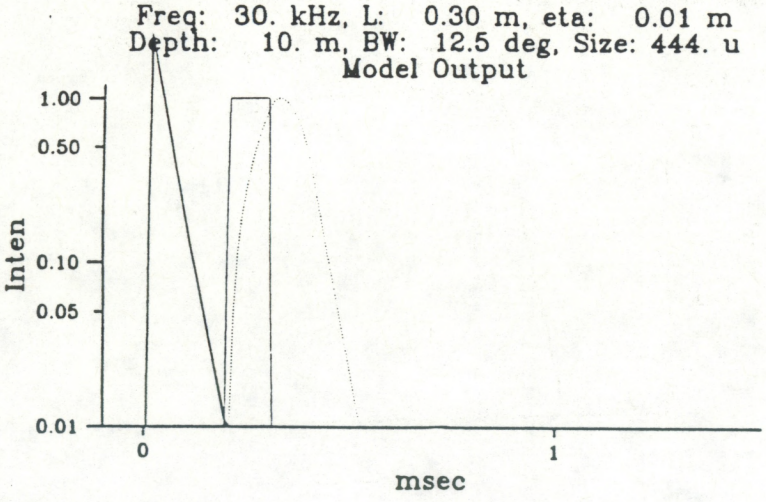

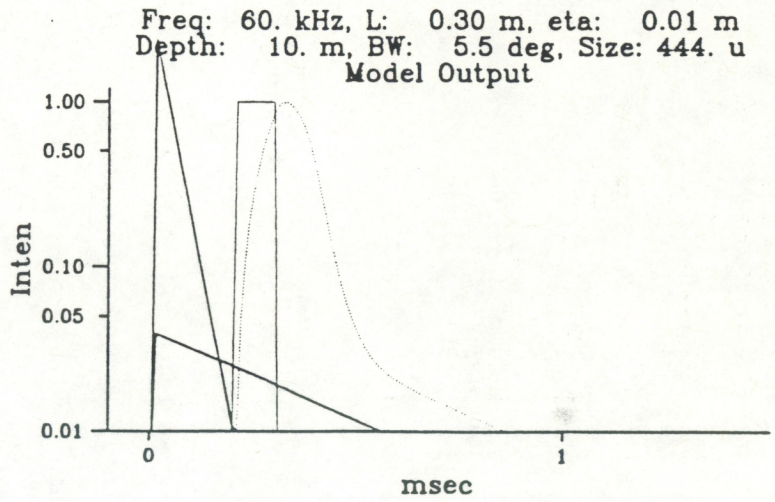

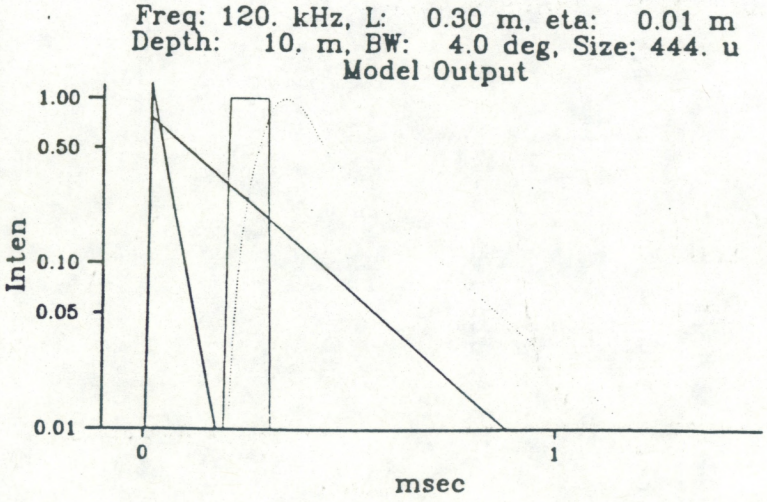

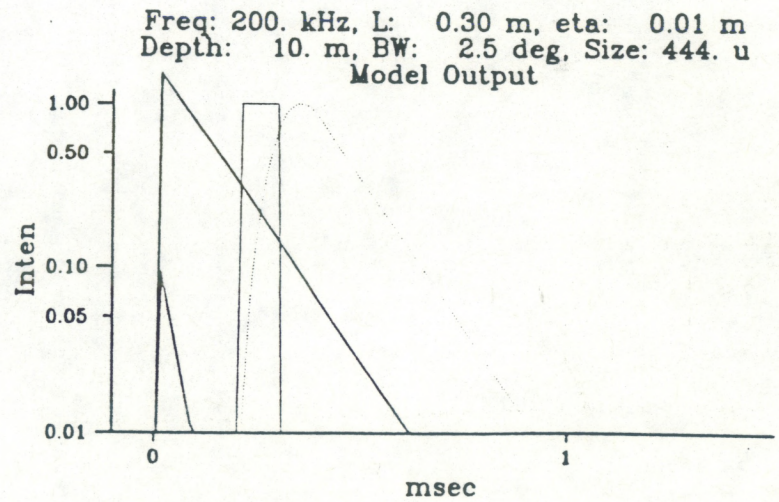

Figure 9. Model predictions for the Thimble Channel site.

$$p(z) = \int_{-\infty}^{\infty} g(x,z)\ \exp[2ikh(x)]dx. \qquad (3)$$

Where h(x) is the bottom height, $k=2\pi/\lambda$ is the acoustic wavenumber, and

$$g(x,z) = (2\pi iz)^{-1/2}\ \exp[ikx^2/(2z)], \qquad (4)$$

is the Green's function that describes acoustic propagation from depth z, horizontal position x to the transducer.

The depth h(x) is, of course, an unknown function. To produce a tractable expression the depth is considered to be a random function that can be averaged over a suitable ensemble of cases. In the case of the echo sounding study, this ensemble is, of course, the set of individual pings. Ship motion in between pings produces a different configuration of bottom and transducer for each ping so that the function h(x) is essentially different for each ping. As noted earlier, for the Dodge Island calibration experiment, the geometry was fixed so that there was very little ensemble averaging effect when the echo was from the bottom. When the echo was from the surface, however, surface wave activity provided a convenient ensemble.

The appropriate average to calculate is the ensemble average intensity

$$\langle I(z)\rangle = \rho c\langle p(z)p^*(z)\rangle, \qquad (5)$$

where the angular brackets <..> denote averaging the bracketed quantity over the statistical ensemble, and the conceptually complex pressure p is multiplied by its conjugate to form the intensity.

Putting (3) and (4) into (5) gives the intensity as a double integral

$$\langle I(z)\rangle = K \int\int_{-\infty}^{\infty} dx_1 dx_2 \, \langle \exp\{ik[2h(x_1)-2h(x_2)+(x_1^2- x_2^2)/2z]\}\rangle. \qquad (6)$$

A formula for the expected value of the exponential of an imaginary Gaussian random variable can be used to pass the average inside the exponential, giving:

$$\langle I(z)\rangle = K \int\int_{-\infty}^{\infty} dx_1 dx_2 \, \exp\{-2k^2\langle[h(x_1)-h(x_2)]^2\rangle + ik(x_1^2- x_2^2)/2z]\}. \qquad (7)$$

Making the further change of variable

$$s = (x_1 + x_2)/2, \; t = x_1 - x_2, \qquad (8)$$

simplifies this to

$$\langle I(z)\rangle = K \int\int_{-\infty}^{\infty} ds \, dt \, \exp\{-2k^2 C(t)\} \exp\{ikst/2\}, \qquad (9)$$

where $C(t) = \langle[h(0)-h(t)]^2\rangle$ is the structure function of the bottom variations. This structure function is closed related to the spatial correlation function; it is twice the variance times one minus the correlation function. Equation (8) can be simplified to recover the results of the original model by recognizing that the integral over s gives a delta function in t. That is, $\int ds \exp(ikst/z) = \delta(kt/z)$, so that

$$\langle I(z)\rangle = Kz/k \exp\{-2k^2 C(0)\}, \qquad (10)$$

since the delta function collapses the integral over t.

This result is the prediction for the coherent echo obtained in the original model. The assumptions in this model are that the indicident acoustic wave is essentially monochromatic. To obtain the pulse response, the single frequency, monochromatic response, must be integrated over the Fourier transform of the transmitted pulse.

The procedure is essentially the same as before, except that an additional integral over transmitted frequency must be included. This gives a four-fold integral for the expected intensity at time τ. Dropping the explicit z dependence gives,

$$\langle I(\tau)\rangle = K \int\int\int\int_{-\infty}^{\infty} dx_1 dx_2\, d\omega_1 d\omega_2 \exp\{i[\omega_1 h(x_1) - \omega_2 h(x_2)]/c$$

$$+ i[\omega_1 x_1^2 + 2 - \omega_2 x_2^2)]/2zc + i(\omega_1 - \omega_2)\tau\}. \qquad (11)$$

where the two angular frequency variables ω_1 and ω_2 have been introduced and the relation between wavenumber and frequency, $k = \omega/c$, has been used. Changing to sum and difference variables in time as was done previously for spatial variables before, $\eta = (\omega_1 + \omega_2)/2$ and $\zeta = \omega_1 + \omega_2$, gives

$$\langle I(\tau)\rangle = K \int\int\int\int_{-\infty}^{\infty} dx_1 dx_2\, d\eta d\zeta \exp\{i[(\eta+\zeta/2)h(x_1) - (\eta-\zeta/2)h(x_2)]/c$$

$$+ i[(\eta+\zeta/2)x_1^2 + 2 - (\eta-\zeta/2)x_2^2)]/2zc + i\zeta\tau\}. \qquad (12)$$

Collecting terms and dropping a term involving ζ times the mean depth since the mean depth is zero mean gives

$$\langle I(\tau)\rangle = K \int\int\int\int_{-\infty}^{\infty} dx_1 dx_2\, d\eta d\zeta \exp\{i\eta[h(x_1)-h(x_2)]/c$$

$$+ i\zeta[x_1^2 - x_2^2]/2zc + i\eta[x_1^2 - x_2^2]/2zc = i\zeta\tau\}. \qquad (13)$$

As before, this can be simplified since the integral over ζ introduces a δ-function with argument $\tau + [x_1^2 + x_2^2]/2zc$ which is therefore forced to zero. This term describes an "annulus" on the bottom whose radius is determined by the delay time within the pulse. The three remaining integrals then collapse to two: an integral over the frequency variable η and over the constrained sum of x_1^2 and x_2^2.

A reasonably tractable expression can be obtained by changing to polar coordinates $r = \sqrt{[x_1^2 + x_2^2]}$, and $\phi = \tan^{-1}(x_1^2/x_2^2)$. After taking the ensemble average, and introducing the structure function as before,

$$\langle I(\tau)\rangle = K\sqrt{4\tau zc} \int_{-\infty}^{\infty} d\eta \int_{-\pi}^{\pi} d\phi \exp\{-\eta[C(\sqrt{\tau}cz(\cos\phi - \sin\phi))]/2c^2$$

$$+ 2i\eta\, \tau z \cos 2\phi/2zc\}. \qquad (14)$$

No closed form solution is apparent for this double integral, but the second should give a δ-function type sieving of the integral over ϕ. The integral over η forces ϕ to have values of $\pi/2$ plus even multiples of π. The argument of C in the first term is thus either 0 or $\sqrt{2}$; recall that C is an even function so sign does not matter.

This gives the final approximation

$$\langle I(\tau)\rangle \simeq \exp\{-2^2\, C(2\sqrt{\tau zc})\}. \qquad (15)$$

where k is the wavenumber at the center of the narrow band of transmitted frequencies. In case the structure function C is quadratic, an assumption commonly made in scattering theory, this result coincides with the earlier theory. Equation (15) then reduces to a simple exponential decay with time delay τ.

Use of the structure functions shown in Figure 13 extracted from the track data only modify the form of the surface reverberation slightly, changing the decay curves in Figure 9 into damped decay curves without changing their width very much. As a result, this refinement to the theory is not sufficient to account for the observations, and a more fundamental change was needed.

A successful line of attack was found in a paper by Clay (1960). While Clay was concerned with fluctuations of echoes at grazing incidence, his ansatz proved useful. Clay considers the sea surface to be a collection of statistically independent patches that together contribute to the echo. This approach is supported by Figures 10 and 11 which plot width pulse versus frequency and transducer beam width.

Taking this approach, the total surface reverberation waveform, I_s', is

$$I_s'(t) = A(t) * I_s(t) , \tag{16}$$

where * denote convoltion, A(t) is the ensonified area at time t, and I_s is the exponentially decaying surface reverberation. The area A(t) is determined by the transducer beam patterns shown in Figure 12, but for short times it increases linearly with t, and then remains constant until the ensonfied annulus reaches the beam width.

Figure 14 shows the results of applying equation (16). The plotted quantities are the same as shown in Figure 4, with the addition of a dark

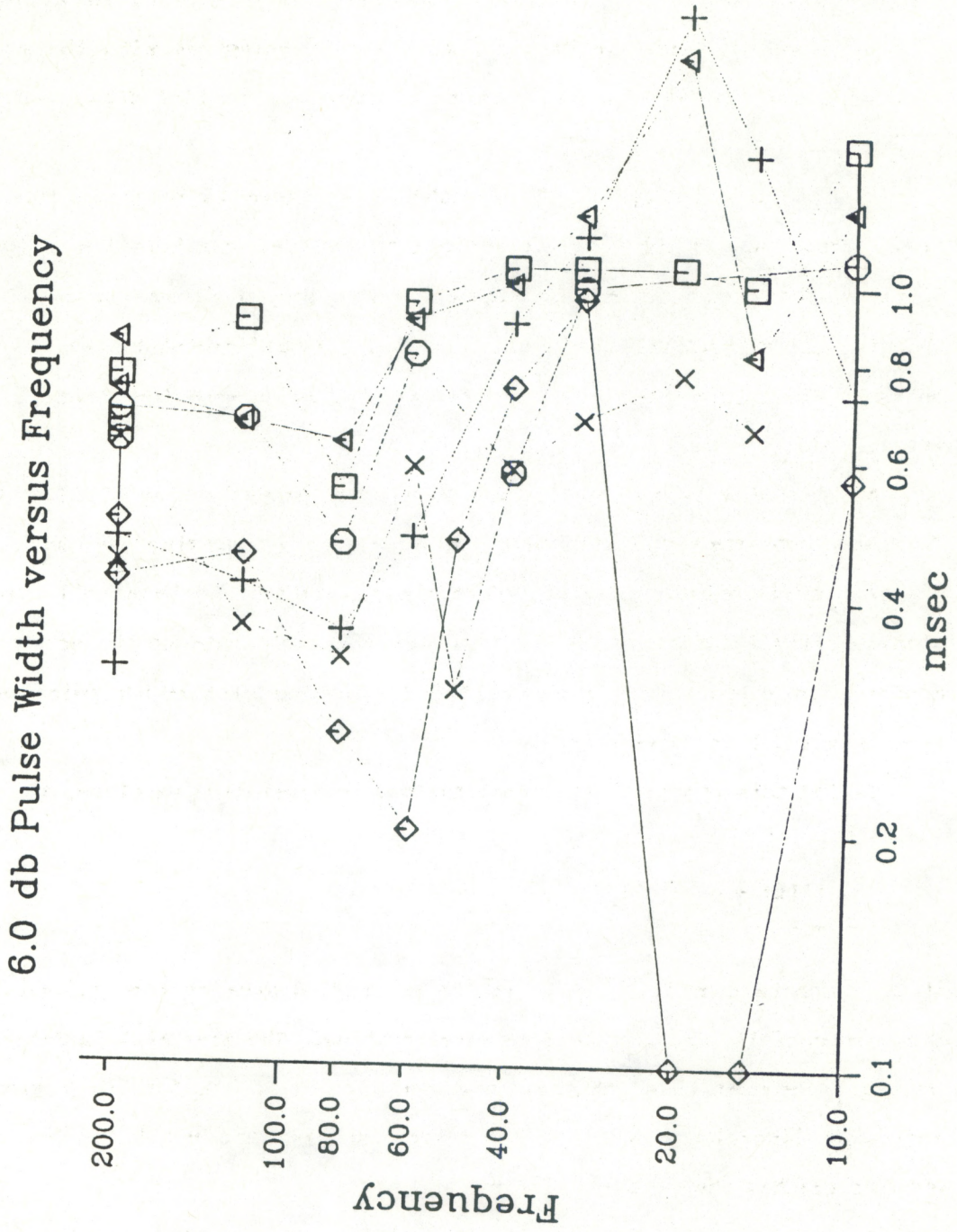

Figure 10. Observed pulse width versus frequency.

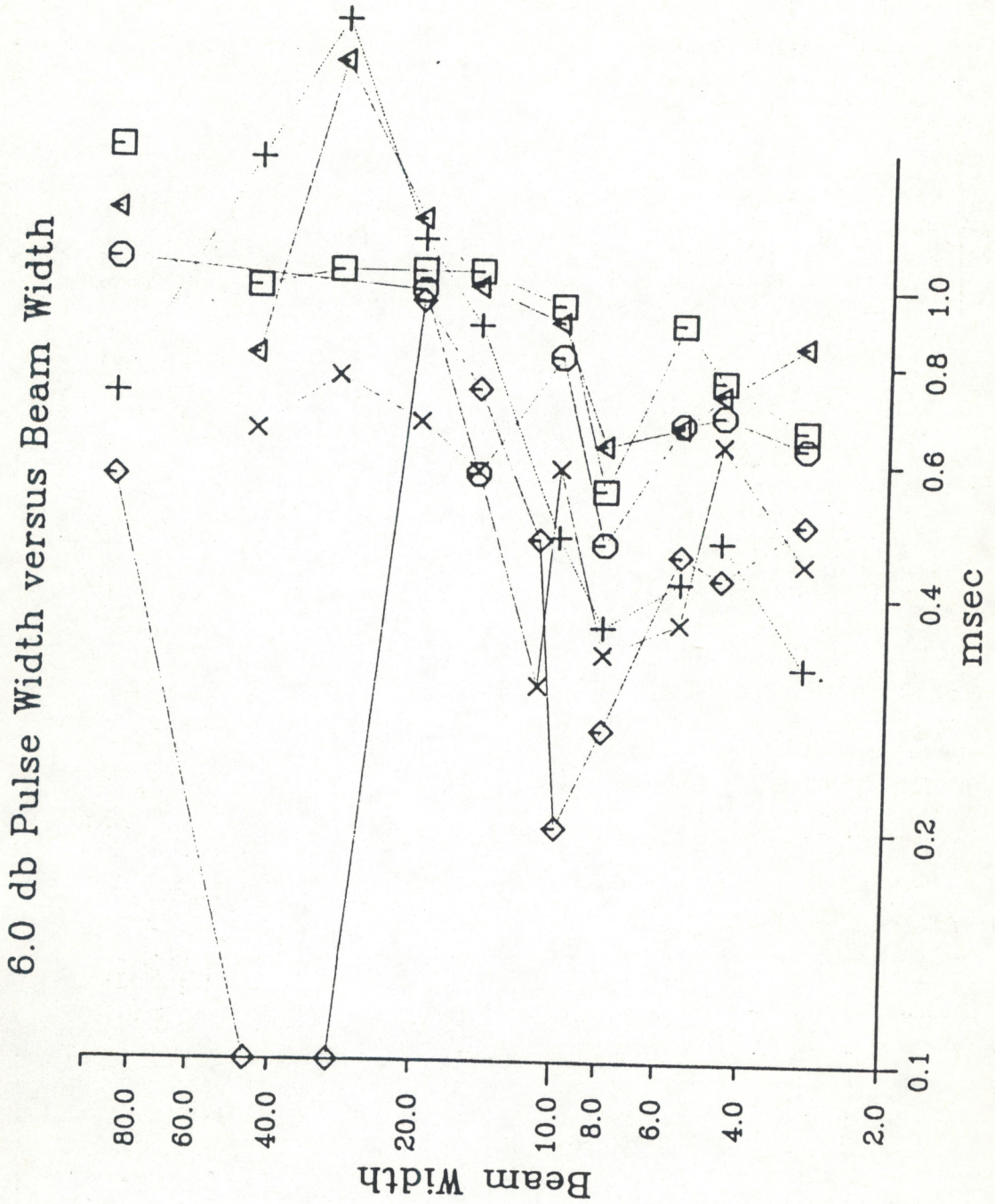

Figure 11. Observed pulse width versus transducer beam width.

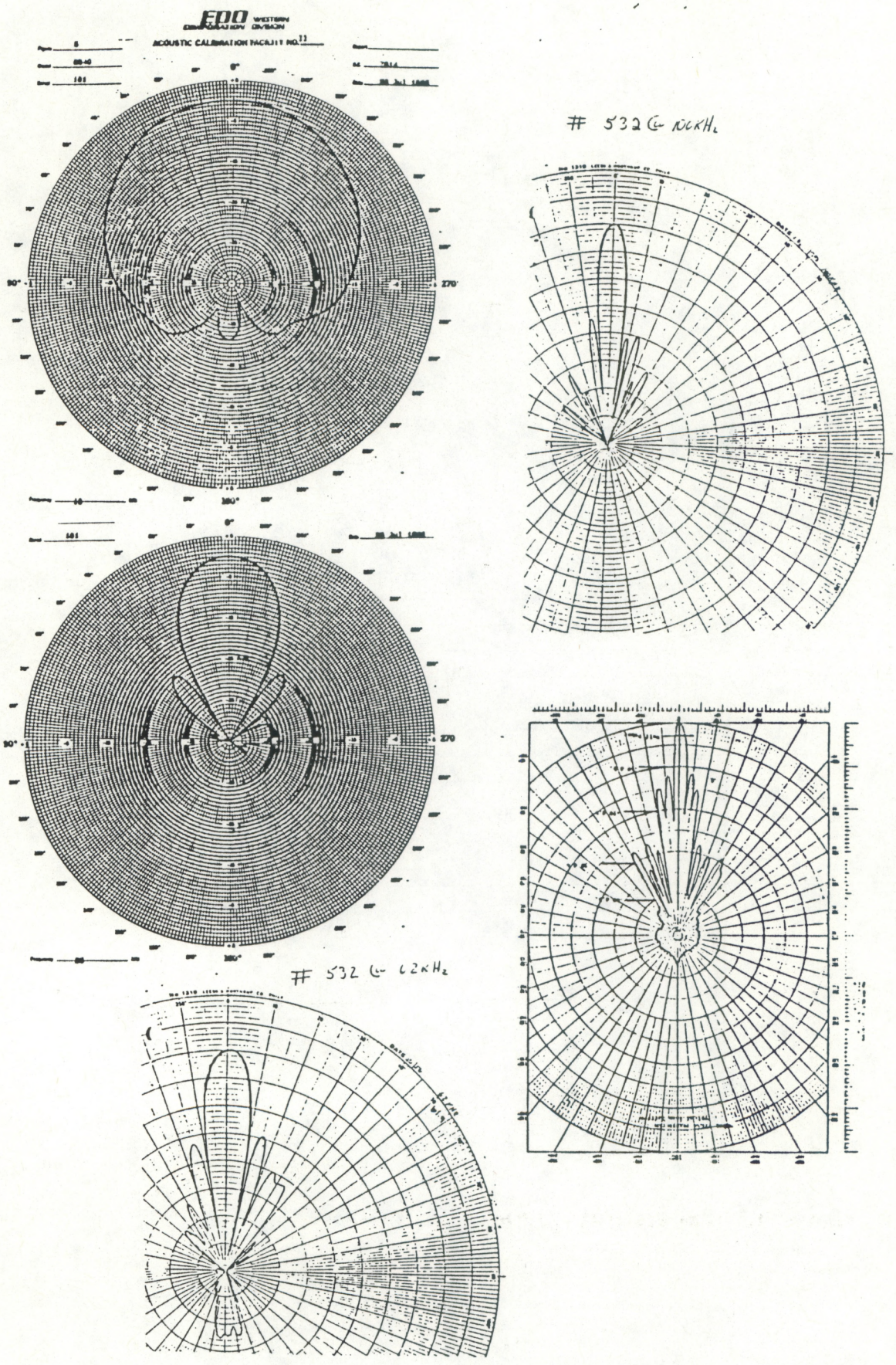

Figure 12. Transducer beam patterns.

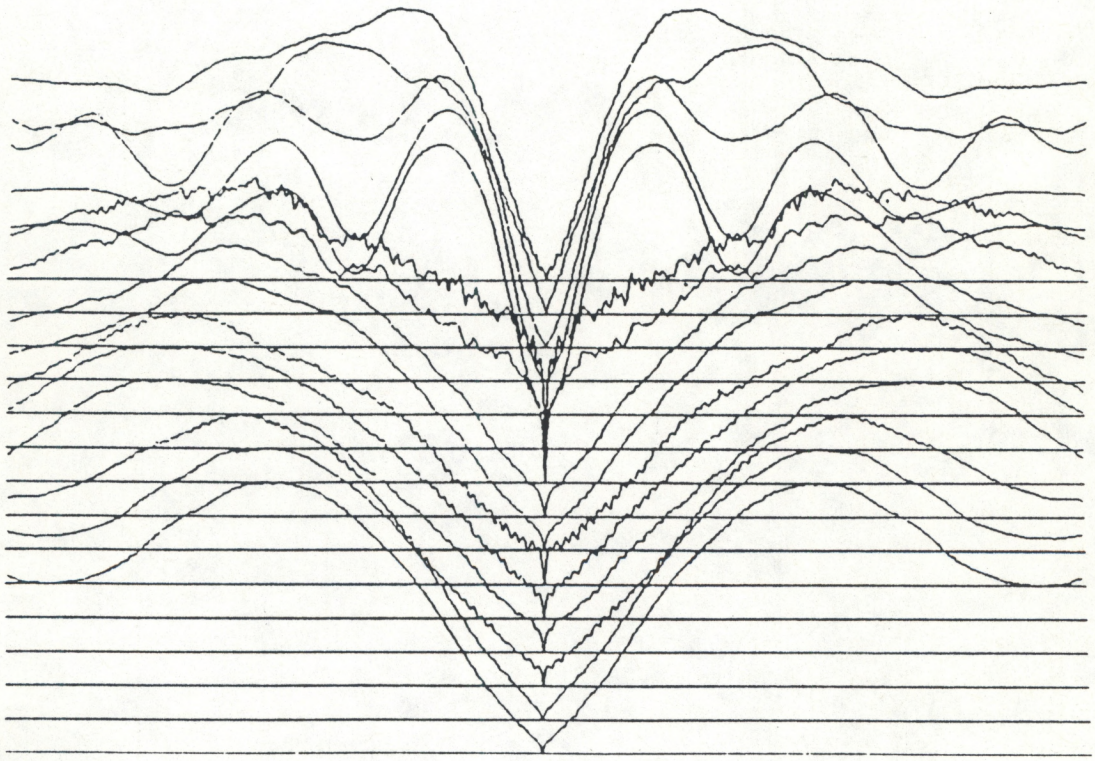

Figure 13. Spatial structure functions.

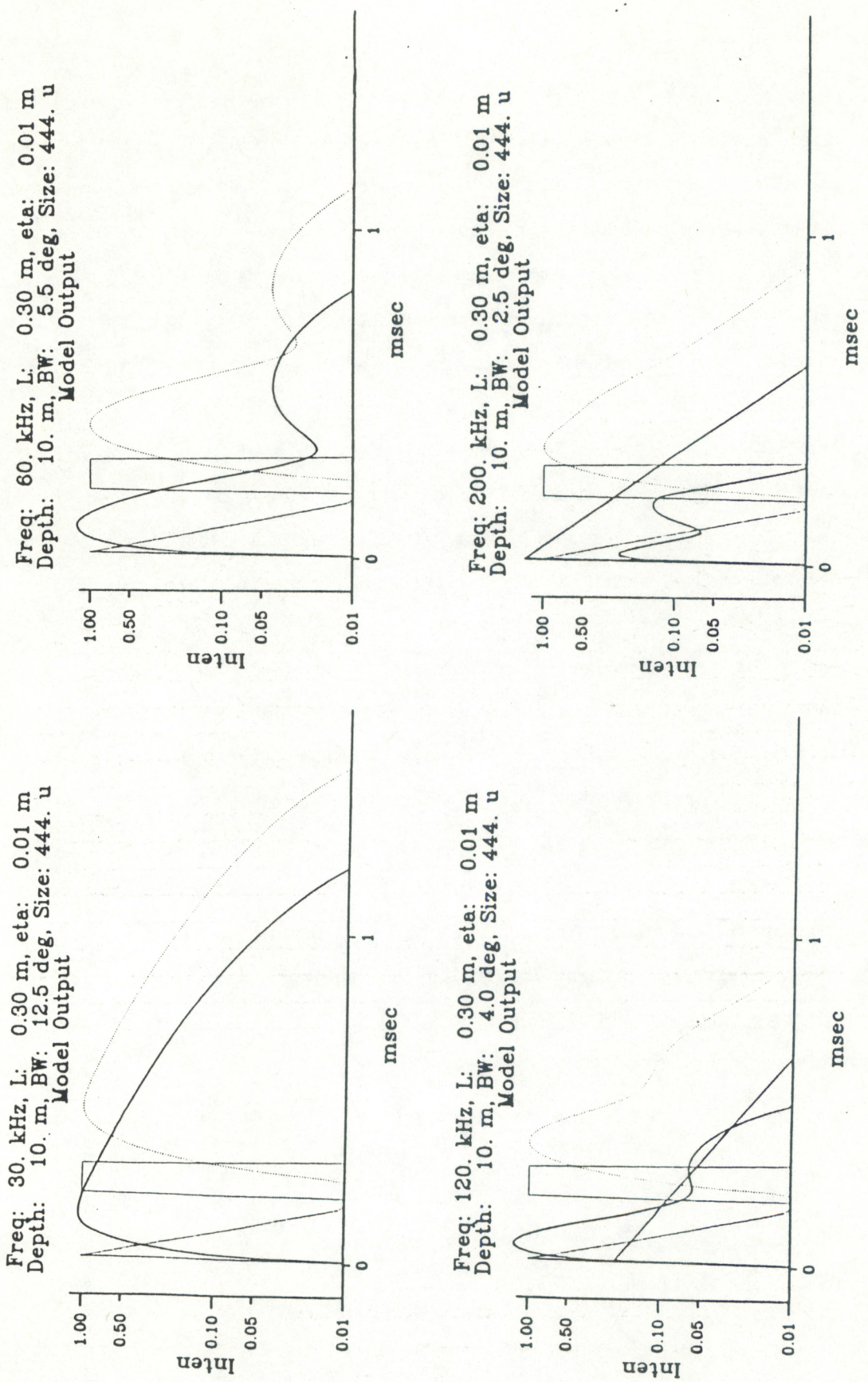

Figure 14. Modified model predictions for the Thimble Channel site.

curve starting at t = 0. This curve is I_s', the result of convolving the "far-field" reverberation function with the transducer beam pattern. The form of A(t) mirrors the beam pattern of the transducer. At 60 kHz in particular A(t) shows oscillatory behavior reflecting transducer sidelobes.

The agreement between predictions and observations is much better when I_s is used to model the surface reverberation. Physically A(t) should be normalized by the size of the statistically independent patches, but because absolute calibration for the transducers was unavailable, this refinement is unnecessary here. As an estimate for the size of the patches, the characteristic length L extracted from the profiles can be used. In Chesapeake Bay this length ranges from 30 cm to about 1 meter, so that many independent patches would be found within the ensonified area of a given pulse.

The model presented here is essentially a heuristic modification to an existing theory, and while it explains the observations much better than the unmodified theory, there is much room for refinement. In particular, the convolution performed in equation (3) tacitly assumes that the scattering from each independent patch of the bottom is independent of incident angle. While to first approximation this is true, more refined calculations and observations will need to take such effects into account.

Nevertheless, the present model fits the data well enough that it should serve the purpose for which it was originally developed: the testing and refinement of operational echo-sounders.

LITTLE CREEK DISCUSSION

As mentioned earlier, the bottom at the Little Creek site was a sandy silt; details can be found in the appendix. The grain size used for calculations of Rayleigh backscattering was 400 microns. Despite the presence

of a large amount of fine silt, the presence of fairly coarse material with a large acoustic cross section tilted the acoustically average grain size toward the larger sizes. The surface roughness estimated from the track data was 4 cm RMS roughness height, with a characteristic length of 1.1 meters.

The bottom is therefore fairly smooth, and one does not expect a great deal of volume scattering. This expectation is born out by the observations shown in Figure 15. The lower frequency pulses are broad as a result of the convolution of individual surface element scattering with the broad transducer beam pattern. Above 80 kHz, however, the pulses narrow down and are primarily a result of volume scattering effects. The model predictions are shown in Figure 16, and the agreement is fairly good.

Echoes from the off-vertical transducers are shown in Figure 17. Transducer 3 is vertical, transducer 4 at 15°, transducer 5 at 30°, and transducer 6 is at 45°. These waveforms would be encountered in a multiple beam system like SeaBeam. As the angle increases, the pulse broadens out and develops a tail. The first return in the off-vertical beams is due to sidelobes. This is most evident for transducer 6 where the sidelobe return precedes the main body of the pulse by over a millisecond.

The variance over the ensemble of pulses was calculated and is presented in Figures 18 and 19 as plots of standard deviation of the intensity divided by the intensity; the dotted curve reproduces the pulse amplitude. For a fully random signal composed of the sum of many randomly phased reflections from a variety of scatterers, this value should be near one. For a deterministic signal, an echo from a constant target, this value should be small and is determined by the signal to noise ratio of the data gathering system. When the pulse drops below a threshold, the standard deviation is suppressed; this accounts for the jagged appearance of grazing transducer 6.

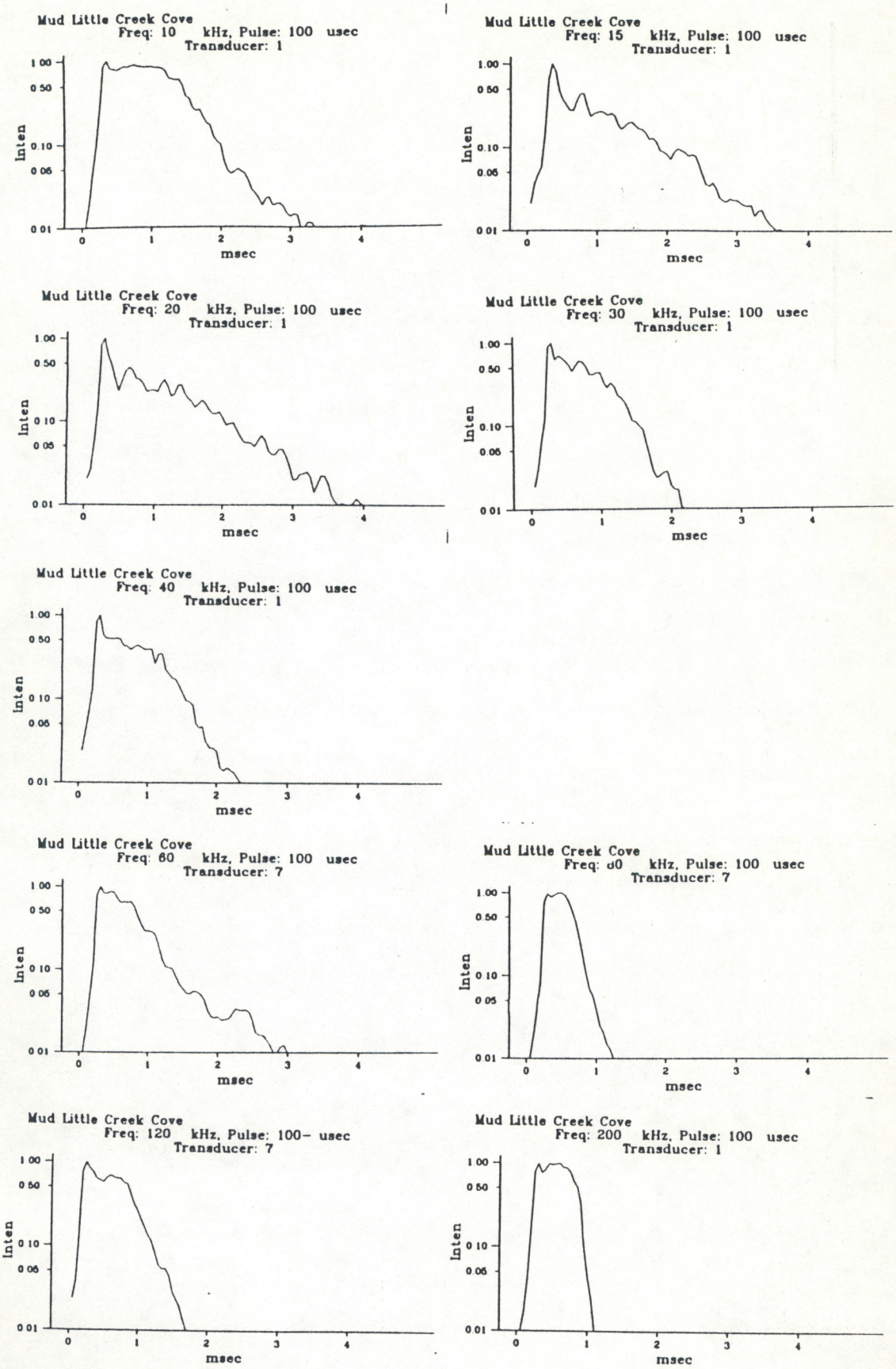

Figure 15. Observed echoes for the Little Creek site.

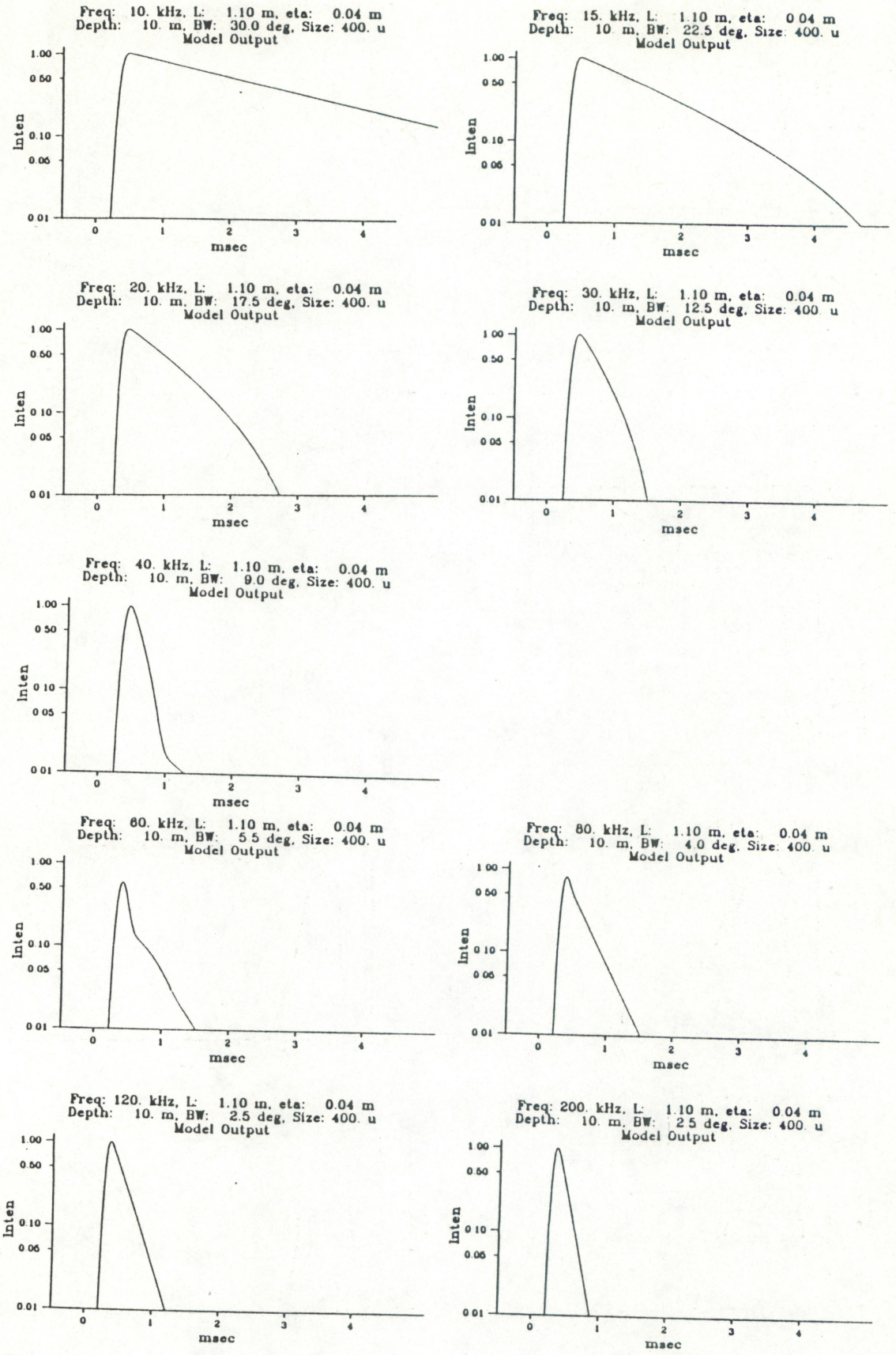

Figure 16. Model predictions for the Little Creek site.

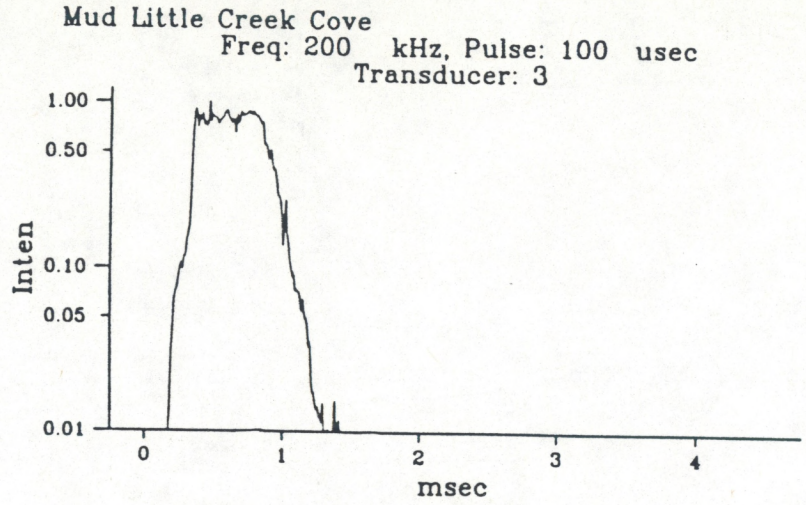

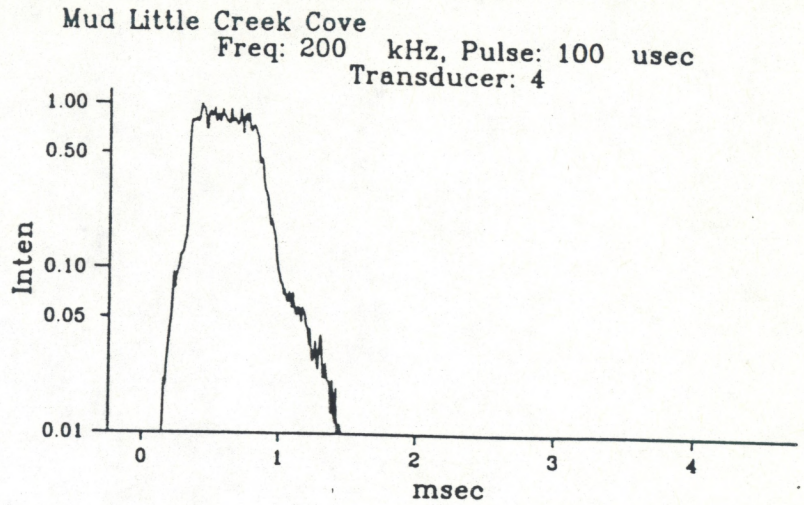

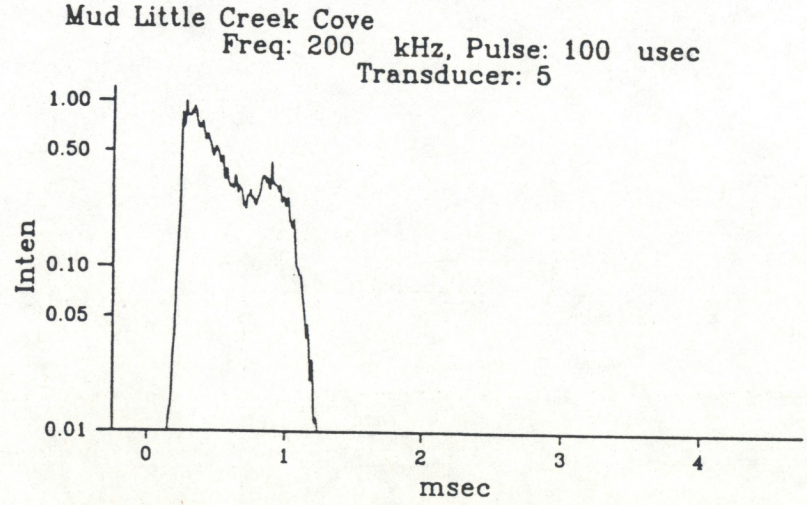

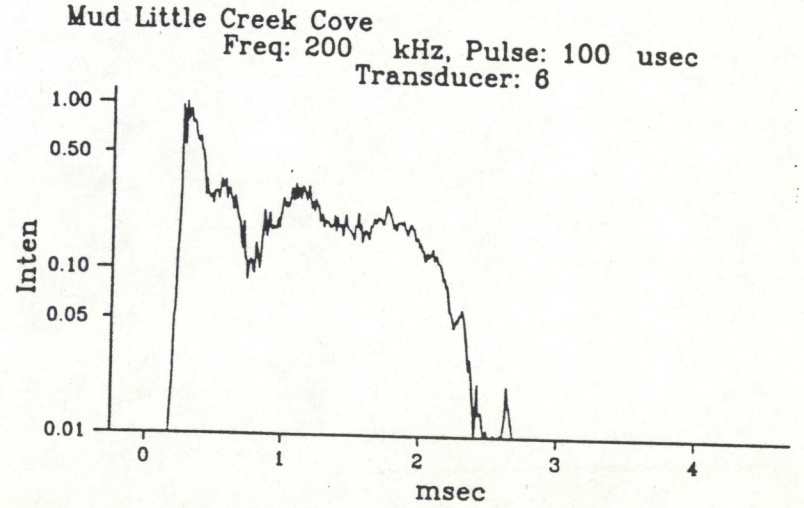

Figure 17. Observed grazing echoes for the Little Creek site.

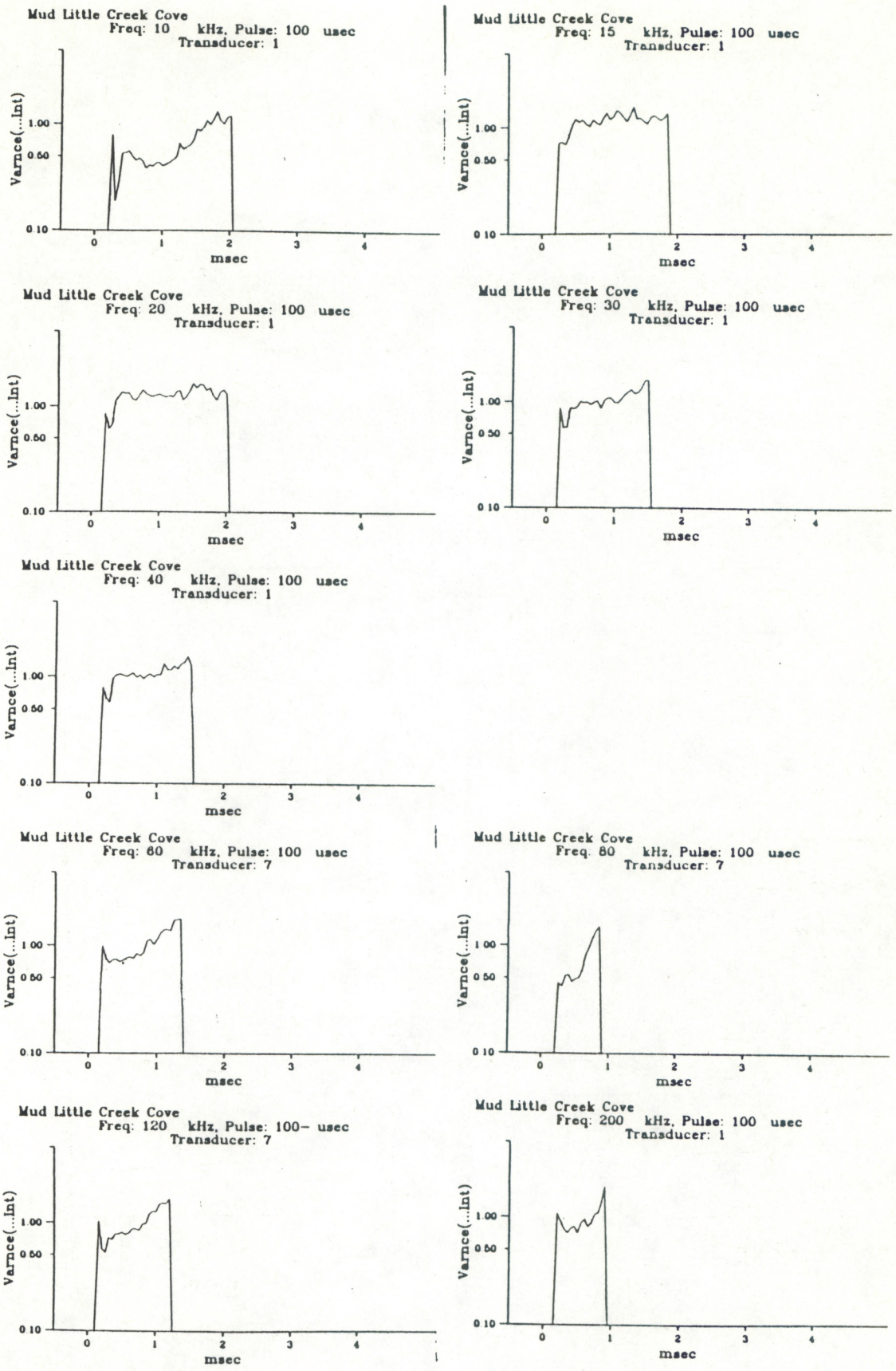

Figure 18. Echo variability for echoes from Little Creek.

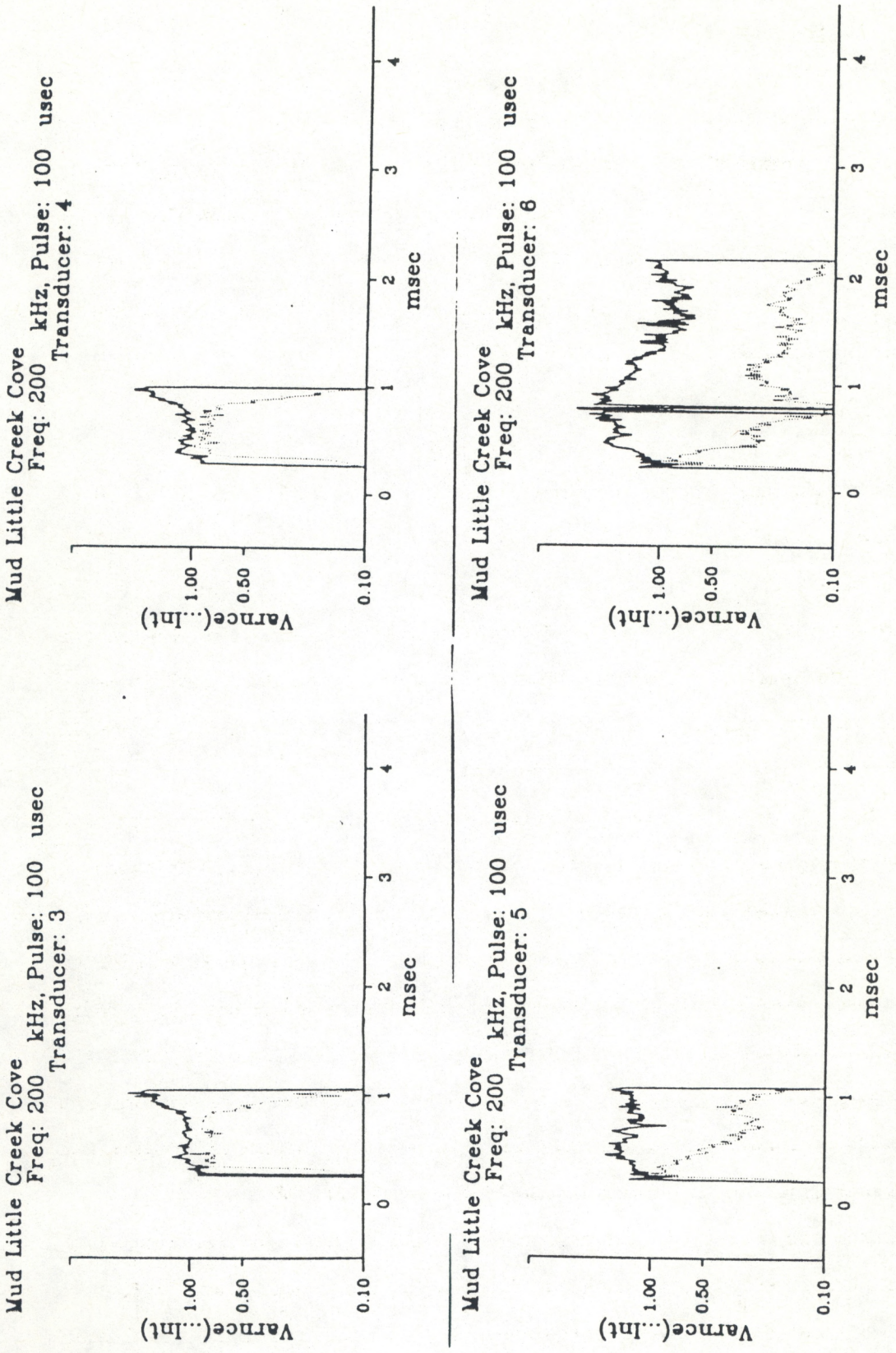

Figure 19. Echo variability for grazing echoes from Little Creek.

For the most part, the signals are fully random with the normalized standard deviation near unity. Only at the leading edge of the lower frequencies is the standard deviation low enough to suggest a constant target. This is to be expected since at lower frequencies the wavelength becomes larger than the roughness height. During the tails of pulses, the normalized standard deviation rises above one; this is probably due to the combination of signal variability and additive noise.

BAY BRIDGE DISCUSSION

The bottom at the Bay Bridge site was firmly packed sand; details can be found in the appendix. The grain size distribution was not widely disperse, so the diameter used for calculations of Rayleigh backscattering of 374 microns agrees fairly closely with the volume weighted mean grain size in the appendix. The surface roughness estimated from the track data was estimated to be 1.8 cm RMS roughness height, with a characteristic length of 0.22 meters.

This bottom is also fairly smooth, and but the sandy nature of the sediment should give significant volume scattering. The observations shown in Figure 20 agree with this picture. The lower frequency pulses are not as broad as a seen in Little Creek; because the individual surface element scatterers are smaller, the effect of the convolution with the beam pattern is different. As before, above 80 kHz the pulses become narrower, but are broader than before due to the lower absorption of the finer grained sand and are primarily a result of volume scattering effects. The model predictions are shown in Figure 21, and the agreement is again fairly good.

Data from the off-vertical transducers are shown in Figure 22. As before transducer 3 is vertical, transducer 4 at 15°, transducer 5 at 30°, and transducer 6 is at 45°. Again as the angle increases, the pulse broadens out

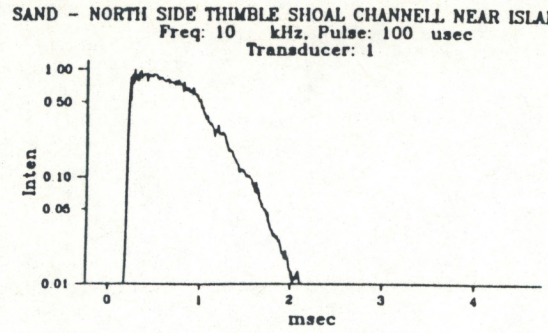

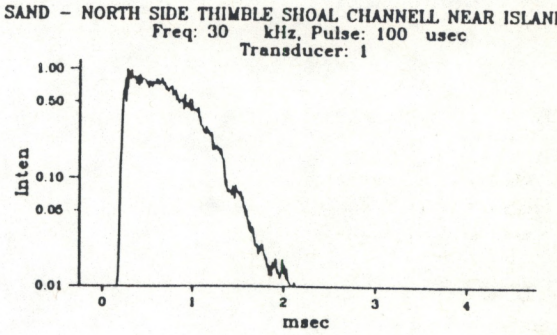

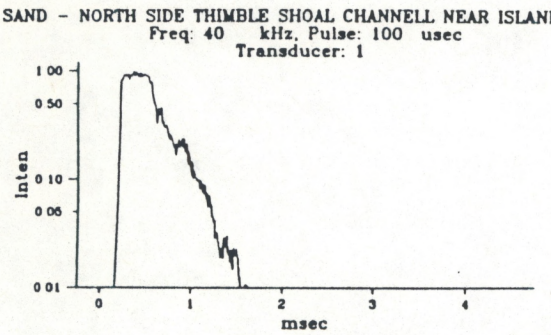

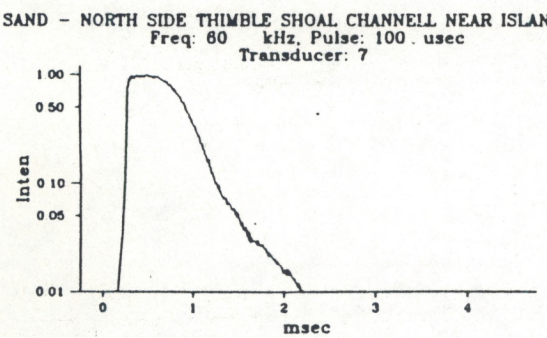

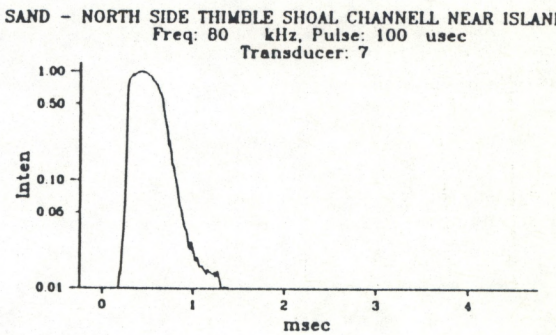

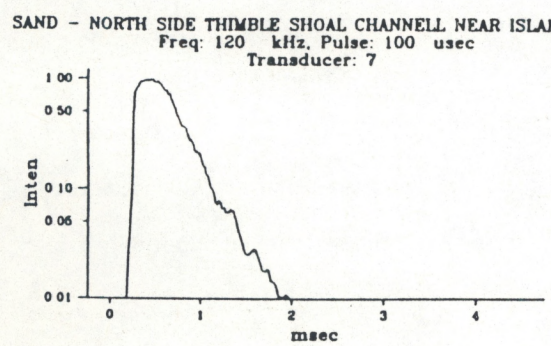

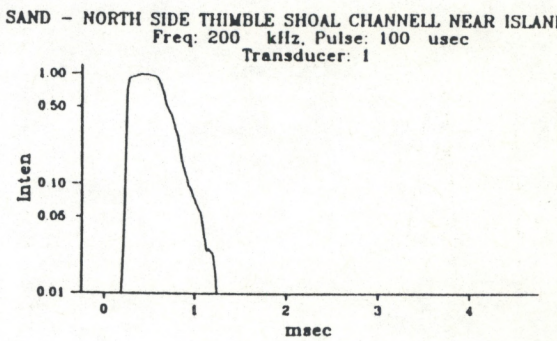

Figure 20. Observed echoes for the Bay Bridge site.

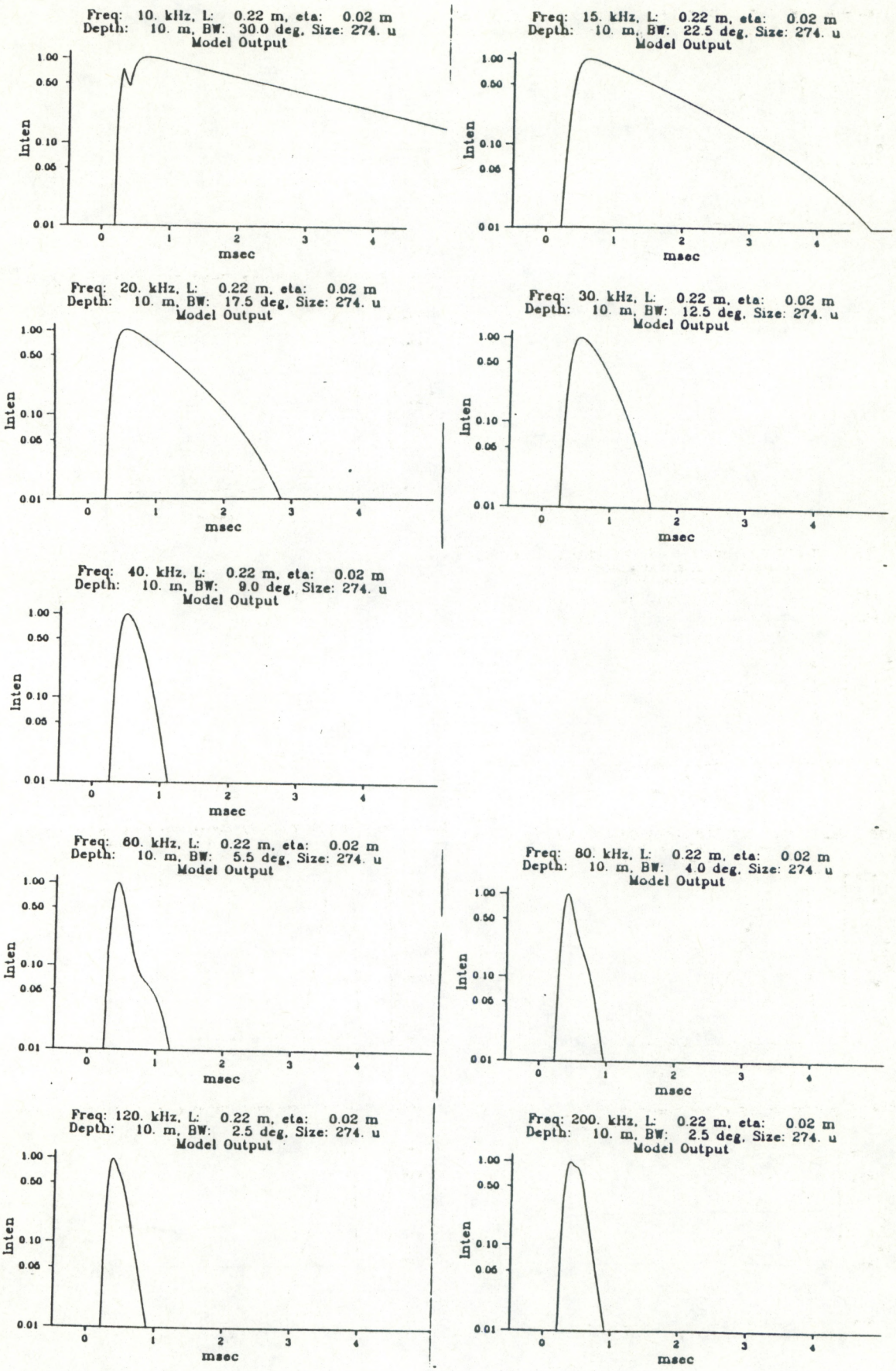

Figure 21. Model predictions for the Bay Bridge site.

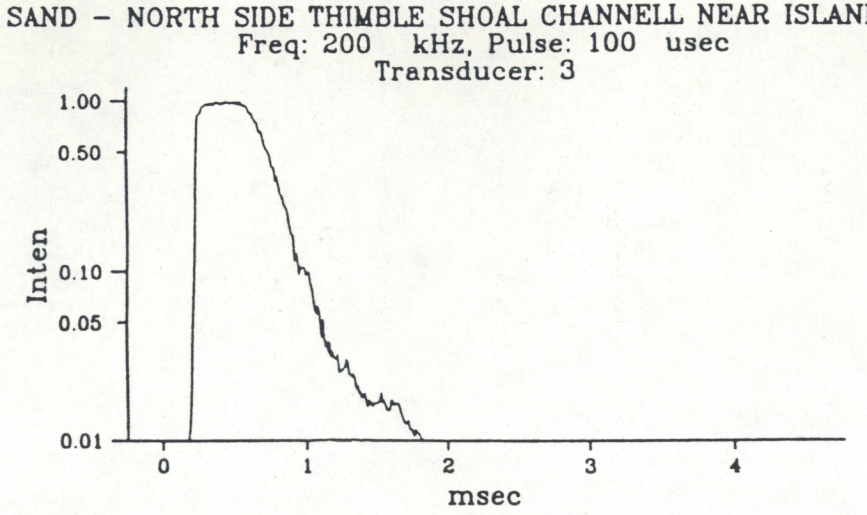

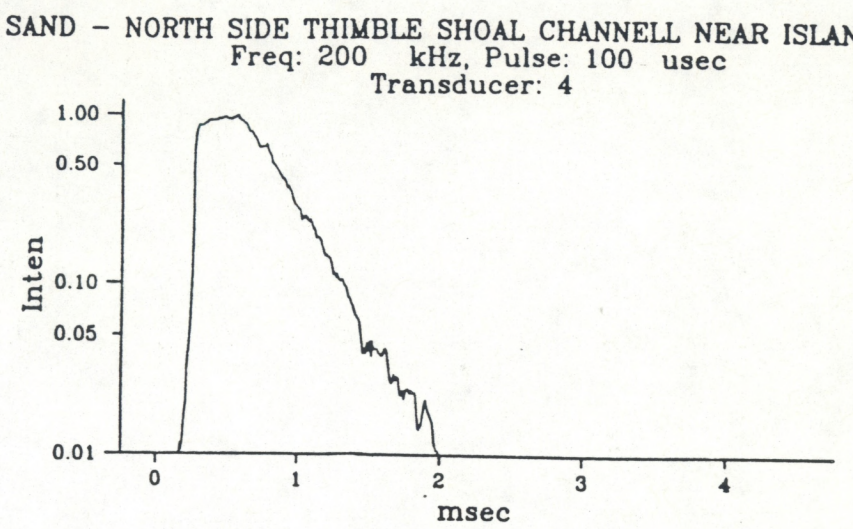

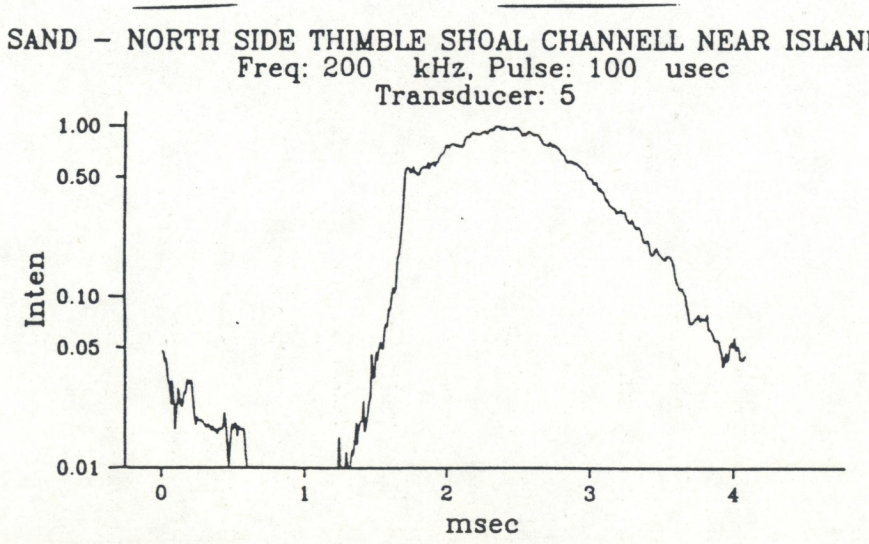

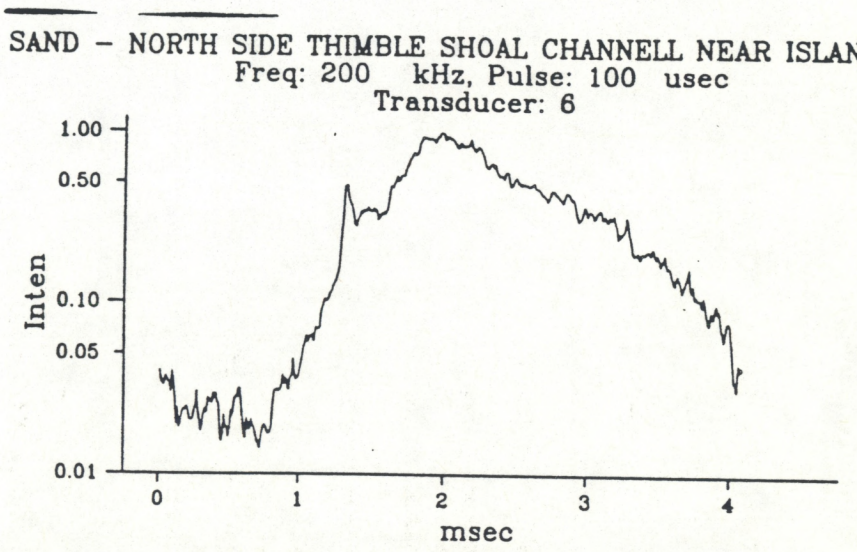

Figure 22. Observed grazing ehcoes for the Bay Bridge site.

and develops a tail. The first return in the off-vertical beams is due to sidelobes. This is most evident for transducer 6 where the sidelobe return precedes the main body of the pulse by over a millisecond. The sidelobe return is very sharp here due to the low roughness and small correlation length of the bottom.

The variance over the ensemble of pulses was calculated and is presented in Figures 23 and 24 as plots of standard deviation of the intensity divided by the intensity. As before, for the most part, the signals are fully random with the normalized standard deviation near unity. Only at the leading edge of the lower frequencies is the standard deviation low enough to suggest a constant target. This is to be expected since at lower frequencies the wavelength becomes larger than the roughness height. During the tails of pulses, the normalized standard deviation rises above one; this is probably due to the combination of signal variability and additive noise.

THIMBLE CHANNEL DISCUSSION

The bottom at the Thimble Channel site contained the coarsest sediment found during the experiment; the bottom consisted of coarse sand, almost a gravel. The grain size used for calculations of Rayleigh backscattering was 444 microns. The surface roughness estimated from the track data was estimated to be 3 cm RMS roughness height, with a characteristic length of .3 meters.

The bottom is smooth enough that one expects some coherent component to the echoes at lower frequencies. At the same time there should be a good deal of volume scattering even at lower frequencies because of the coarseness of the sediment. This expectation is born out by the observations shown in Figure 25. The lower frequency pulses are broad as a result of the combination of surface scattering with volume scattering. Above 80 kHz,

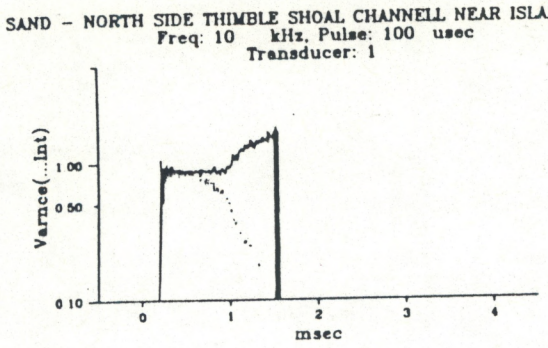

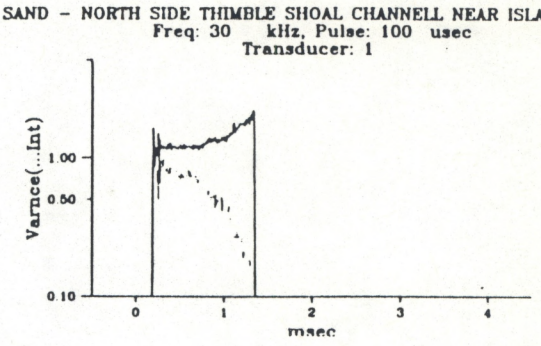

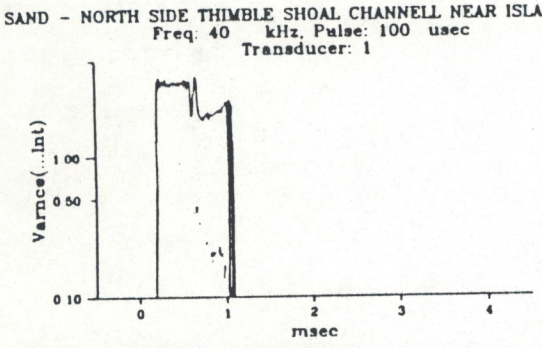

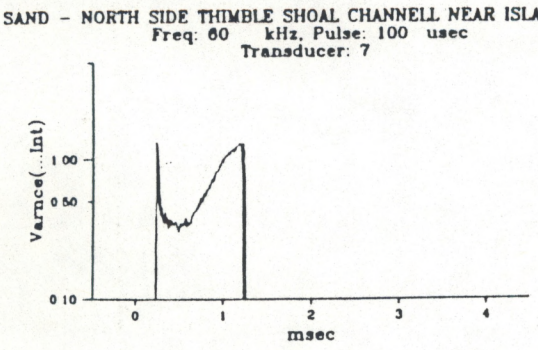

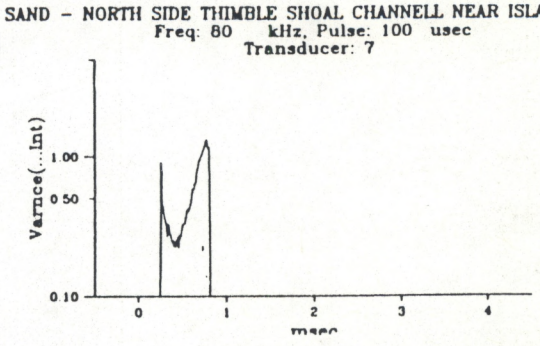

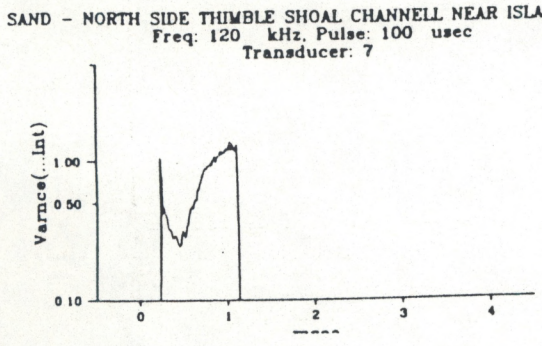

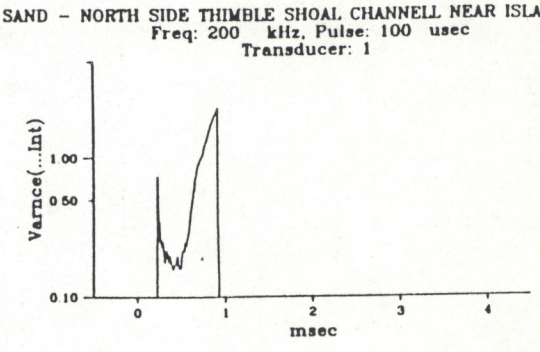

Figure 23. Echo variability for echoes from Bay Bridge.

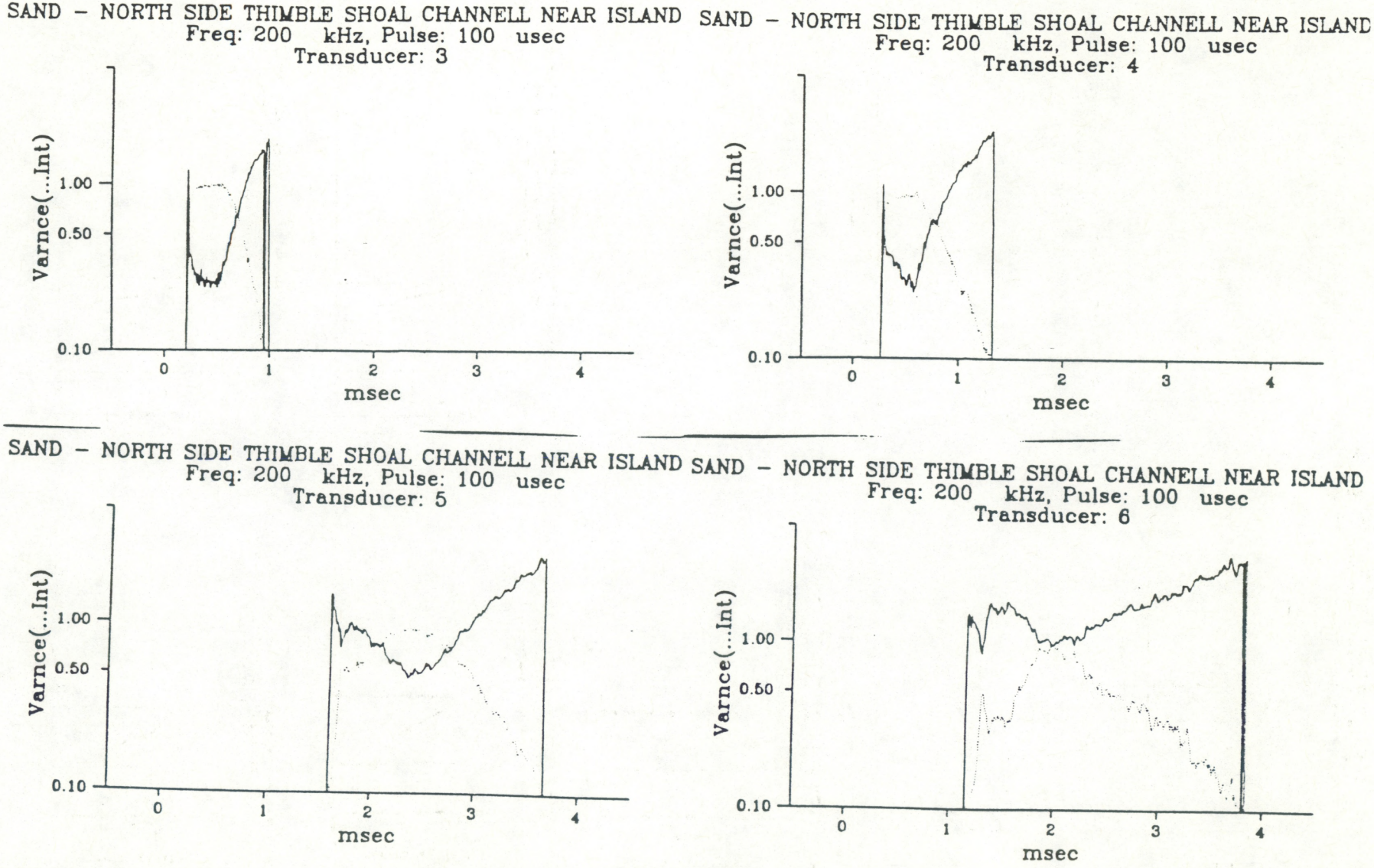

Figure 24. Echo variability for grazing echoes from Bay Bridge.

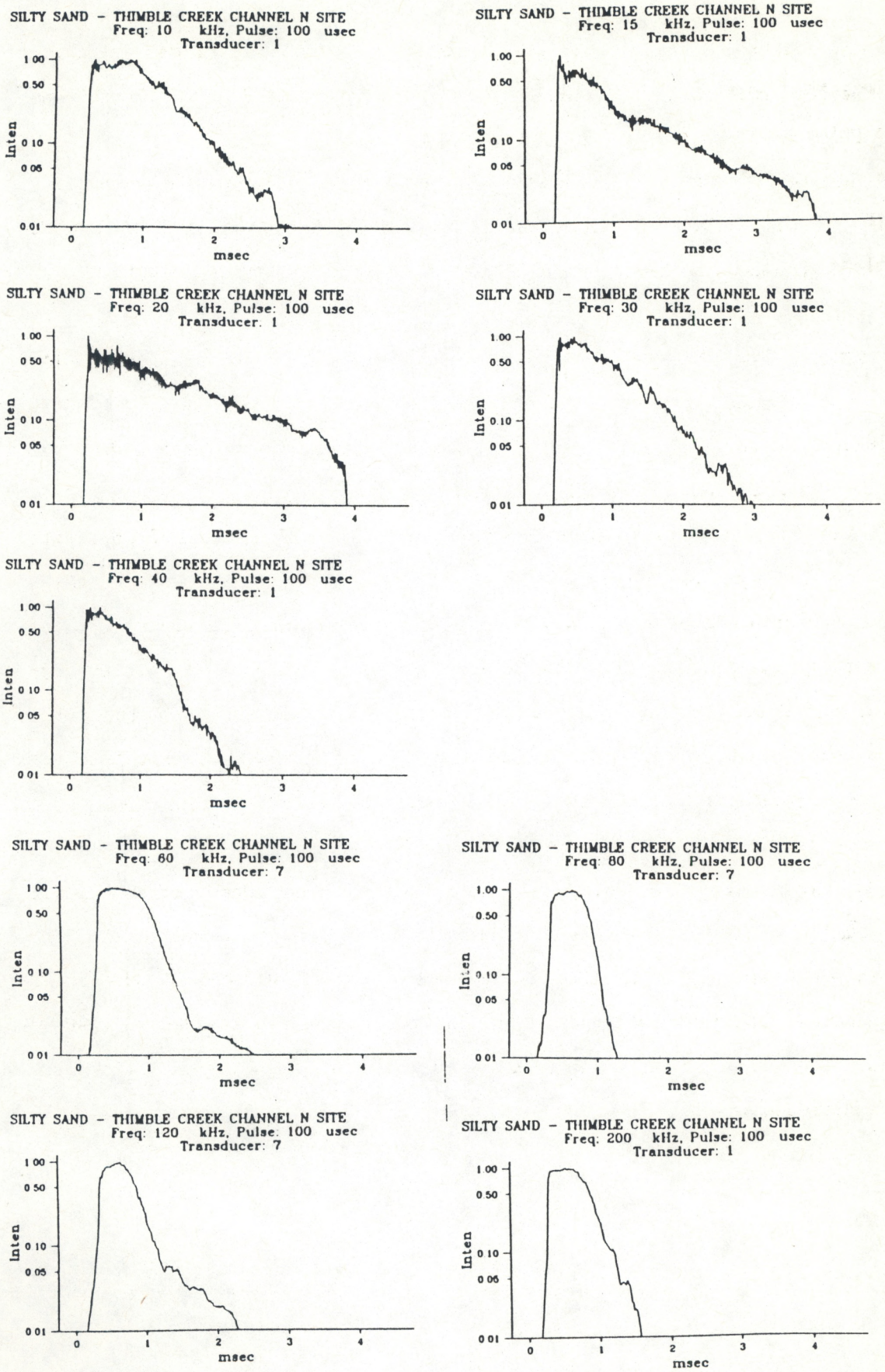

Figure 25. Observed echoes for the Thimble Channel site.

however, the beam pattern narrows and the duration of the surface reverberation is reduced, but at 120 kHz there is again significant broadening of the pulses due to the rapid rise of volume scattering.

The model predictions are shown in Figure 26, and the agreement is fairly good. In particular the volume scattering seen at 120 kHz is well predicted. Some discrepancies do exist; for example, the large coherent peak predicted at 10 kHz is not seen in the data.

Echoes from the off-vertical transducers are shown in Figure 27. As before, transducer 3 is vertical, transducer 4 at 15°, transducer 5 at 30°, and transducer 6 is at 45°. As the angle increases, the pulse broadens out and develops a tail. The first return in the off-vertical beams due to sidelobes is less evident in this data set than in the echoes from Little Creek or the Bay Bridge sites.

The variance over the ensemble of pulses is presented in Figures 28 and 29 as plots of standard deviation of the intensity divided by the intensity; again, the dotted curve reproduces the pulse amplitude, and when the pulse drops below a threshold, the standard deviation is suppressed; this accounts for the jagged appearance of the standard deviation in the pulse tails.

For the most part, the signals are fully random with the normalized standard deviation near unity. Only at the leading edge of the lower frequencies is the standard deviation low enough to suggest a constant target. This is consistent with the expected strong coherent echo at the lower frequencies. During the tails of pulses, the normalized standard deviation rises above one; this is probably due to the combination of signal variability and additive noise.

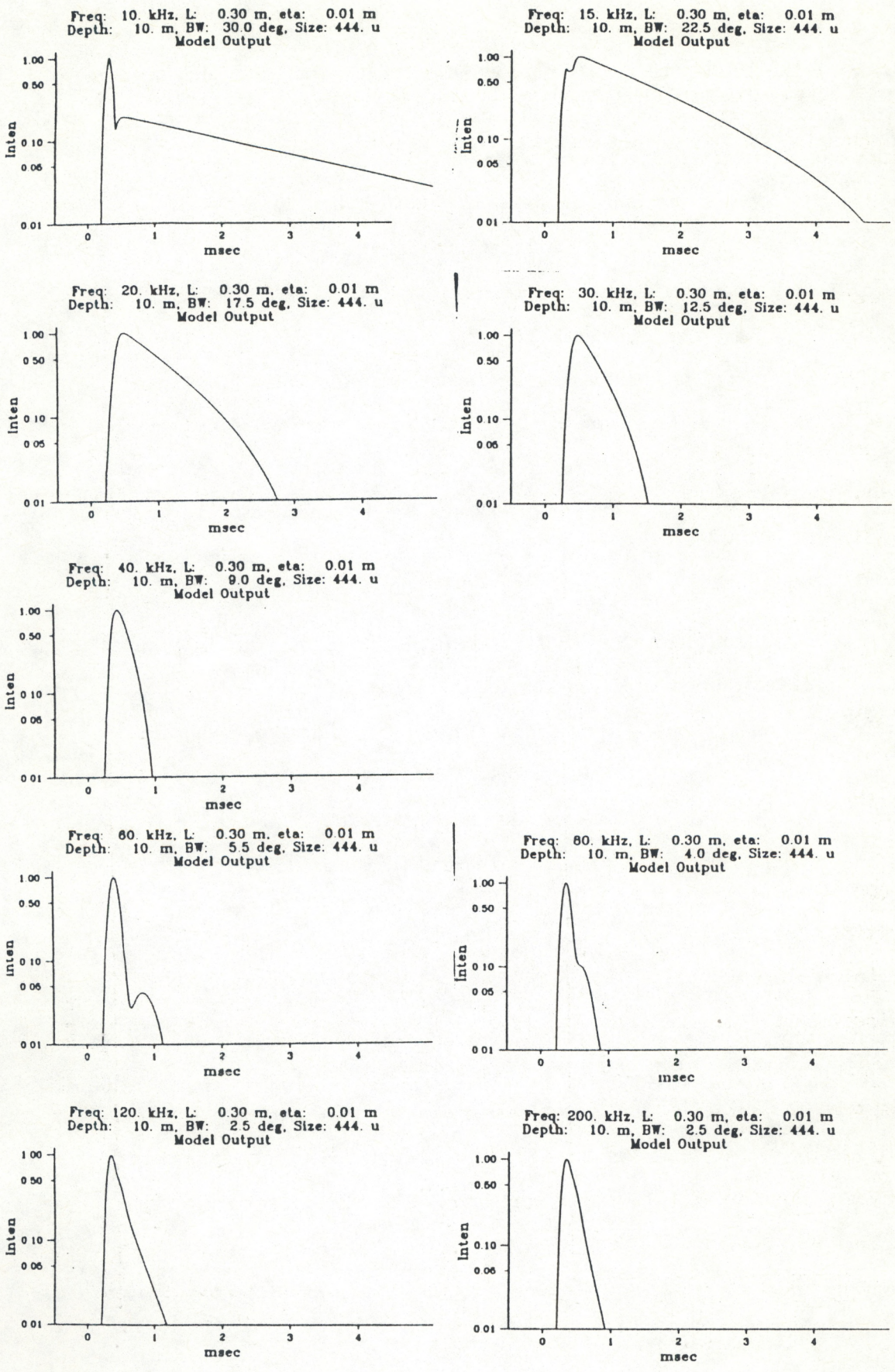

Figure 26. Model predictions for the Thimble Channel site.

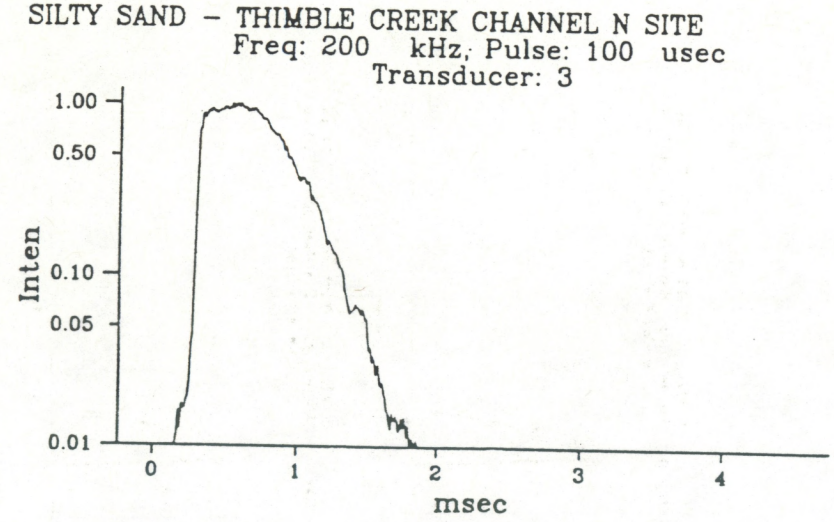

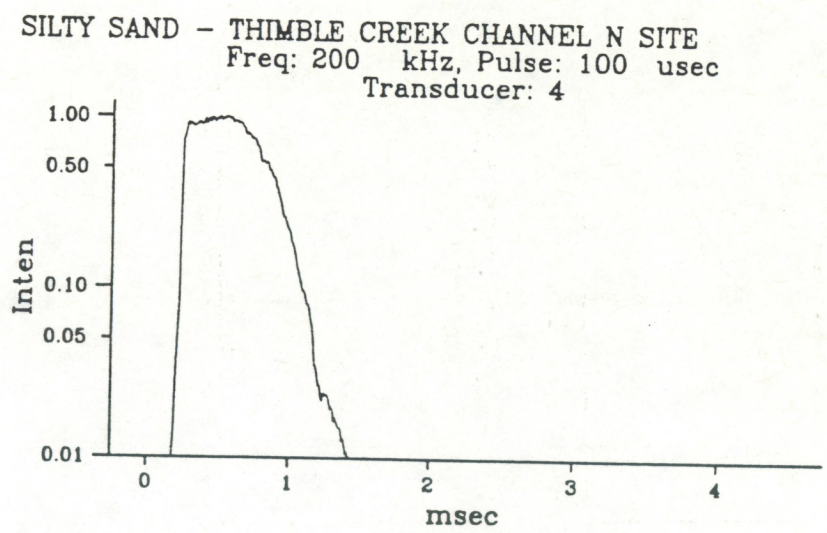

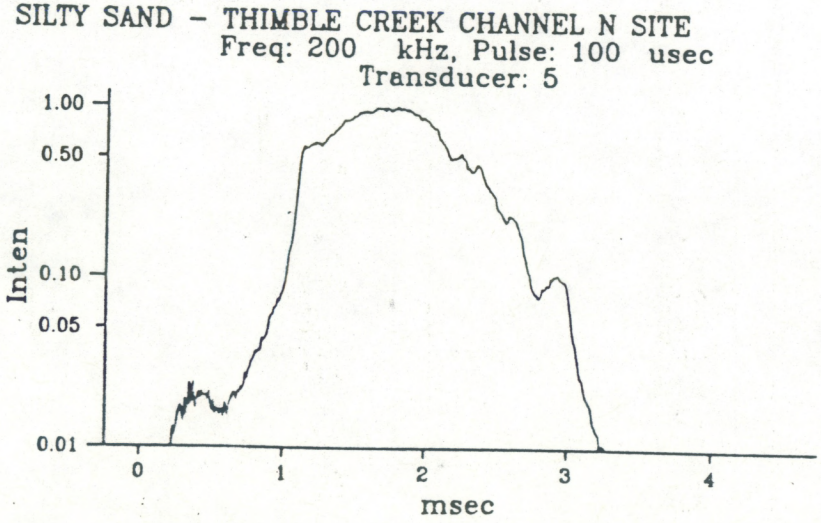

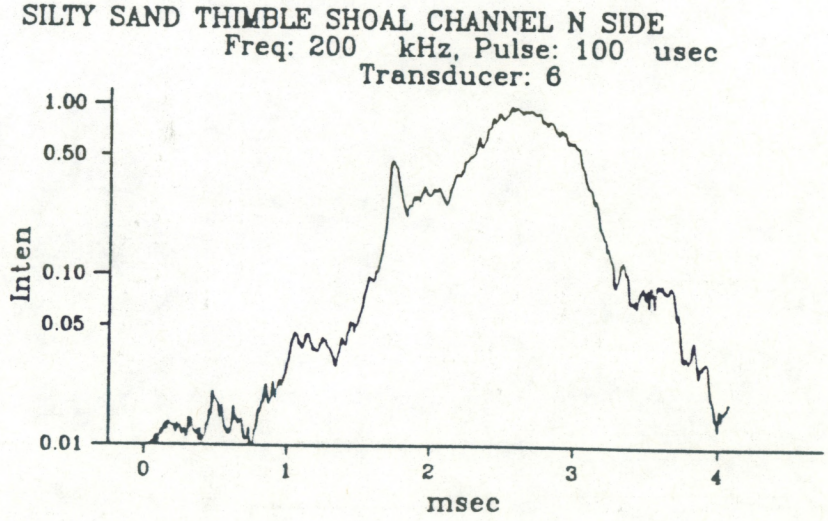

Figure 27. Observed grazing echoes for the Thimble Channel site.

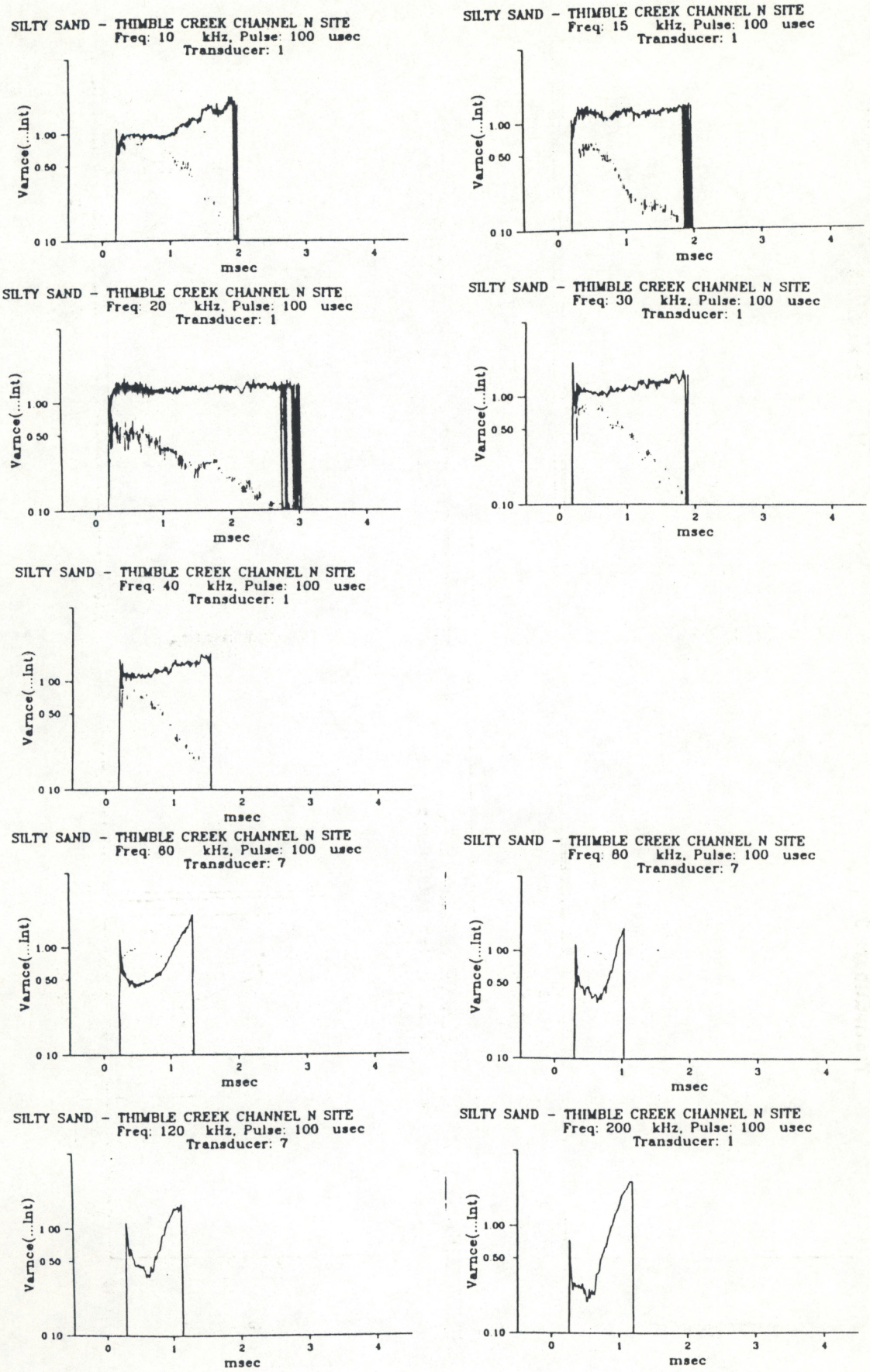

Figure 28. Echo variability for echoes from Thimble Channel.

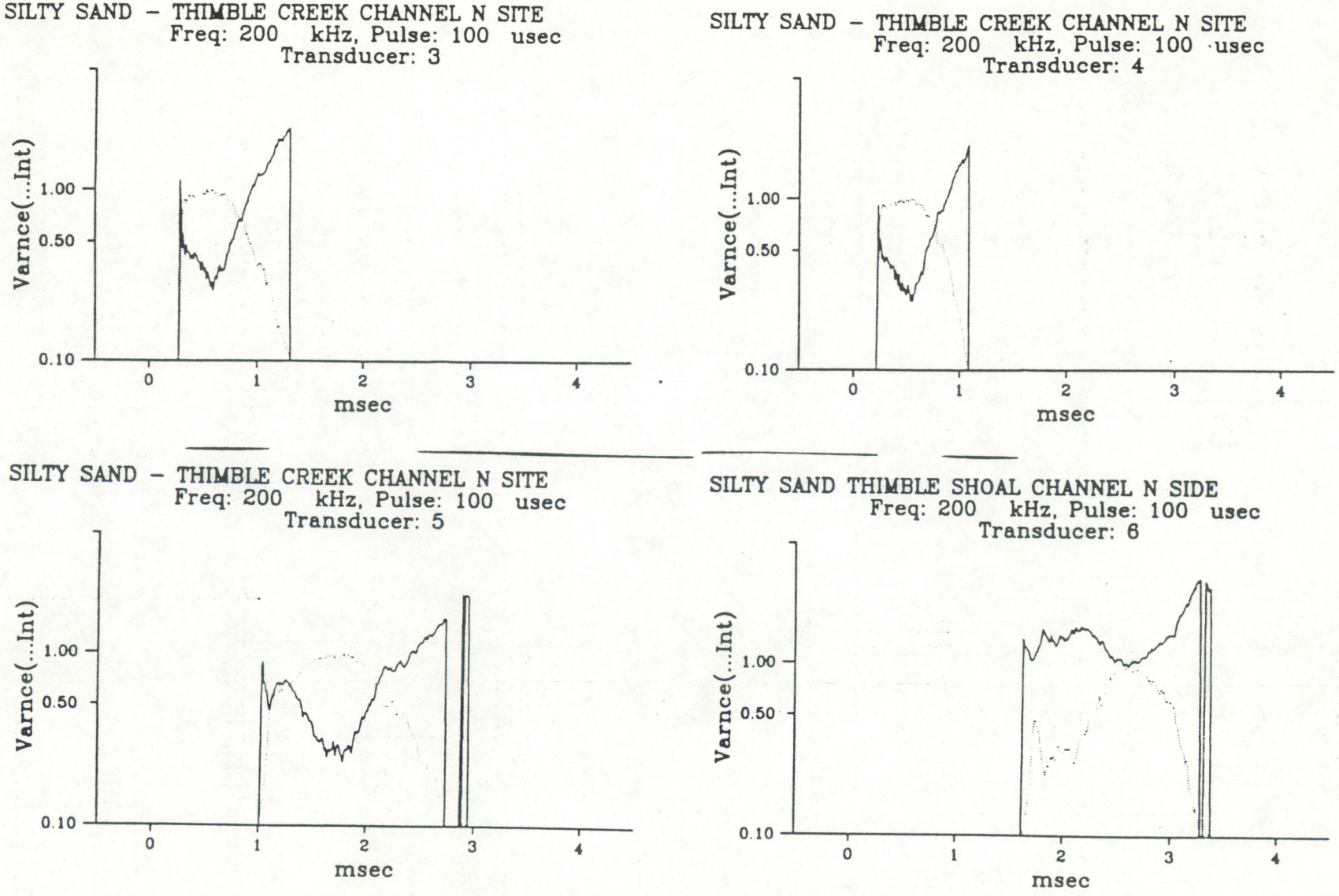

Figure 29. Echo variability for grazing echoes from Thimble Channel.

MIDDLE GROUND DISCUSSION

In many respects, the Middle Ground site resembled the Little Creek site; the bottom at both sites was a sandy silt, although there was less of an admixture of a coarse fraction at the Middle Ground site. As a result, the grain size used for calculations of Rayleigh backscattering was 240 microns. The surface roughness estimated from the track data was estimated to be 16 cm RMS roughness height, with a characteristic length of 2.2 meters. This very rough bottom was likely due to anthropomorphic activity since the middle ground is used as a ship anchorage.

This is the finest sediment encountered during the experiment, but the bottom interface had the roughest surface. As a result the sediment should behave most like an acoustically uniform fluid, producing little backscatter. The rough surface will mean that the echoes are entirely incoherent and random, even at the lowest frequencies. This expectation is born out by the observations shown in Figure 30. The lower frequency pulses are broad as a result of the convolution of individual surface element scattering with the broad transducer beam pattern. The 10 kHz pulse is unexpectedly narrow, however; we have no explanation for this now. Above 80 kHz, however, the pulses narrow down as the transducer beam-widths narrow. An anomaly occurs at 60 kHz in the form a a narrow pulse, equal to transmitted pulse width, at the start of the pulse. This may be due to some coincidence between the side lobe angle at 60 kHz, and the characteristic slope of the bottom roughness resulting in a direct reflection of the side lobes off the sides of bottom roughness elements.

The model predictions are shown in Figure 31, and the agreement is fairly good, except for the unusual cases noted above.

Echoes from the off-vertical transducers are shown in Figure 32. Transducer 3 is vertical, transducer 4 at 15°, transducer 5 at 30°, and

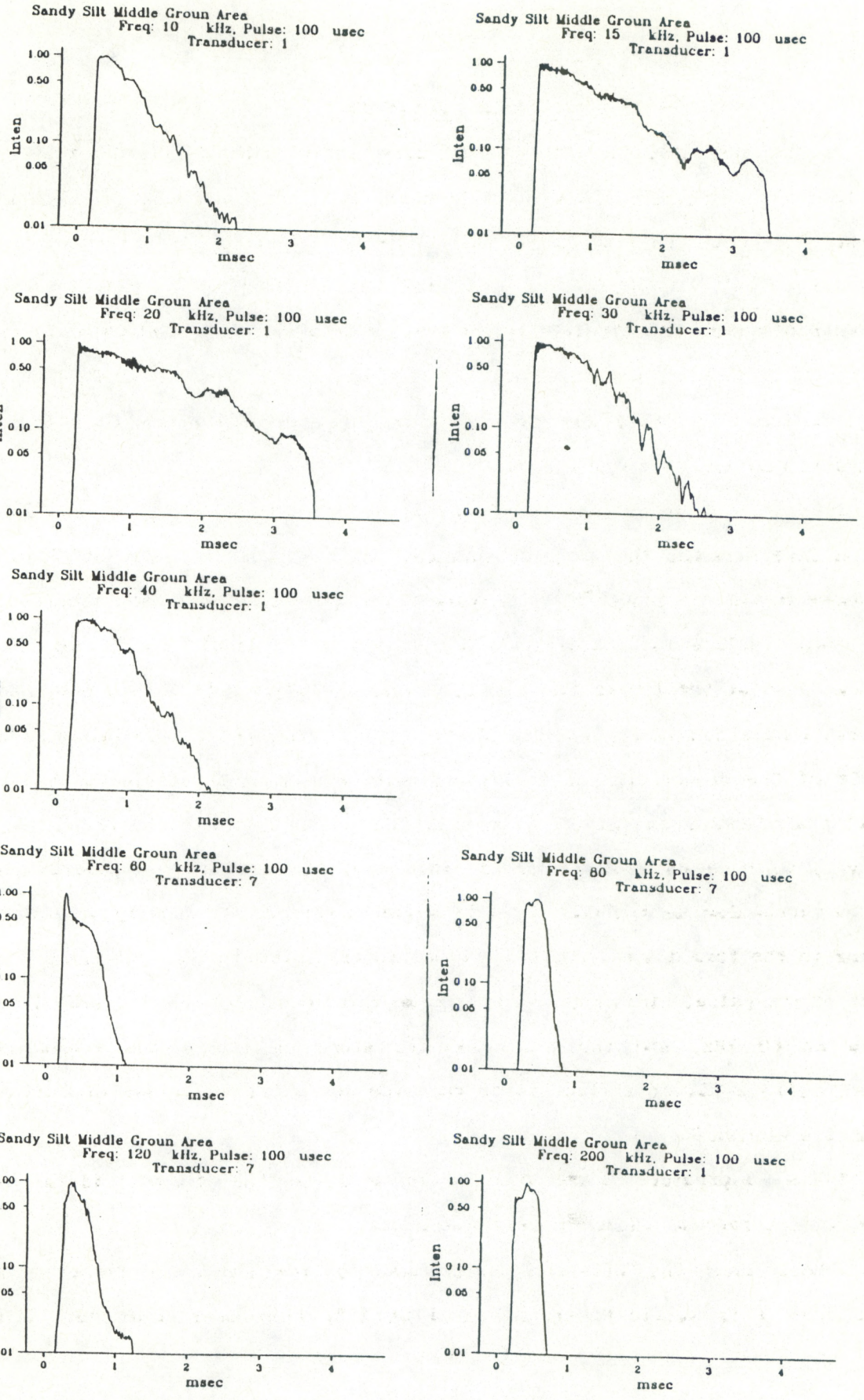

Figure 30. Observed echoes for the Middle Ground site.

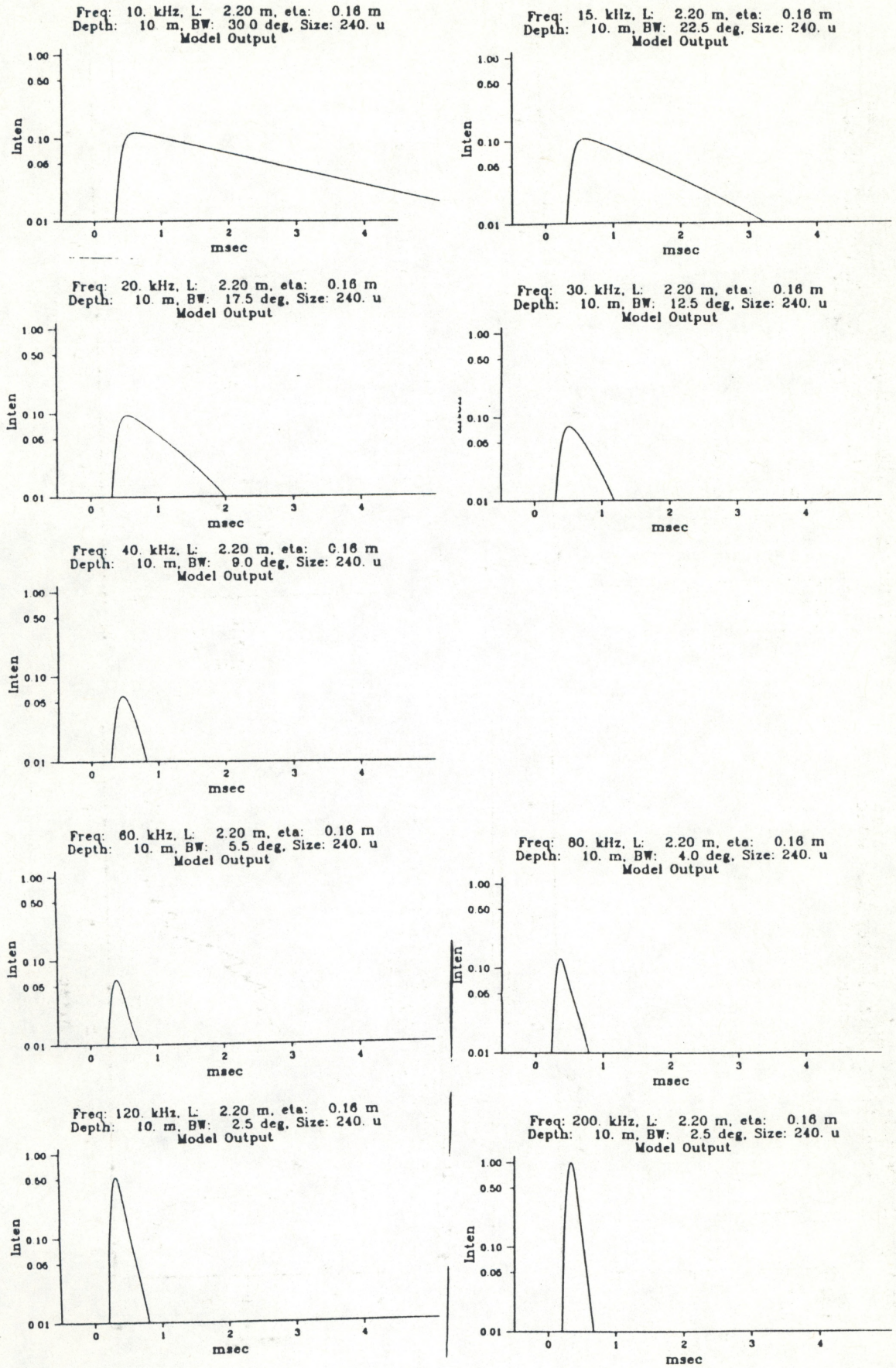

Figure 31. Model predictions for the Middle Ground site.

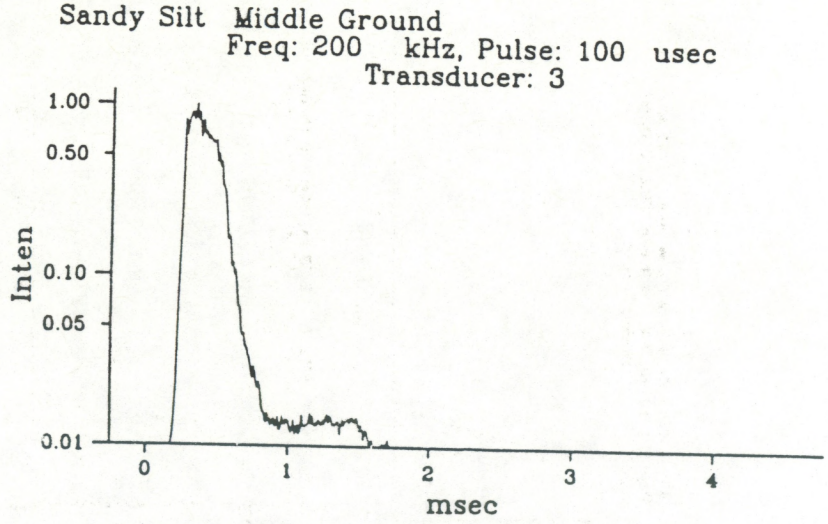

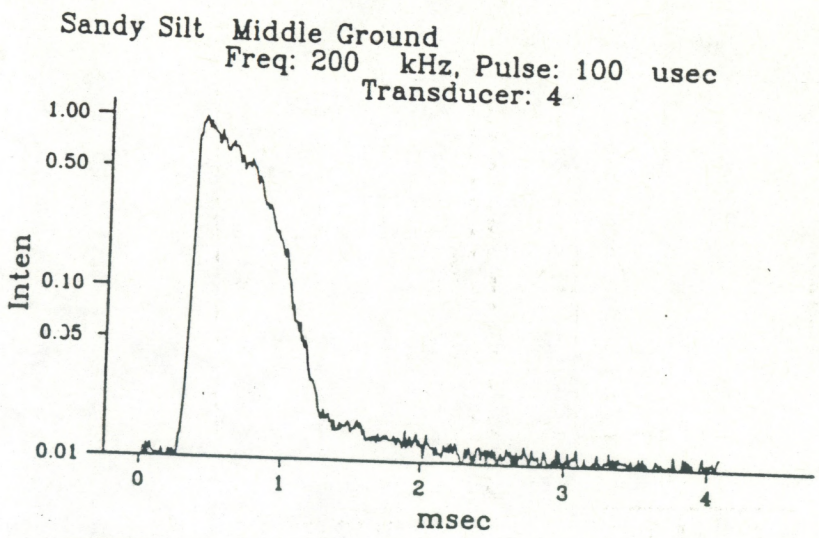

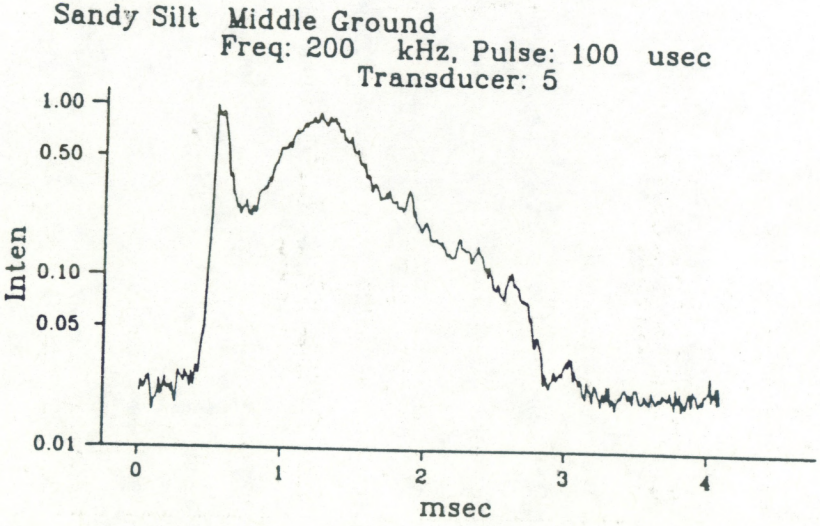

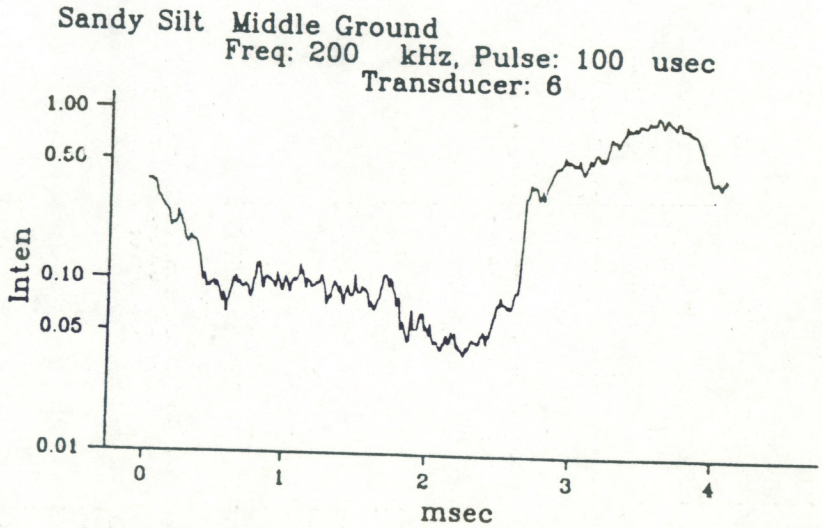

Figure 32. Observed grazing echoes for the Middle Ground site.

transducer 6 is at 45°. The first returns in the off-vertical beams are due to sidelobes. This is most evident for transducer 5 where a very narrow sidelobe return precedes the main body of the pulse by over a millisecond.

The variance over the ensemble of pulses was calculated and is presented in Figures 33 and 34 as plots of standard deviation of the intensity divided by the intensity; the dotted curve reproduces the pulse amplitude. When the pulse drops below a threshold, the standard deviation has been suppressed; this accounts for the jagged appearance of may of the graphs.

For the most part, the signals are fully random with the normalized standard deviation near unity. Only at the leading edge of the 10 kHz pulse frequencies is the standard deviation significantly below unity. Even during the anomalous narrow pulse at 60 kHz, the standard deviation is high, supporting the hypothesis that this anomaly is due to interaction of side lobes with random roughness elements, rather than an echo from some locally strong target such as a rock.

DODGE ISLAND BOTTOM DISCUSSION

The bottom at the Dodge Island site consisted of a mix of sediment types ranging from silt to coarse shell hash. As a result the grain size used for calculations of Rayleigh backscattering was 600 microns reflecting the heavy weighting toward larger sized provided by the Rayleigh scattering function. The surface roughness estimated from the track data was estimated to be 4 cm RMS roughness height, with a characteristic length of 1.1 meters.

Thus, as with the Thimble Channel site, the bottom is smooth enough that one expects some coherent component to the echoes at lower frequencies. At the same time there should be a good deal of volume scattering even at lower frequencies because of the coarseness of the sediment. This expectation is born out for the most part by the observations shown in Figure 35. The lower

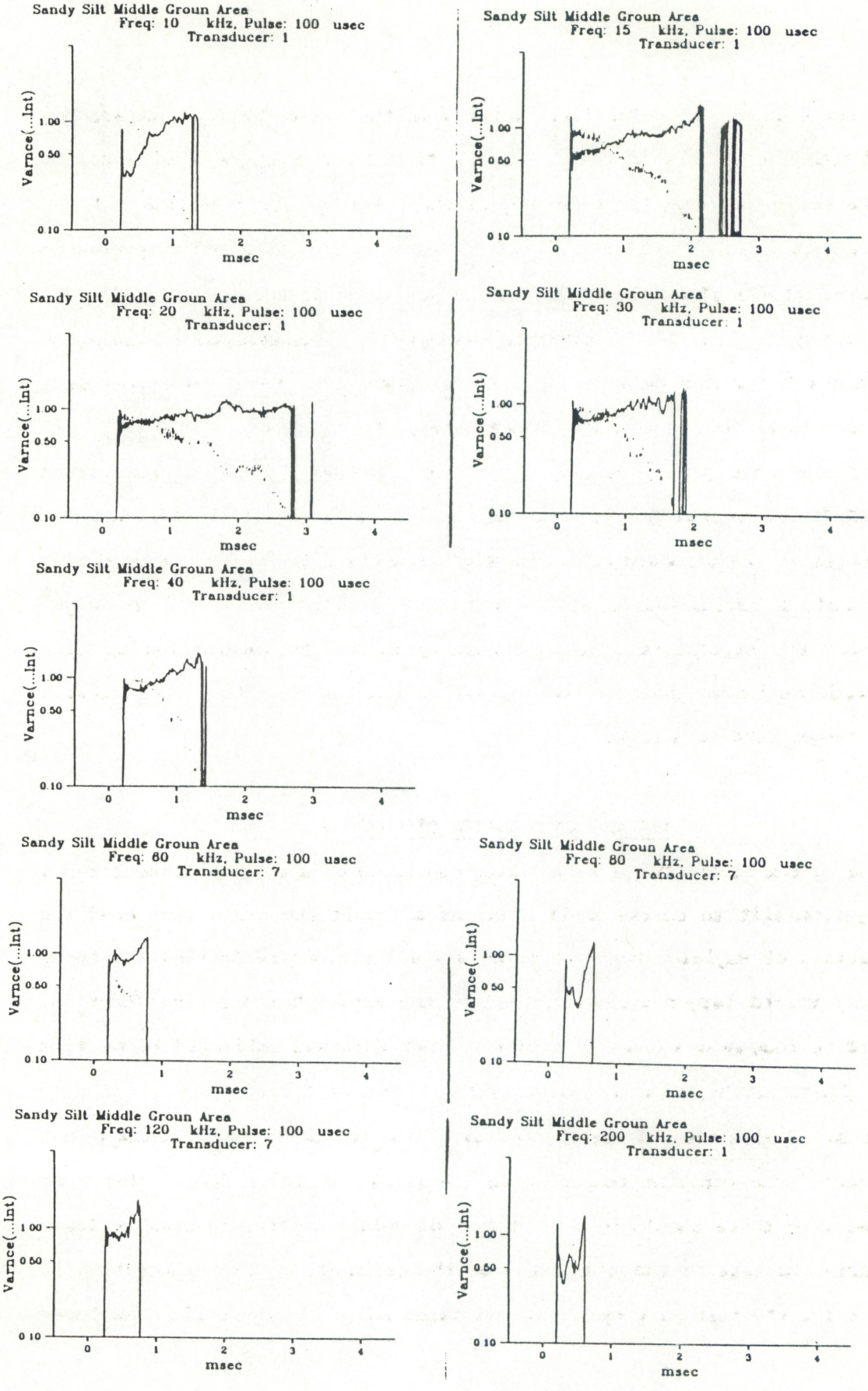

Figure 33. Echo variability for echoes from Middle Ground.

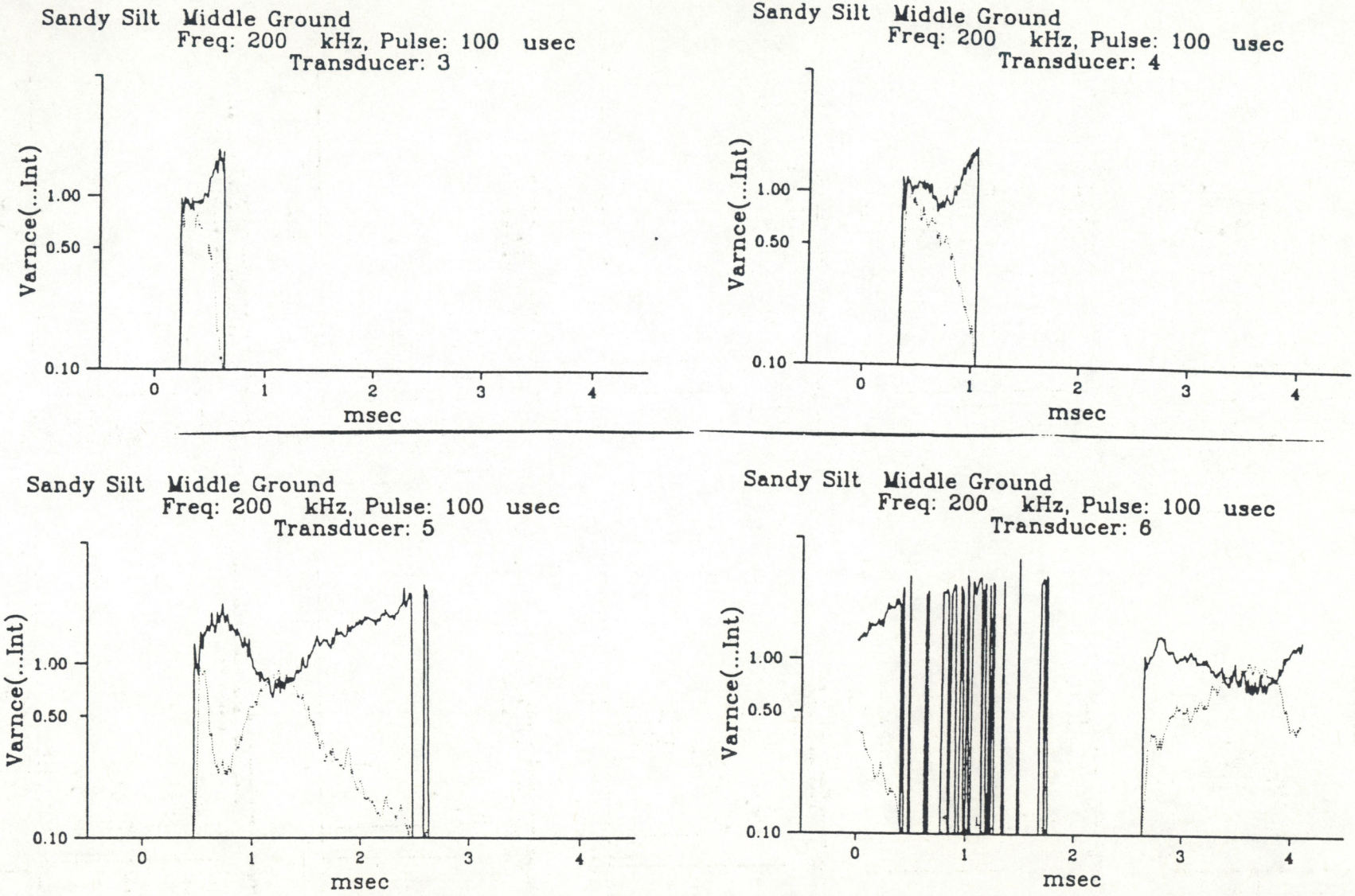

Figure 34. Echo variability for grazing echoes from Middle Ground.

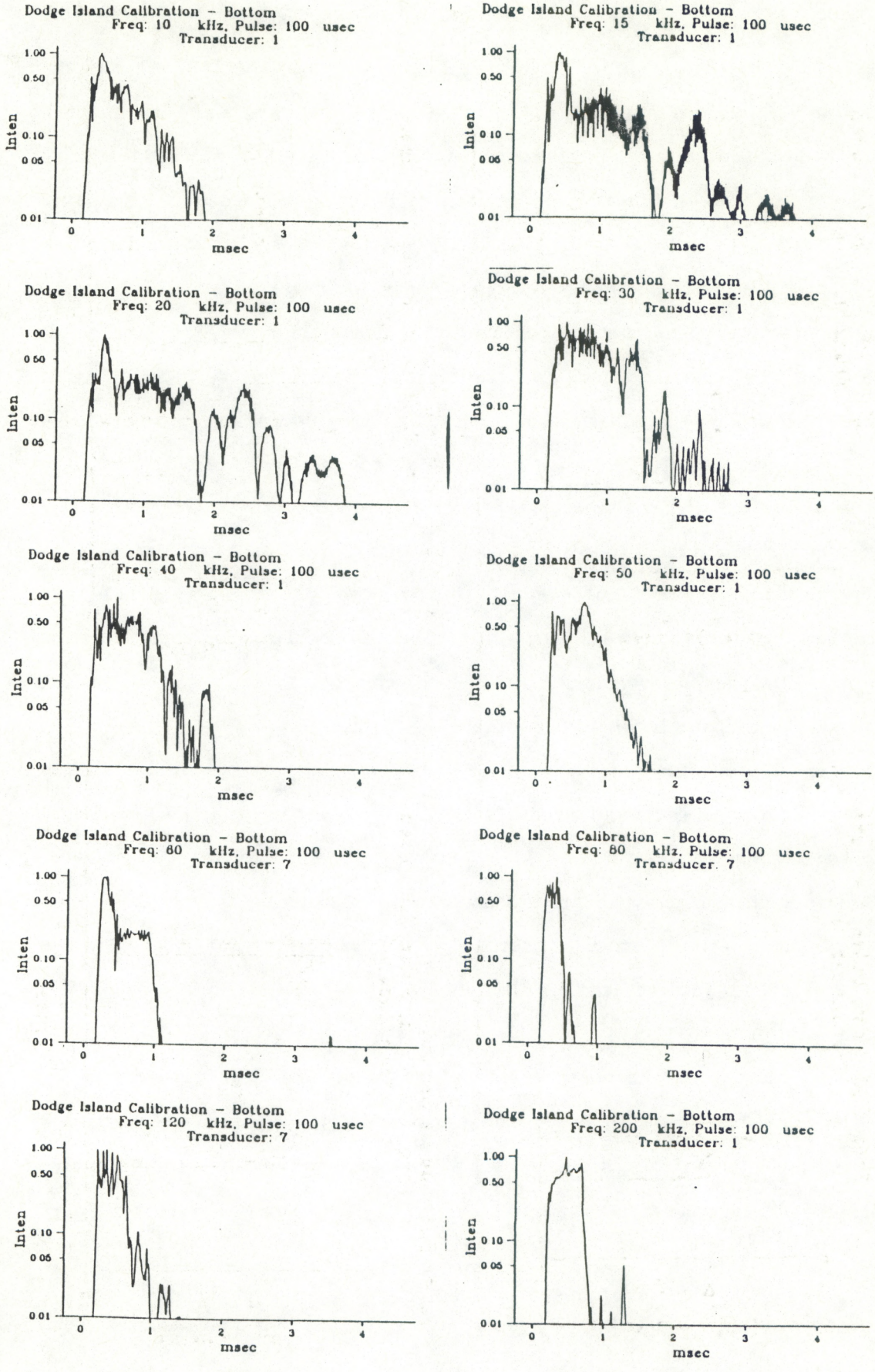

Figure 35. Observed echoes for the Dodge Island site.

frequency pulses are broad as a result of the combination of surface scattering with volume scattering. Above 80 kHz, however, the beam pattern narrows and the duration of the surface reverberation is reduced, but at 120 kHz there is again significant broadening of the pulses due to the rapid rise of volume scattering. At 60 kHz there is a curious shelving of the pulse which is probably due to some sort of roughness/sidelobe interaction.

A new feature seen in these echoes is the detailed temporal structure in the tails of the echoes. Since the transducer platform was suspended from a shore-mounted crane, there was no ship motion to provide an ensemble of echoes as in the previous data sets. At Dodge Island each echo was essentially identical, so that what is seen is the detailed interaction of the transducer beam pattern, the surface roughness, and the volume scattering as mapped into the time domain. In particular at 15 kHz a remnant of the original 15 kHz transmitted frequency can be seen in the fine oscillations of the echo waveform. In the observations taken from the R/V Laidly, such coherent details were wiped out by the ship motion.

The model predictions are shown in Figure 36, and the agreement is fairly good. In particular the model predicts the shelving behavior at 60 kHz due to volume scattering.

Echoes from the off-vertical transducers are shown in Figure 37. The complicated echo structure caused by the prominence of the sidelobe returns, and the interaction of the off-vertical beam with the roughness elements is clear.

The variance over the ensemble of pulses is presented in Figures 38 and 39. There are no surprises here; for the most part, the signals are fully random with the normalized standard deviation near unity. It is interesting to note that the standard deviation is relatively low during the initial part

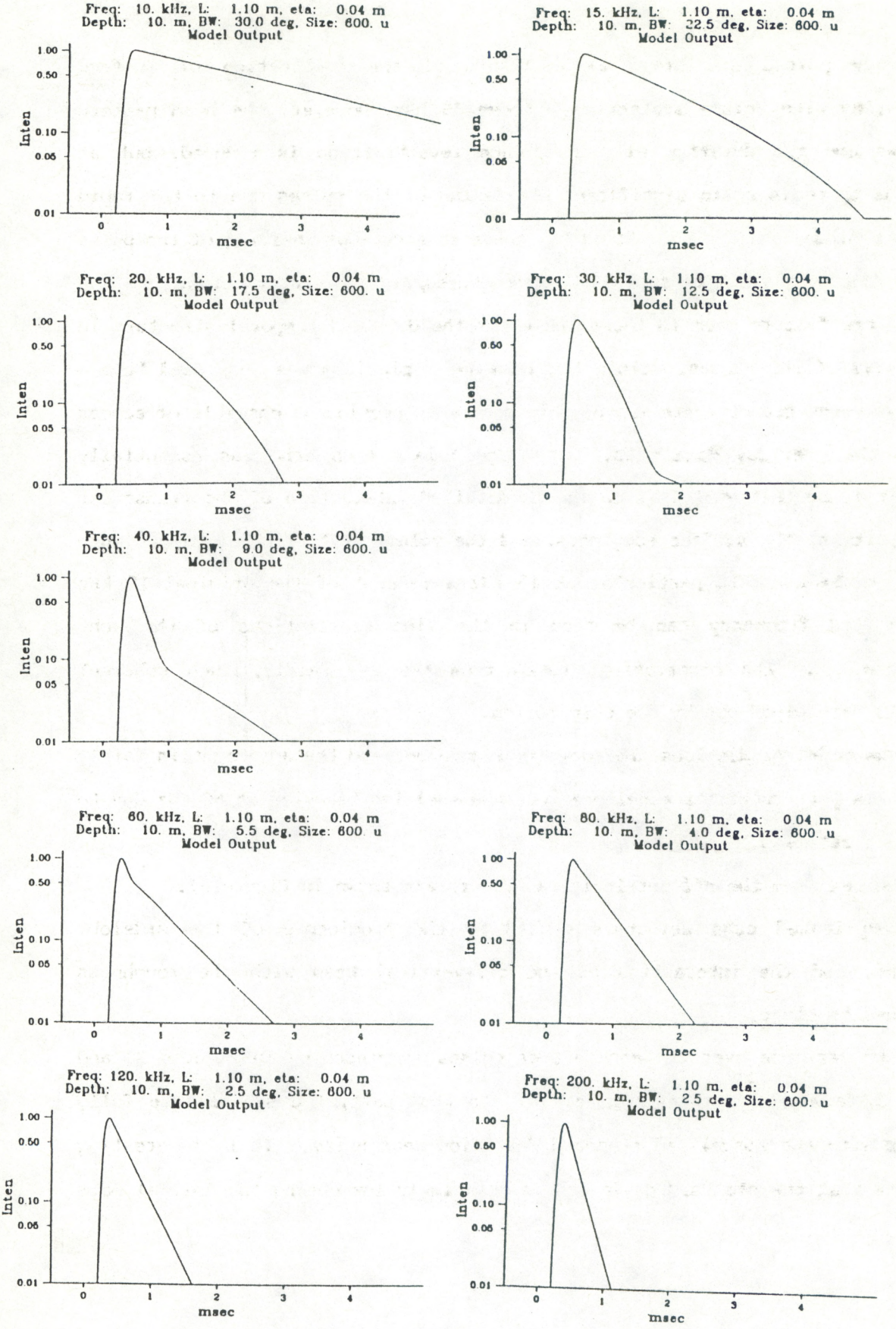

Figure 36. Model predictions for the Dodge Island site.

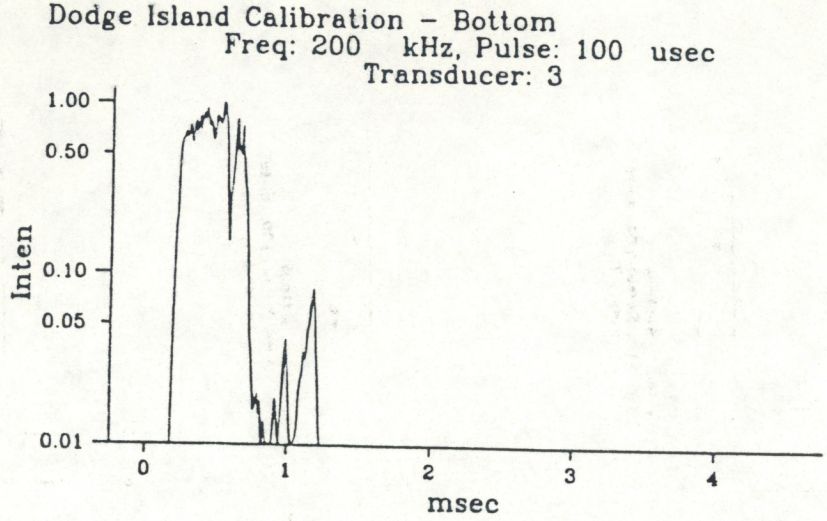

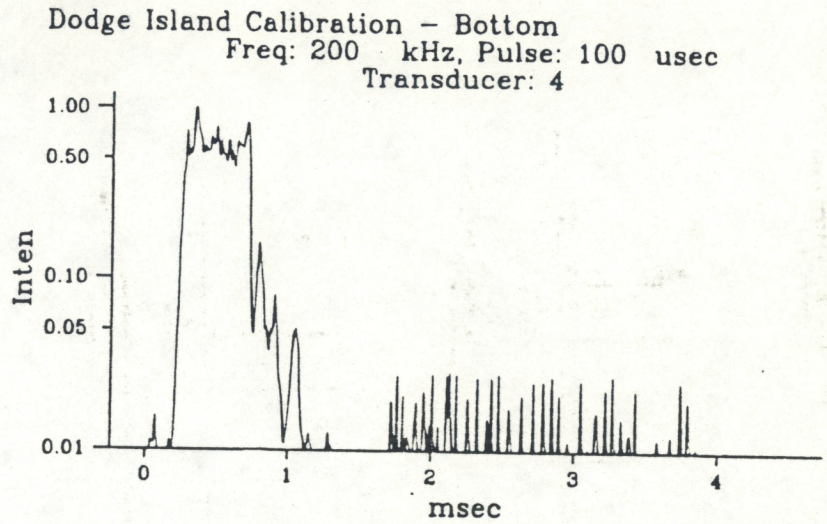

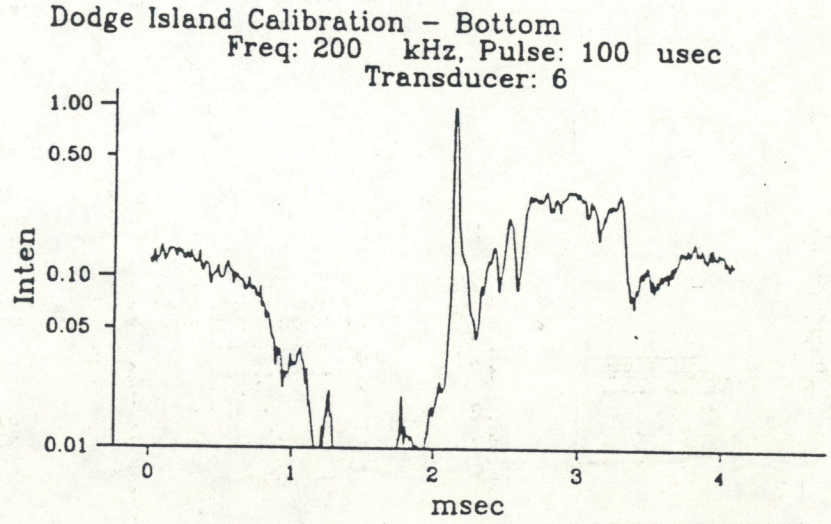

Figure 37. Observed grazing echoes for the Dodge Island site.

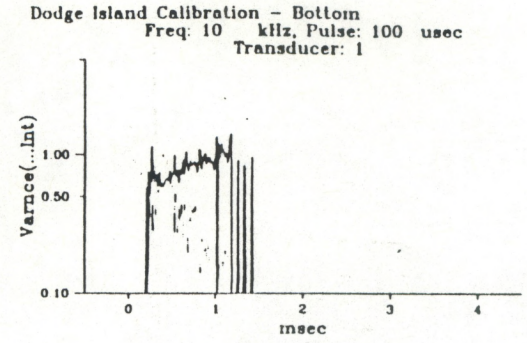

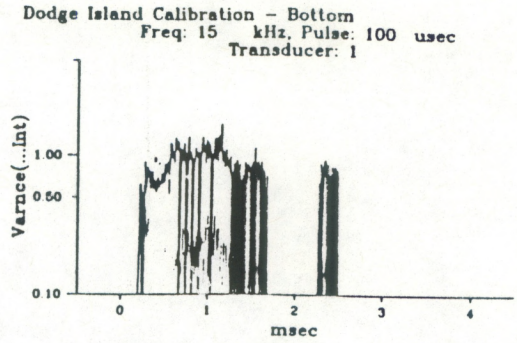

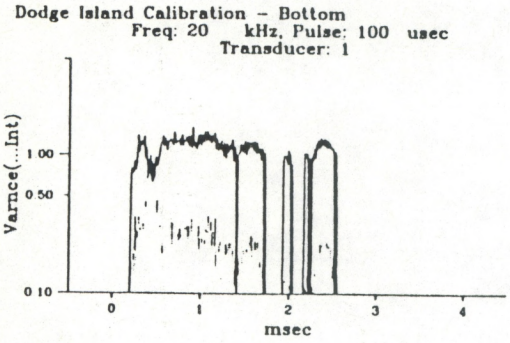

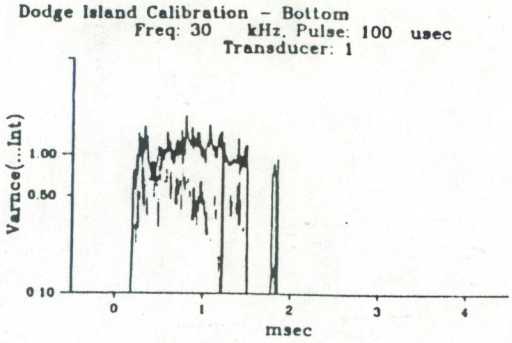

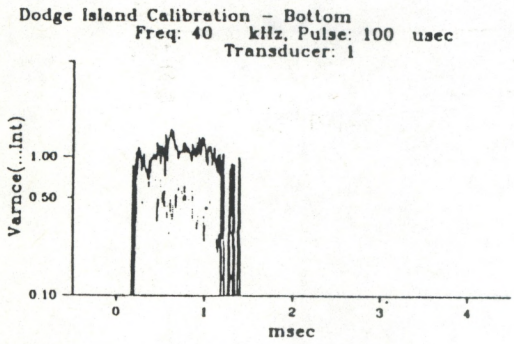

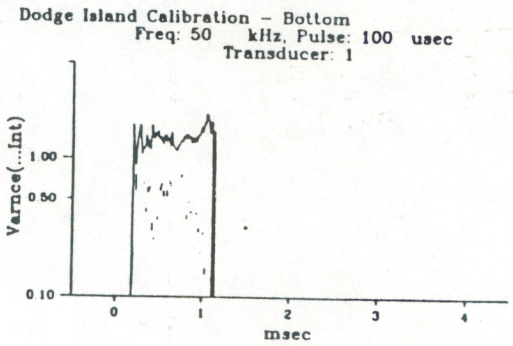

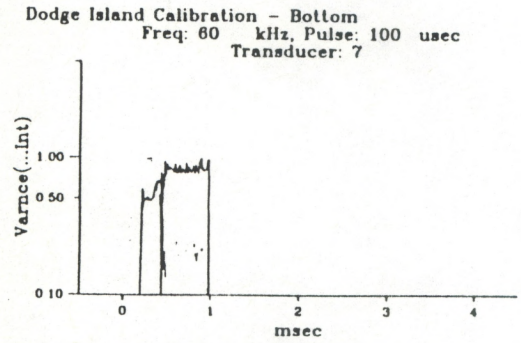

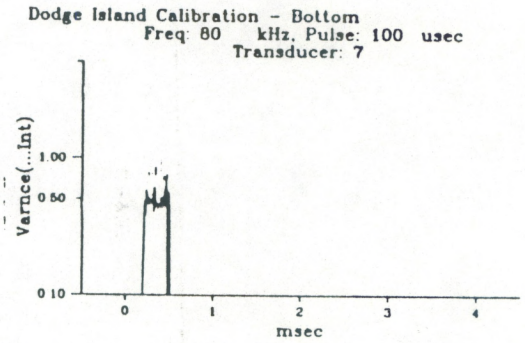

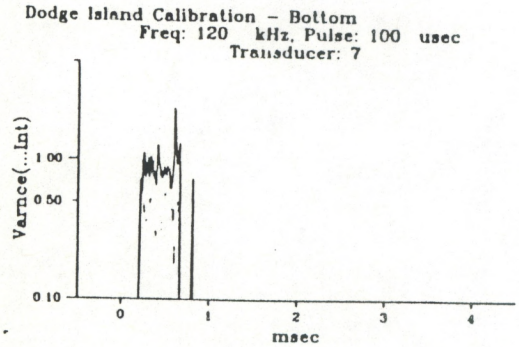

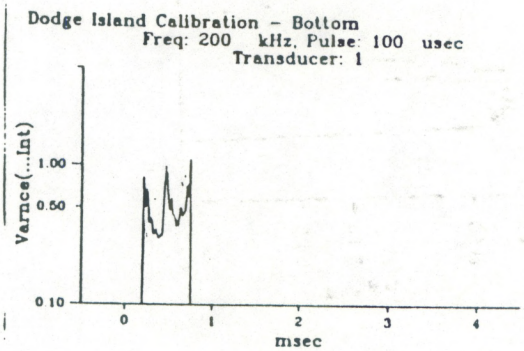

Figure 38. Echo variability for echoes from Dodge Island.

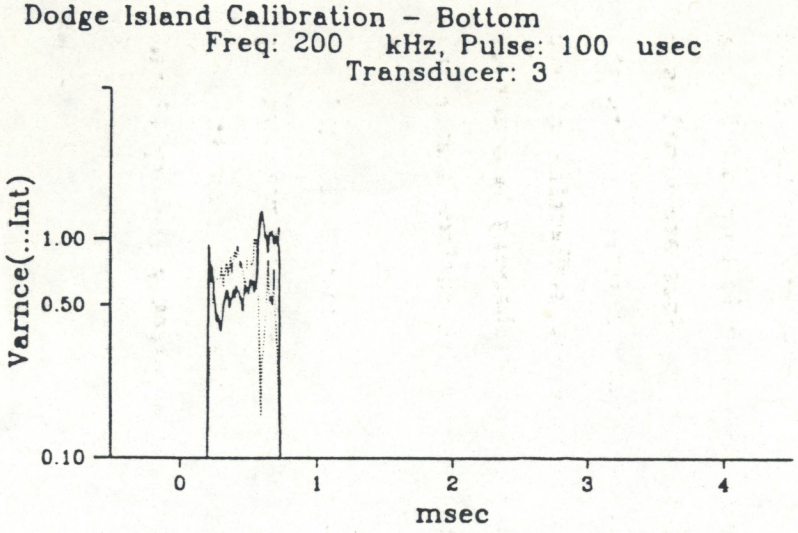

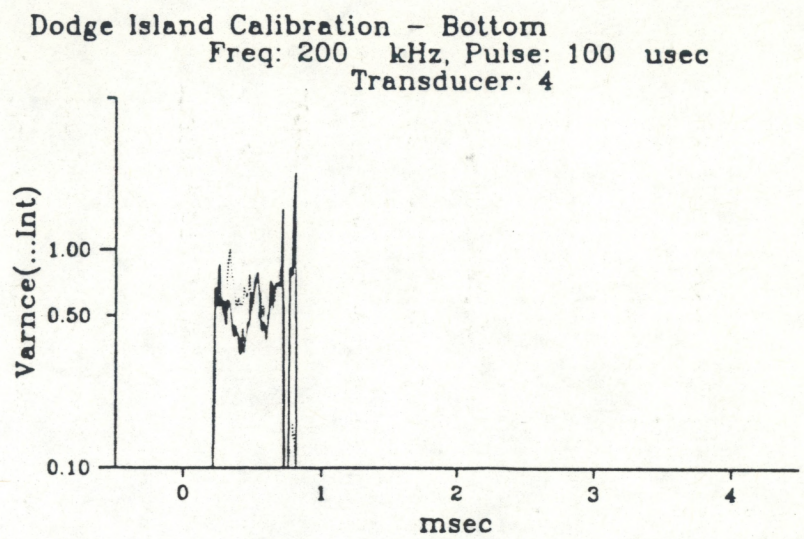

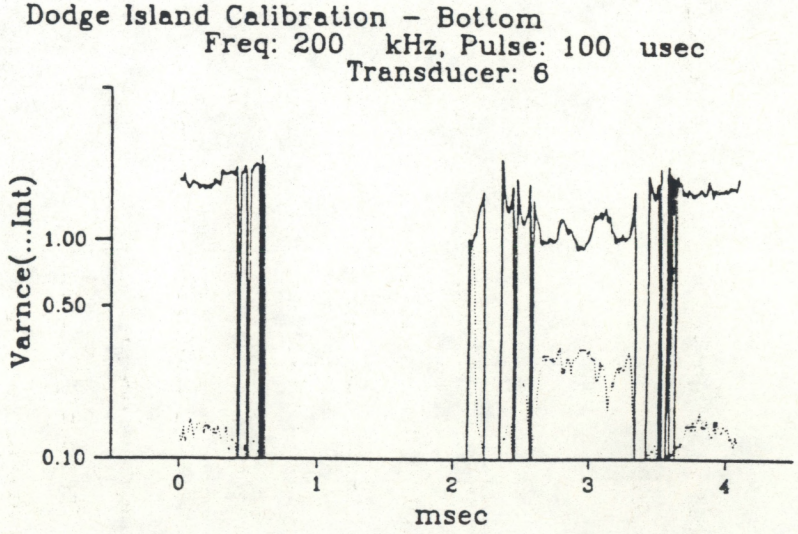

Figure 39. Echo variability for grazing echoes from Dodge Island.

of pulse at 60 kHz, during the shelve or tail due to volume scattering the variability rises.

DODGE ISLAND SURFACE DISCUSSION

At Dodge Island the transducer array was lowered to the bottom to ping upward at the surface in inverted echo sounder (IES) fashion. The provided a pure test case since the only scattering from the sea water/air interface should be surface scattering; essentially no sound penetrates this boundary. In addition to its utility as a pure surface scattering test case, these measurements may serve as a scale model for the operation of IES instruments in the deep ocean.

Obviously, grain size is not relevant to this case, and no precision estimate of surface roughness is available. On the day of the experiment, the harbor was fairly calm, however, with a roughness of perhaps 10-20 cm. This surface is rough enough, so that the echoes should be entirely incoherent and random, even at the lowest frequencies. This expectation is born out by the observations shown in Figure 40. The lower frequency pulses are broad as a result of the convolution of individual surface element scattering with the broad transducer beam pattern, but a trace of coherent reflection of the transmitted pulse persists up to 20 kHz. The peculiar shelving behavior is again seen in the 60 kHz echo, but now it must be due to surface scattering effects.

Echoes from the off-vertical transducers are shown in Figure 41. This is most evident for transducer 5 where a very narrow sidelobe return precedes the main body of the pulse by over a millisecond. The echo from the 45° transducer 6 is largely structureless noise; there apparently is very little direct backscatter at this angle.

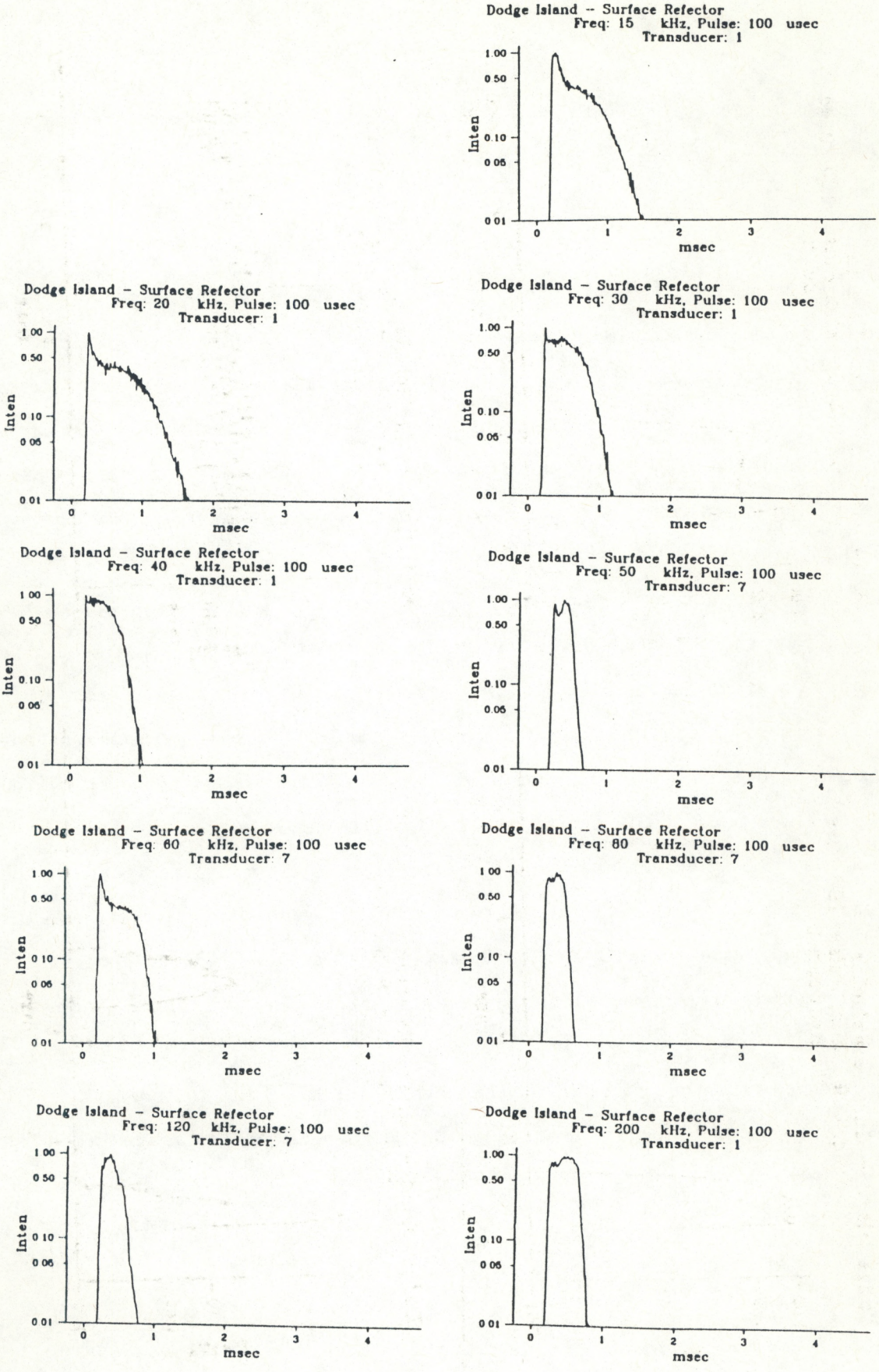

Figure 40. Observed echoes from the surface at Dodge Island.

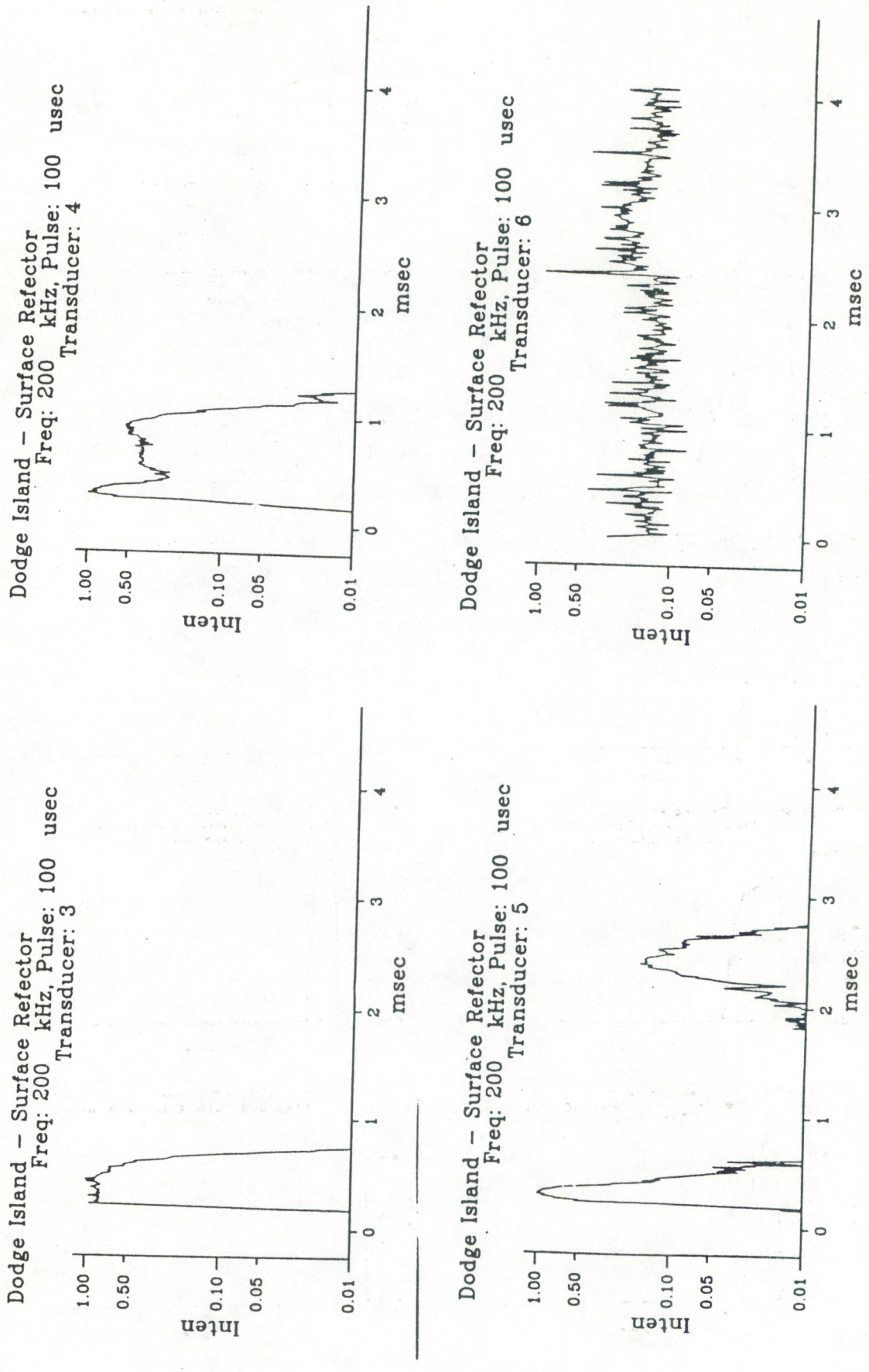

Figure 41. Observed grazing echoes from the surface at Dodge Island.

The scattering that gives rise to these echoes can be more clearly visualized from the waterfall plots of Figure 42. At vertical incidence (transducer 3) the individually scattered replicas of the transmitted pulse that convolve to form the average echo waveform are reflected in the fine structure of individual pulses. The narrow pulse that occurs at progressively later times in each pulse is due to spurious electronic noise. At 15° (transducer 4) the main lobe and sidelobes are not clearly separated in time so the individual pulse echoes are a broad combination of sound from these two sources. At 30°, the main lobe and side lobes are well separated and this is reflected in the average pulse of Figure 41. The 45° beam has only a trace of echo from the side-lobes, but very little other recognizable scatterers. One feature of note is a slow periodicity in the scattering probably due to variation in roughness as wave trains passed through the ensonified area of the surface. Initially up to pulse 10, there is little scattering except for what is apparently a side-lobe echo. From pulses 10-20, there is an increase in diffuse scattering and the sidelobe echo decreases. Around echo 20, the diffuse scattering decreases before picking up by echo 30. This pattern repeats several times, although not as clearly, during the remainder of the pulses. This illustrates the clear dependence of the echo waveform on the surface roughness.

The variance of the pulses is presented in Figures 43 and 44 as plots of normalized standard deviation of the intensity. For the most part, the signals are fully random with the normalized standard deviation near unity. Only at the leading edge of the lower frequency pulses is the standard deviation significantly below unity. Even during the anomalous narrow pulse at 60 kHz, the standard deviation is high, supporting the hypothesis that this anomaly is due to interaction of side lobes with the random surface roughness.

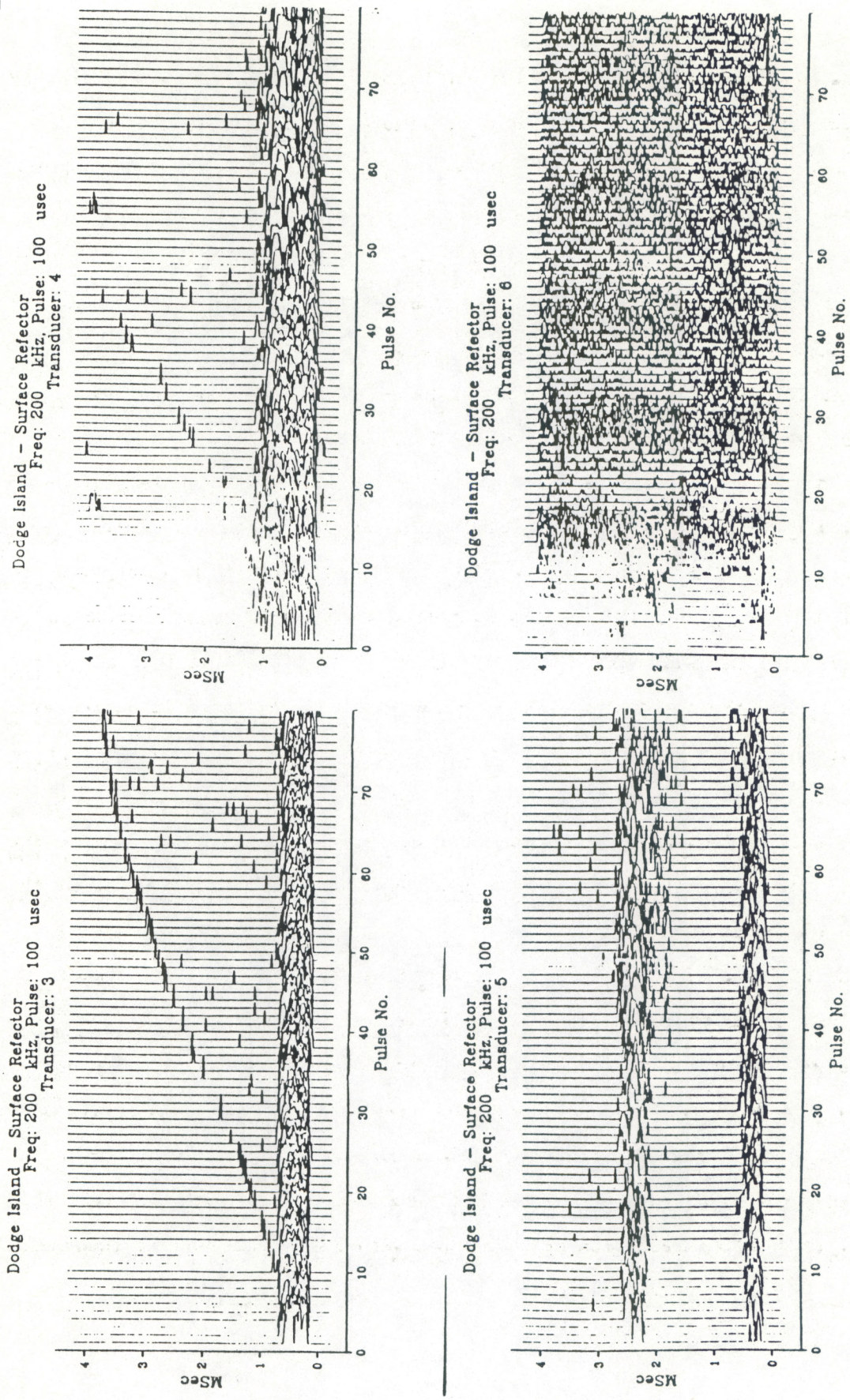

Figure 42. Waterfall plot of grazing echoes from the surface.

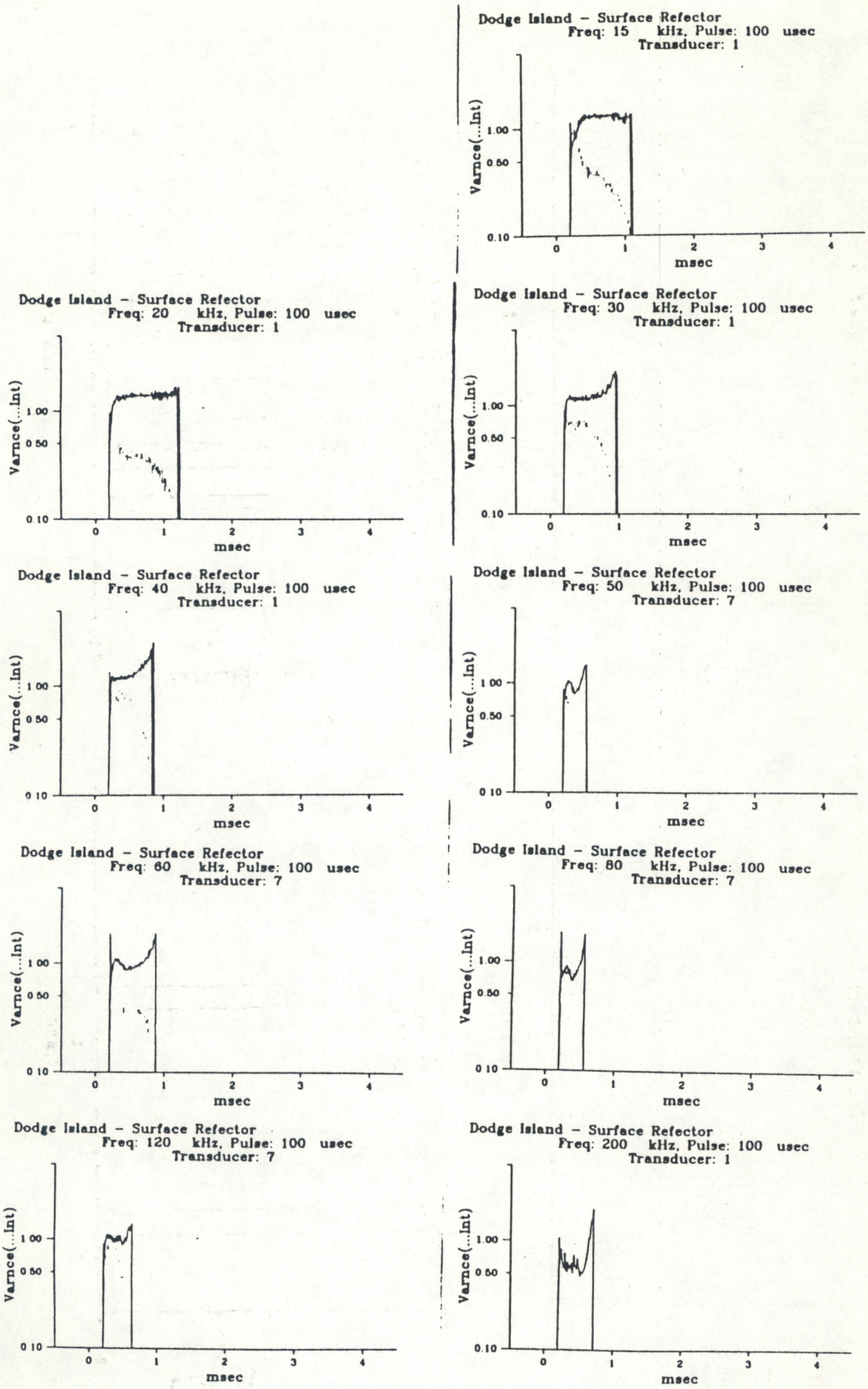

Figure 43. Echo variability for echoes for surface.

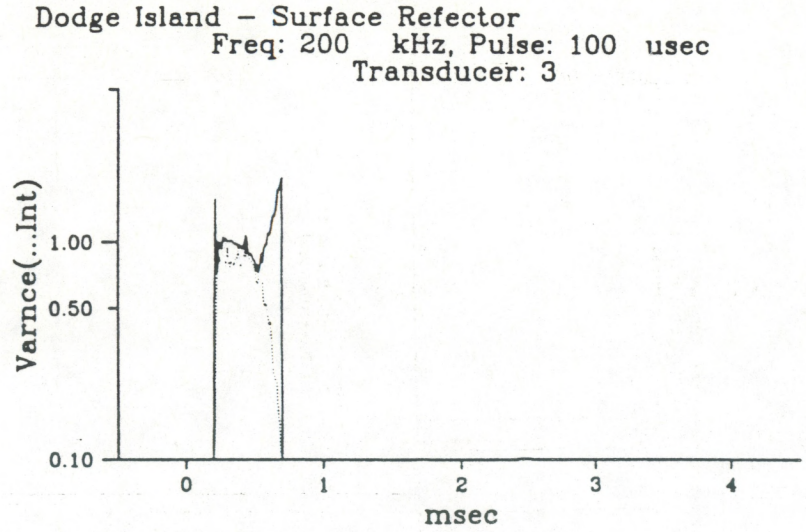

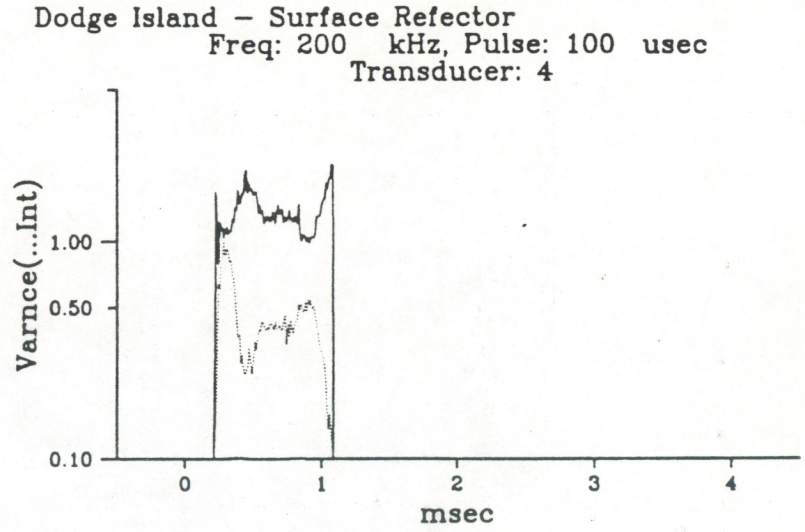

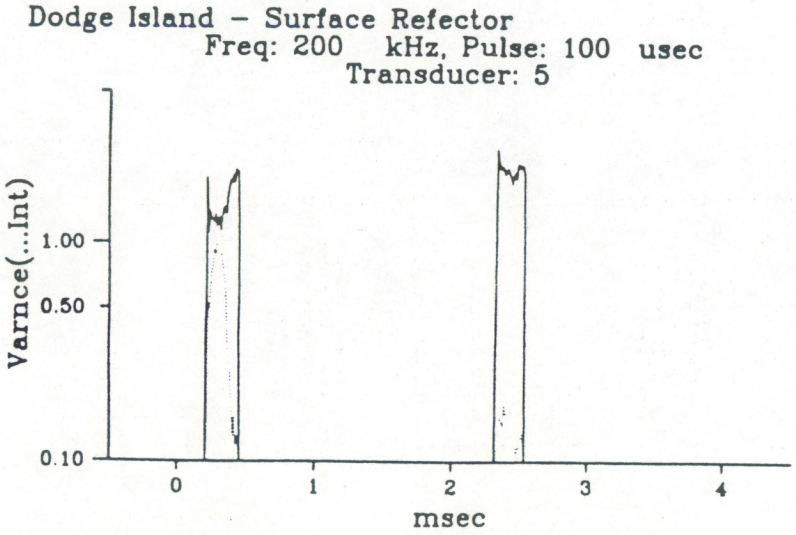

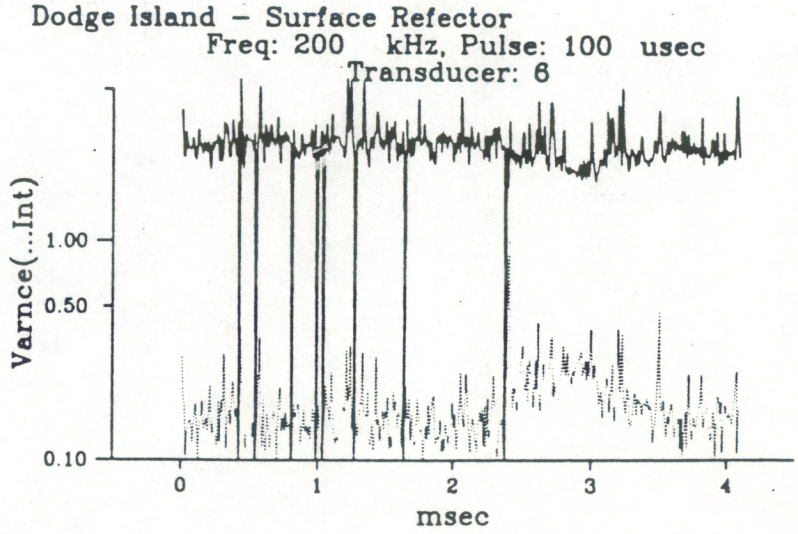

Figure 44. Echo variability for grazing echoes from surface.

CONCLUSION AND RECOMMENDATIONS

The ability of this model to easily generate sample echoes from a wide range of bottom types permits a pattern recognition approach to be taken to the problem of extracting information from the echo signals. In general terms, an algorithm for discrimination between bottom echoes will be based upon some (possibly vector) parameter P. Starting with some initial parameter value P_0, the algorithm is "trained to recognize the echoes by determining a succession of values of the parameter P_i, i = 1..., based on the success of the algorithm on the ith echo."

Perhaps the simplest discrimination algorithm uses linear discrimination. That is, if X is the vector of echo data, the parameter vector P, then the data is classified according to the sign of $X \cdot P = \Sigma X(f,t)P(f,t)$ where f is the frequency of the echo and t measures is time at which the echo amplitude is measured.

The training algorithm for linear discrimination is simple. Start with an initial value P_0, then for the set of data {X}, let $P_i = P_{i-1} + X$ if the echo is misclassified, that is, if the sign of $X \cdot P$ is wrong. If the set of echoes can be correctly classified on the basis of a linear discriminant, then it can be shown that this algorithm converges to a parameter P that correctly classifies the echoes.

For the echo sounding case a program was written in which the echo vector X had thirty components. These were samples of echoes at five different frequencies 10, 20, 40, 80, and 160 kHz at 6 different delay times beginning with the beginning of the echo waveform and equally spaced from 0 to 1 msec. This 30-vector was then used to train a linear discriminant algorithm. The data were generated with random values of surface roughness, h, ranging from 0 to 10 cm, and with random noise added to the waveforms to produce a realistic test.

The linear discriminant algorithm converged when the criteria was correct classification of mud versus gravel. The parameter vector P was essentially zero except for 200 μsec delay and 80 kHz and 160 kHz. The discriminant was approximately

$$X \cdot P = X(160 \text{ kHz}, 200 \mu\text{sec}) - 0.25X (80 \text{ kHz}, 200 \mu\text{sec}).$$

This agrees generally with the conclusions of Meng and Guan (1982).

When the criteria was correct, discrimination between fine sand and mud, however, the algorithm failed. This indicates that it is not possible to discriminate linearly between these two sediment cases for all possible combinations of bottom roughness in the presence of noise.

Such an adaptive algorithm can be "trained" using model-generated echoes in the same way speech recognition systems are "trained." The linear discriminant algorithm can be trained to distinguish mud from gravel, but has difficulty with mud versus fine sand. This suggests that a more complex algorithm will be needed to remotely recognize the full range of ocean bottom types.

Applications for bottom recognition using pattern recognition techniques on multiple frequency echoes are a fairly remote prospect. While advances in electronics have made possible personal computer add-in circuit boards that can discriminate the sounds of speech, applying pattern recognition techniques to the recognition of voice commands, applications of similar hardware to bottom-type discrimination involve much more than development an appropriate circuit board. In addition to the recognition hardware, transducers and electronics must be provided that can cover a suitable frequency range. In addition, existing survey boats would have to be adapted to these new transducers, and the present data analysis and charting system would have to

be modified to accept output from the recognition hardware. The magnitude of these changes and problems are such that it would be more appropriate to incorporate them at a future time when the present systems are being totally replaced.

Of more immediate benefit to NOS's charting needs would be an upgrade to the existing DSF-6000 echo-sounder. The method developed for aligning the digitized echoes for analysis (see EXPERIMENT EQUIPMENT section), could be programmed into a small module containing a digital signal processing (DSP) integrated circuit (IC). This module could then be wired into the DSF-6000 in place of the present detector circuit to provide improved performance. Externally, the acoustic and data interfaces of the DSF-6000 would remain the same, but performance would be upgraded.

Development of a replacement detector based on a DSP IC would be a suitable task for any of a number of small, independent electronic engineering and consulting firms. A number of suitable DSP ICs are available now from Texas Instruments (32010 etc.), AT&T (DSP32, DSP16), Motorola (56000) etc. The module would contain the DSP IC, a program memory, an analog to digital converter to convert the DSF-6000 signals to a form suitable for the DSP IC, output circuitry to signal the detection of the bottom echo, and other necessary circuitry such as clock generators.

This proverbial "handful of ICs" would implement the algorithm specified in the EXPERIMENT EQUIPMENT section of this report. The DSP IC would keep a constantly updated running sum estimate of the square integral or energy of the acoustic echo waveform received by the DSF-6000. This energy estimate then establishes a threshold so that when the integrated square voltage crosses the threshold, the DSP IC issues a bottom detected signal. Obvious refinements include establishing a time window for looking at the signal to minimize the processing required, and to reduce the possibility or spurious

triggering; this window would track the expected position of the bottom on a pulse to pulse basis.

The proposed replacement detector module for the DSF-6000 should be easy to develop within a relatively short time at moderate cost. It would nevertheless provide a definite near-term payoff in improved survey accuracy.

ACKNOWLEDGEMENTS

We would like to thank Dr. Stan Alpers of NOS for his encouragement and discussions.

The success of the project would not have been possible without the valuable contributions of Charles Lauter, Paul Dammann, Elizabeth Redmond, Jules Craynock, LTJG Mark Pickett, and Alexandra Lorenzo of OAD.

BIBLIOGRAPHY

Bachman, R. T., "Acoustic and physical property relationships in marine sediment," J. Acoust. Soc. Am., 78, 616-621 (1985).

Clarke, T. L., J. Proni, S. Alper, and L. Huff, "Definition of 'ocean bottom' and 'ocean bottom depth'," Proceedings, Oceans '85, 1212-1216 (1985).

Clarke, T. L., J. R. Proni, D. A. Seem, and J. J. Tsai, "Joint CGS-AOML acoustical bottom echo-formation research I: Literature search and initial modelling results," Tech. Memo. ERL AOML-66, 73 pp. (1988).

Clay, C. S., "Fluctuations of sound reflected from the sea surface," J. Acoust. Soc. Am., 32, 1547-1551 (1960).

Dammann, P., "A high resolution bottom profiler," NOAA Tech. Memo. (1988).

Dodds, D. J., "Surface and volume backscattering of broadband acoustic pulses normally incident on the seafloor: observations and models," J. Acoust. Soc. Am., 75, Suppl. 1, S29 (1984).

Jackson, D. R., D. P. Winebrenner, and A. Ishimaru, "Application of the composite roughness model to high-frequency bottom backscattering," J. Acoust. Soc. Am., 79, 1410-1422 (1986).

Meng, J., and D. Guan, "Acoustical method for classification of seafloor sediment," Chinese J. Acoust., 1, 48-53 (1982).

Stanic, S., K. B. Briggs, P. Fleischer, R. I. Roy, and W. B. Sawyer, "Shallow-water high-frequency bottom scattering off Panama City, Florida," J. Acoust. Soc. Am., 83, 2134-2144 (1988).

APPENDIX - GEOLOGY REPORT

FINAL GEOLOGY REPORT: BASEX PROJECT

INTRODUCTION AND METHODS

In support of the Ocean Acoustics Division's BASEX program, sediment samples were obtained and analyzed from sites in Chesapeake Bay and Duck Island. The site designators are as follows:

Chesapeake Bay Sites and Samples:

Little Creek Site	Core GC-1, box core
Bridge/Tunnel Site	Shipek grab sample
Thimble Shoal Channel Site	box core "grab sample", "anchor" sample
Middle Ground	Core GC-2, box core

Dodge Island Site and Samples:

Off The Wall Site	Cores GC-3, GC-4, box core

Our analysis methods are summarized as follows. Each gravity (GC) and box core was x-radiographed for detection of internal structures, before core opening. This helped identify internal structures, potentially not visible in the sediment upon visual inspection, and to guide sampling upon opening of the core. Immediately after core splitting, the sediment was photographed by 35mm photography and the sediment internal structures were recorded through visual inspection. Prints from the x-radiograph and 35mm color negatives are available upon request. Subsampling for the geotechnical properties of water content, and its later derivatives, bulk density and porosity, was done at 5 cm intervals from the top to the bottom of each core. Since box cores and grabs were not water tight samples, these geotechnical measurements could not be done on such samples in any meaningfull way. Bulk densities were derived from water content via standard geotechnical tables (Bennett et al., 1971) as were porosity values (Lambert and Bennett, 1972). Initial samples were sieved at all intervals but because of the labor intensive nature of sieving at 1/4-phi intervals and the project deadlines, detailed sand analyses were subsequently done at 10 cm intervals. All samples analyzed for sand/fine ratios (63 micron break point) were expressed as respective percentages of each, relative to the total sample. Carbonate content of the samples was done at the same intervals as the sand analysis by removal through acid leaching. The results are expressed as both carbonate percentage of total sediment and percentage of sand.

RESULTS

The results of our tests are submitted herein in two basic tabular forms, a Geotechnical/Texture Summary Table and a Sand Weight % Per 1/4-phi Interval Table with its attendant 1/4-phi interval histograms for each sample. Values entered into the Sand Weight % Table in the)2000 micron interval represents the weight of material, in grams, larger than this boundary but not included in the total weight to which the sand % were normalized. The above are all grouped by sampling site in this report.

For further guidance, a brief description of the results of the visual inspection of the core's x-radiographs and sediment is give below.

Little Creek Site: Core GC-1 (92 cm long)

* at 20.5 cm, granule-sized hard material
* 28-30 cm, sediment in hard lumps
* 35 cm sandy lenses
* 43-45 cm has sandy pockets with fiberous organic remains
* 6-7 mm thick shell hash layer centered at 47 cm
* 83-85 cm interval seems to have increased in sand % from above
* 87-89 cm seems sandy and very firm

Middle Ground Site: Core GC-2 (47 cm long)

* whole core very firm and very sandy
* 17-22.5 cm very sandy and very firm
* 32-34 cm sandy lenses in mud
* 39 cm is interface for mud pocketed with sand above, and sand below

Thimble Shoal Channel Site: Box core "crab sample"

* 432.16 grams of solids recovered
* 107.65 grams (24.9%) of above sampled shell material)2000 microns
* 324.51 grams (75.1%) of above sampled sand material (ie (2000 microns)

Middle Ground: Box core

* sample very rich in fiberous organic material and large shell hash and whole shells.
* from a 330.14 grams subsample 3.3 grams was roots and grass and 8.91 grams was a large shell

Off The Wall Site: Core GC-3 (22 cm long)

* 9-14 cm shell and other crab muddy hash layer(s)
* matrix mud carbonate rich

Off The Wall Site: Core GC-4 (37 cm long)

* 5-7 cm highly variable texture
* nearly horizontal sandy zones at 8.5, 11, 17.5 & 32-37 cm
* some fine shell hash present in each of above, especially 32-37 cm
* 33-35 cm very sandy with charred organic matter

CLOSING COMMENTS

Lack of homogeneity at given sites, such as at Thimble Shoal Channel, is evidenced by the box core "grab sample" and the anchor sample where two drastically different samples were obtained from the "same" spot. This must be kept in mind when and if geology and acoustics seem at odds.

REFERENCES

Bennett, R.H., Lambert, D.N., and Grim, P.J., 1971, Tables for Determining Unit Weight of Deep-Sea Sediments from Water Contents and Average Grain Density Measurements, NOAA Tech Memo ERL AOML-13, 56 pp.

Lambert, D.N., and Bennett, R.H., 1972, Tables for Determining Porosity of Deep-Sea Sediments from Water Content and Average Grain Density Measurements, NOAA Tech Memo ERL AOML-17, 50 pp.

AOML OCD

GEO NICAL / TEXTURE SUMMARY TABLE

PROJECT: BASE X CORE/SAMPLE: GC 1

Little Creek Site, Chesapeake Bay

DEPTH (cm)	WATER (%)	BULK DENSITY (g/cc)	POROSITY (%)	SAND (%)	FINE (%)	CARBONATE % TOTAL	CARBONATE % SAND
0-2	166.49	1.310	81.78	16.80	83.20	0.00	0.00
5-7	142.10	1.352	79.34				
10-12	130.49	1.377	77.8	32.98	67.02	0.74	2.23
15-17	141.65	1.352	79.34				
22-24	126.87	1.384	77.38	22.16	77.84	0.36	1.63
28-30	124.92	1.389	77.1				
33-35	98.13	1.466	72.6	39.40	60.60	0.57	1.45
38-40	136.91	1.362	78.7				
43-45	107.86	1.434	74.4	35.49	64.51	0.83	2.35
48-50	92.24	1.488	71.5				
53-55	126.12	1.386	77.2	28.09	71.91	0.48	1.70
58-60	116.98	1.409	75.9				
63-65	135.77	1.364	78.6	20.03	79.97	0.30	1.49
68-70	121.95	1.396	76.7				
73-75	81.3	1.533	68.6	32.09	67.91	0.62	1.95
78-80	90.65	1.492	71.1				
83-85	64.02	1.623	63.3	40.50	59.50	0.27	0.67
87-89	50.79	1.715	57.9				

PROJECT: BASEY CORE/SAMPLE: GC-1

Little Creek Site

PHI CLASS	MICRON SIZE	WEIGHT % PER 1/4 PHI CLASS				
		INTERVAL	INTERVAL	INTERVAL	INTERVAL	INTERVAL
		0-2	10-12	22-24	33-35	43-45
-1.0	2000	0.01	0.0	0.02	0.02	0.10
-0.75	1690	2.40	0.17	0.00	0.00	0.00
-0.50	1410	2.85	0.34	0.20	0.41	0.52
-0.25	1190	3.366	0.69	0.81	0.41	1.15
0.00	1000	2.88	0.69	1.21	0.52	1.78
0.25	840	2.85	0.69	1.21	0.52	1.46
0.50	710	4.33	0.86	2.02	0.72	2.52
0.75	590	4.33	1.20	3.84	1.34	4.30
1.00	500	3.85	1.20	4.24	1.55	4.72
1.25	420	3.85	2.24	6.67	2.79	8.18
1.50	351	3.37	2.58	6.06	3.30	6.92
1.75	297	4.33	3.79	7.27	5.26	7.34
2.00	250	3.85	2.75	6.06	5.78	4.93
2.25	210	5.77	4.82	8.08	8.77	7.02
2.50	177	4.33	4.65	6.06	6.91	5.24
2.75	149	6.73	10.15	8.28	10.73	8.49
3.00	125	6.25	11.19	6.26	8.15	7.02
3.25	105	8.17	15.32	8.48	8.77	7.97
3.50	88	9.62	15.49	8.23	12.18	7.86
3.75	74	12.50	14.52	11.51	16.20	10.27
4.00	63	4.33	4.65	3.43	5.67	2.30

PROJECT: BASE X CORE/SAMPLE: GC1

Little Creek Site

PHI CLASS	MICRON SIZE	WEIGHT % PER 1/4 PHI CLASS				
		INTERVAL 53-55	INTERVAL 63-65	INTERVAL 73-75	INTERVAL 83-85	INTERVAL
-1.0	2000	/	/	/	/	
-0.75	1690	0.00	1.31	0.10	0.67	
-0.50	1410	0.52	0.78	0.40	0.00	
-0.25	1190	0.52	0.78	0.80	0.27	
0.00	1000	0.52	0.52	1.39	0.27	
0.25	840	0.86	1.57	1.69	0.53	
0.50	710	1.20	2.61	3.09	0.47	
0.75	590	2.34	3.13	5.28	0.60	
1.00	500	3.61	2.61	6.97	0.80	
1.25	420	6.54	4.56	13.65	1.40	
1.50	351	6.02	3.92	10.56	1.53	
1.75	297	6.37	4.44	10.76	2.40	
2.00	250	5.68	3.66	6.47	2.73	
2.25	210	8.61	5.48	6.27	4.66	
2.50	177	6.88	5.22	3.69	4.46	
2.75	149	9.29	9.40	5.08	9.32	
3.00	125	7.57	7.31	3.98	9.99	
3.25	105	9.12	10.97	5.48	14.85	
3.50	88	9.29	10.97	5.38	18.04	
3.75	74	12.05	15.14	7.57	22.17	
4.00	63	3.10	5.22	1.39	5.46	

Base X.

GC1 #185

0-2cm

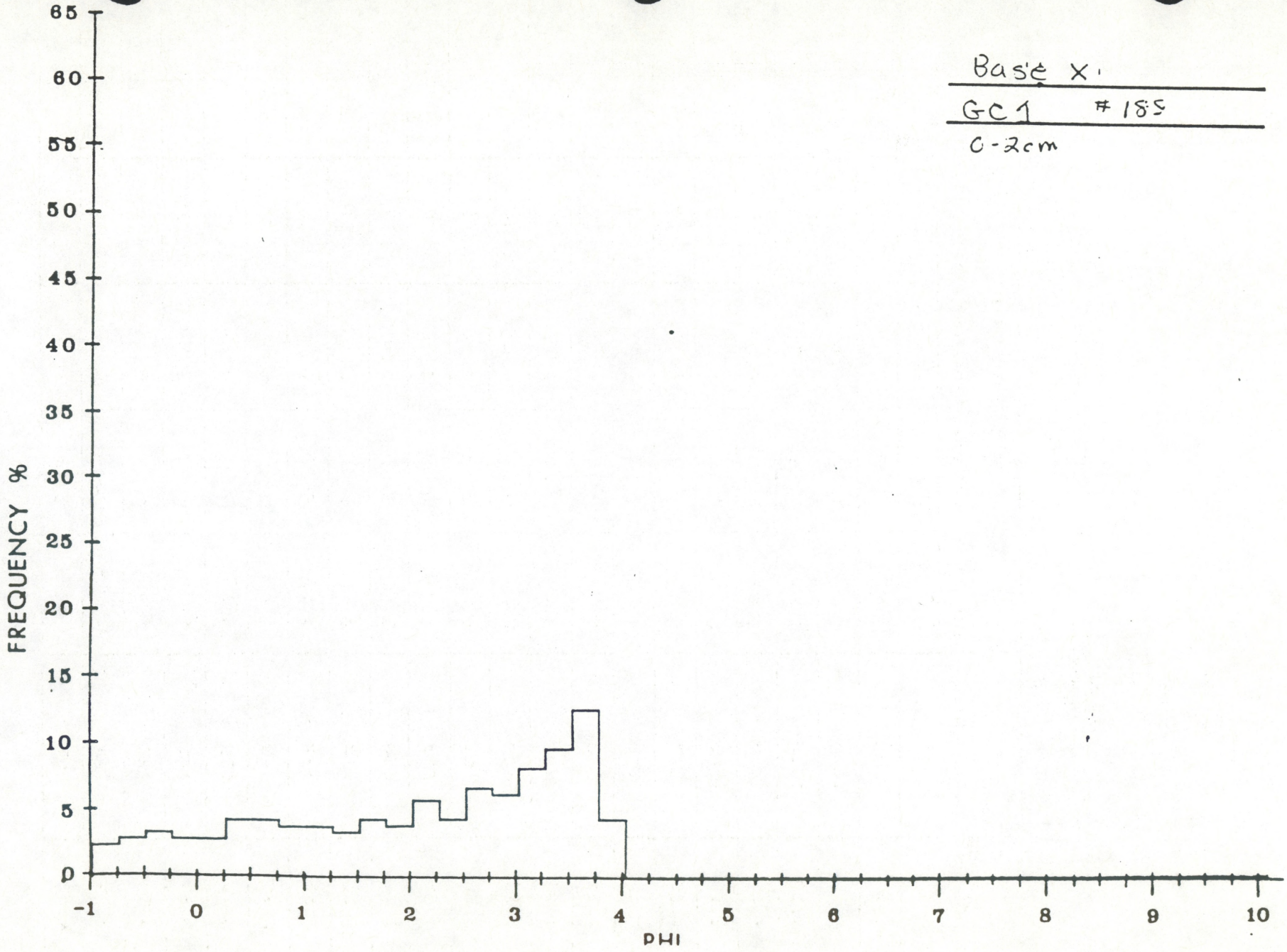

Base X · Little Oak Site

GC 1 # 151

10 - 12 cm

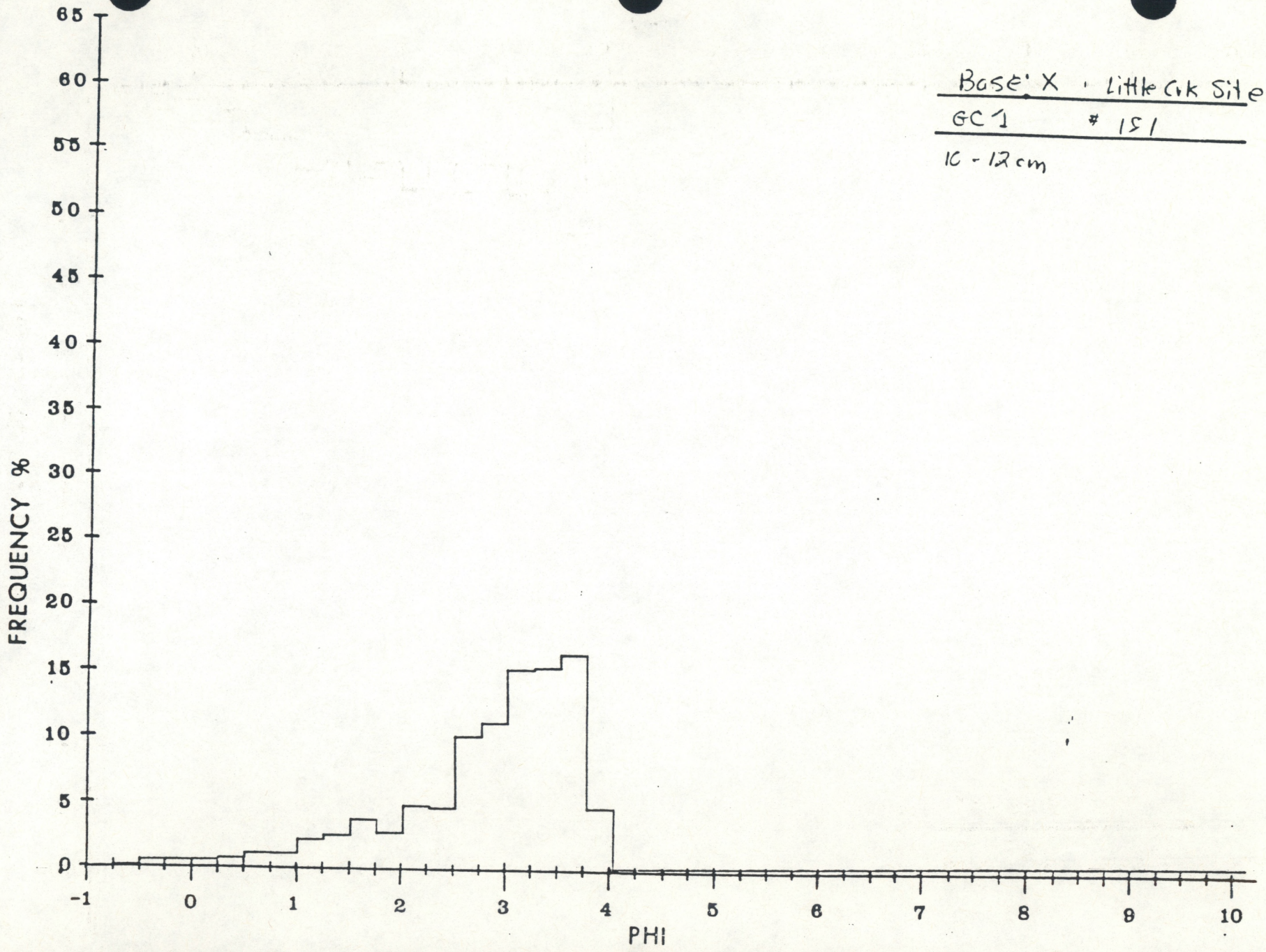

Basex
GC '1 Little Crk Site
193
22 - 24 cm

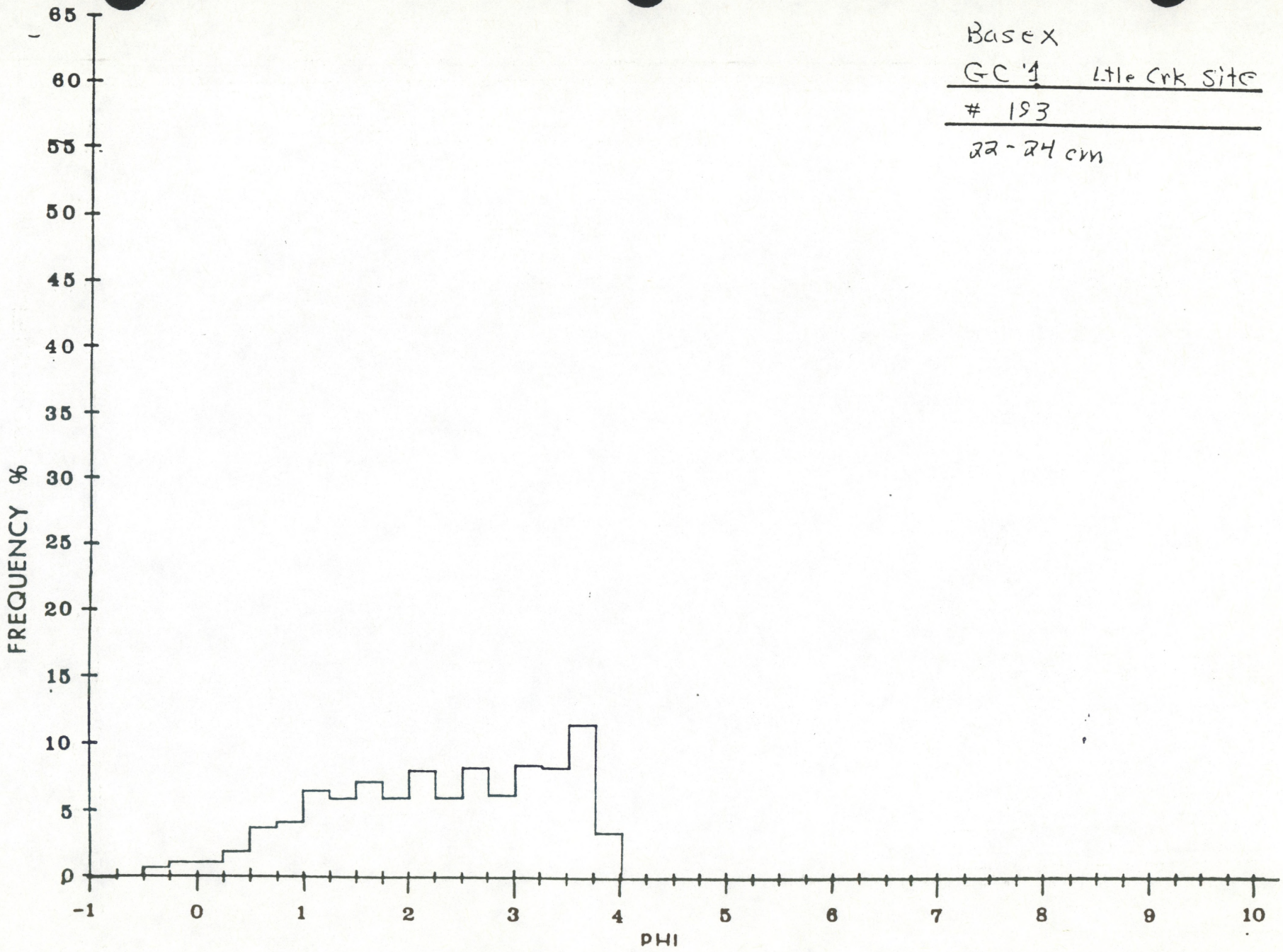

Base X

GC 1 # 155

33-35cm

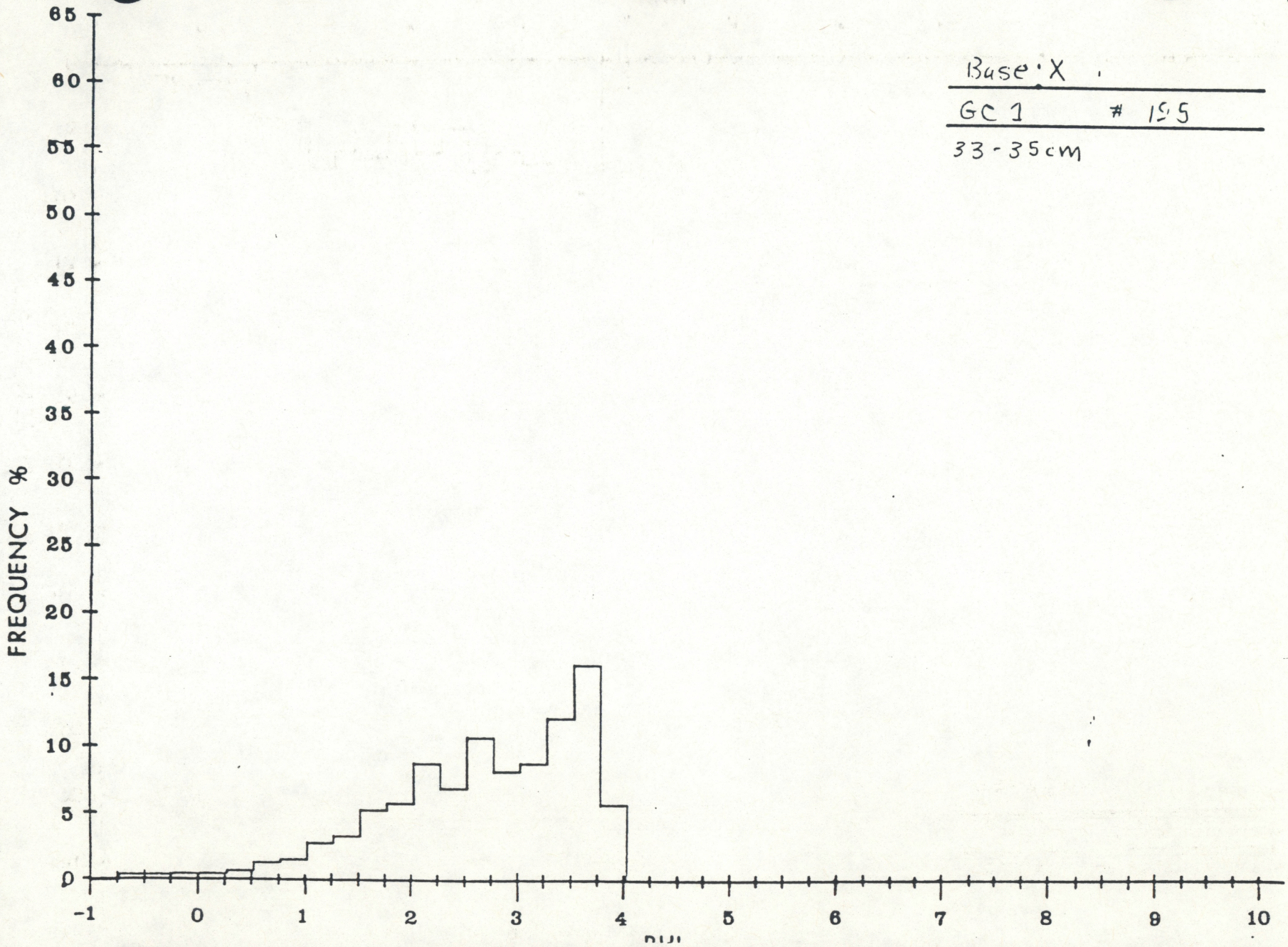

Base X.

GC 1 *197

43-45 cm

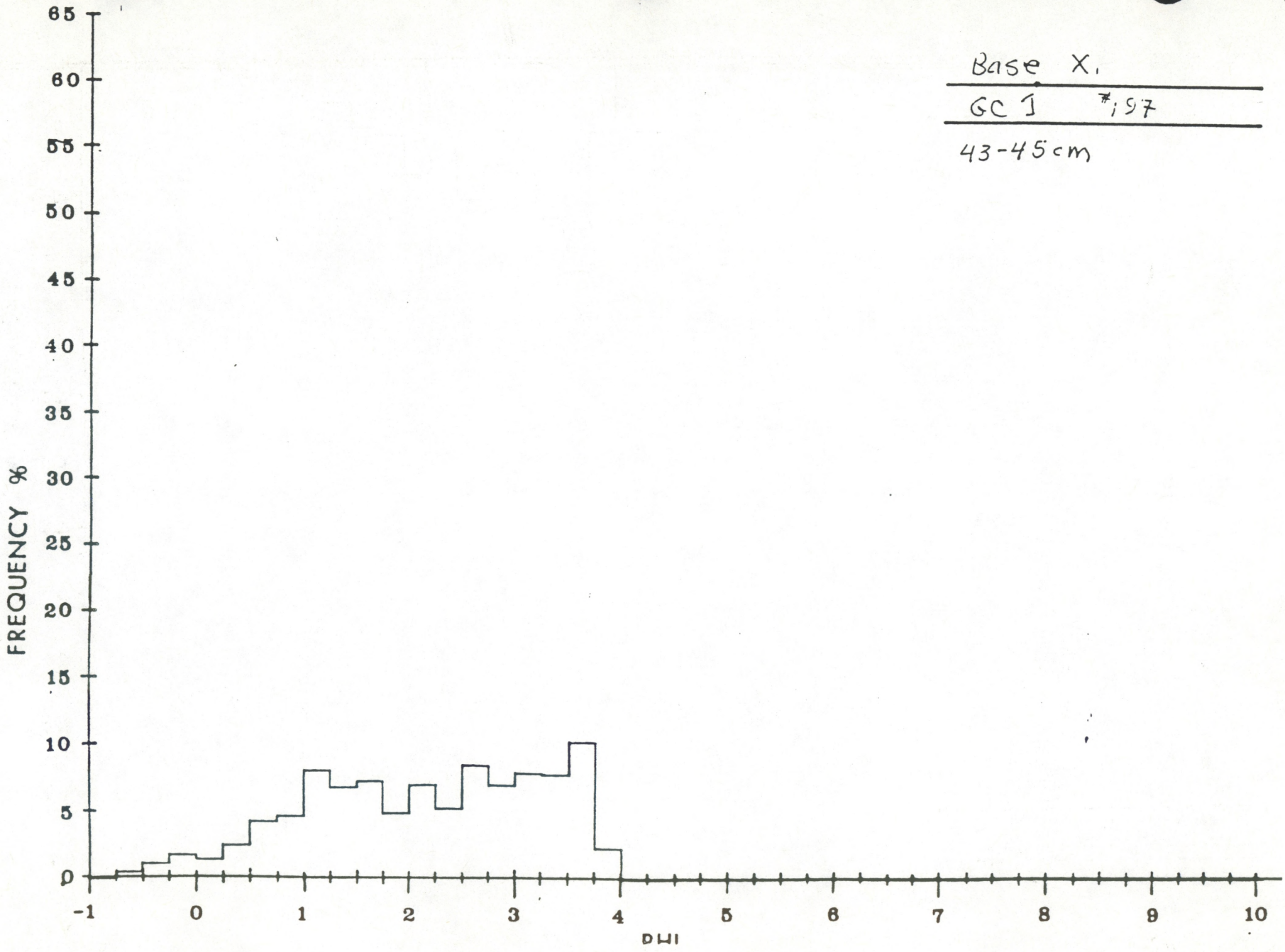

Base 'X'	Little Creek Site
GC 1	53 - 55 cm
#199	

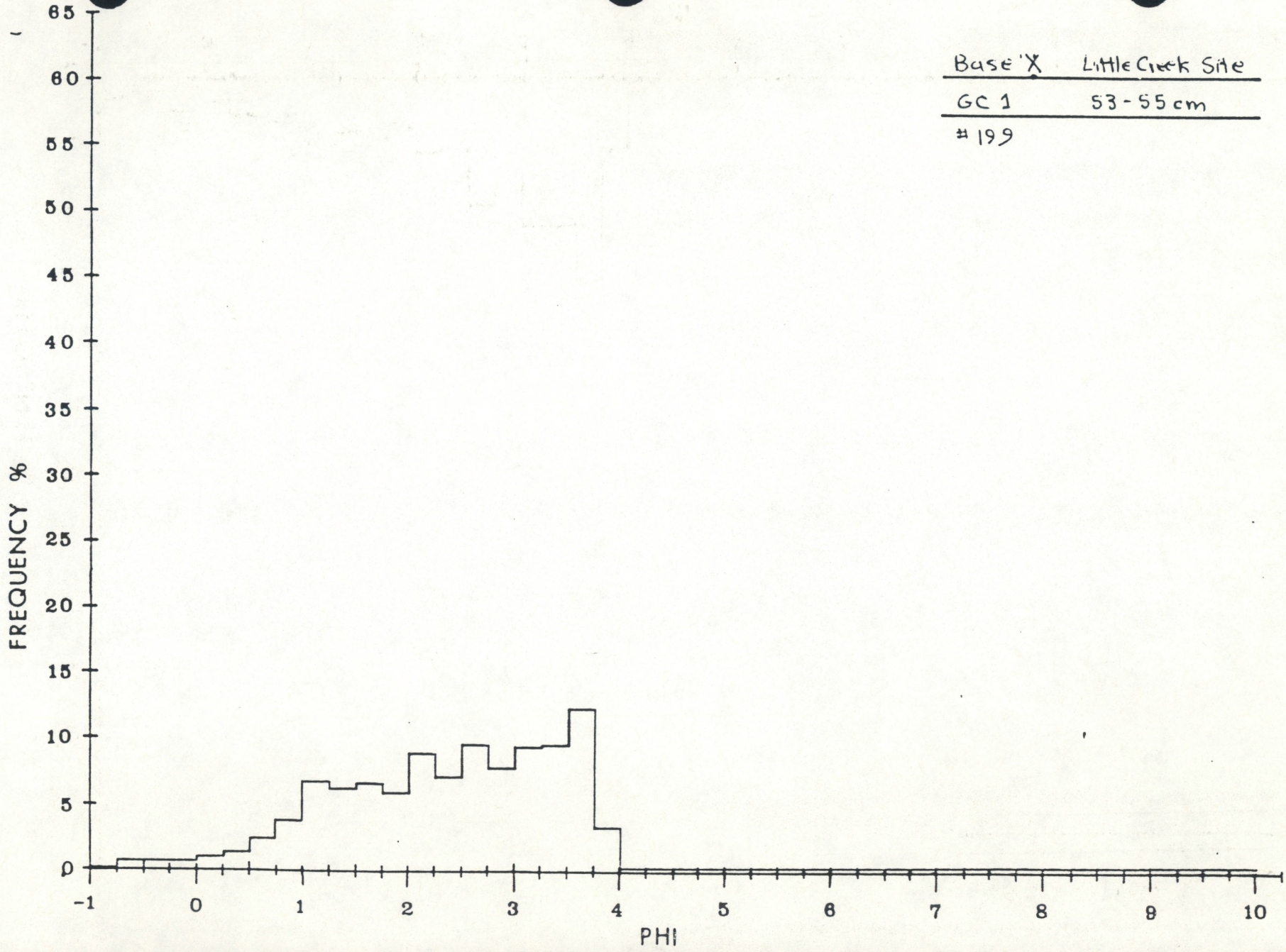

Base X . GC1
#231 63-65cm

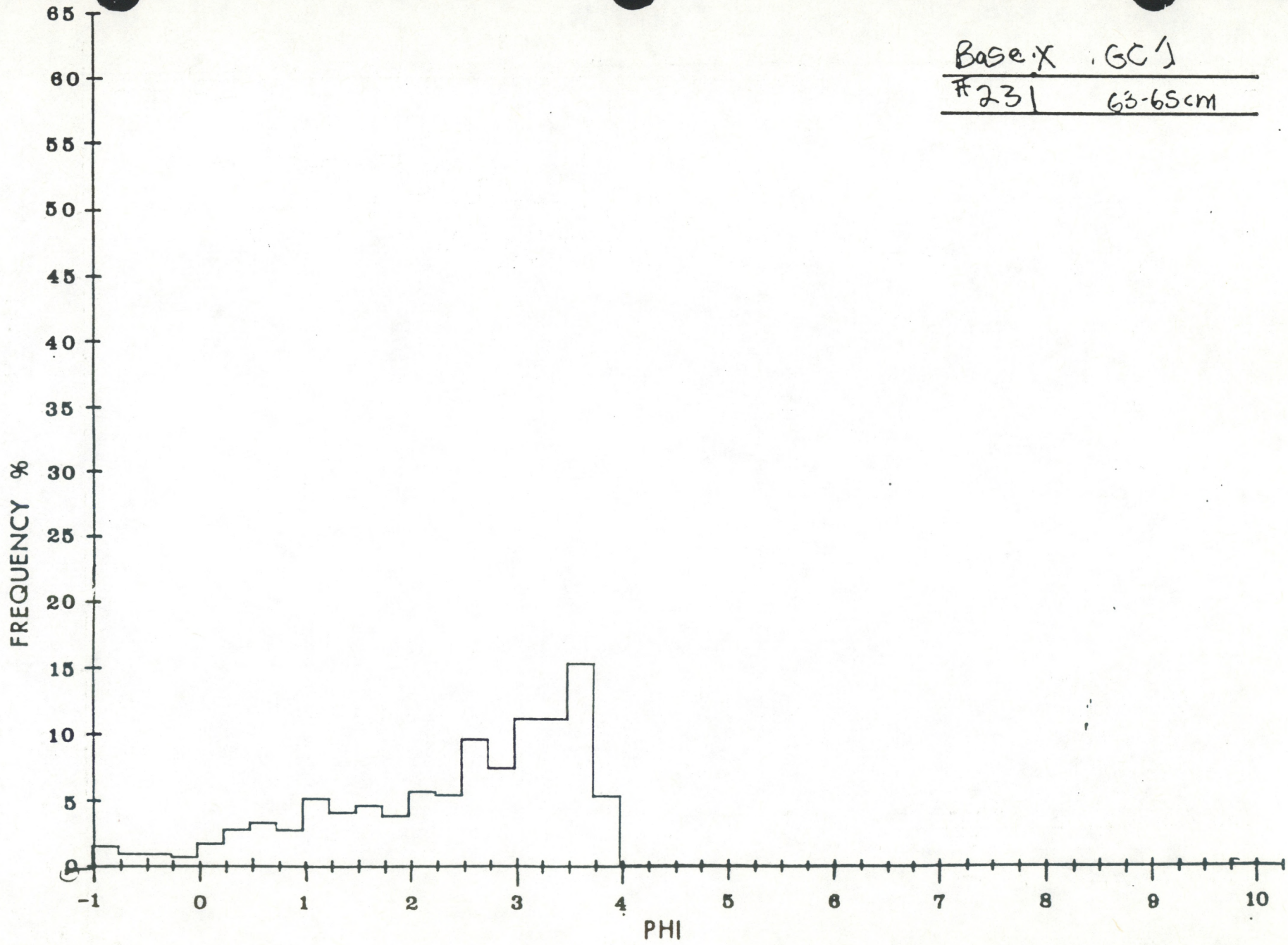

Base X · Little Crk Site

GC 1 # 233

73-75cm

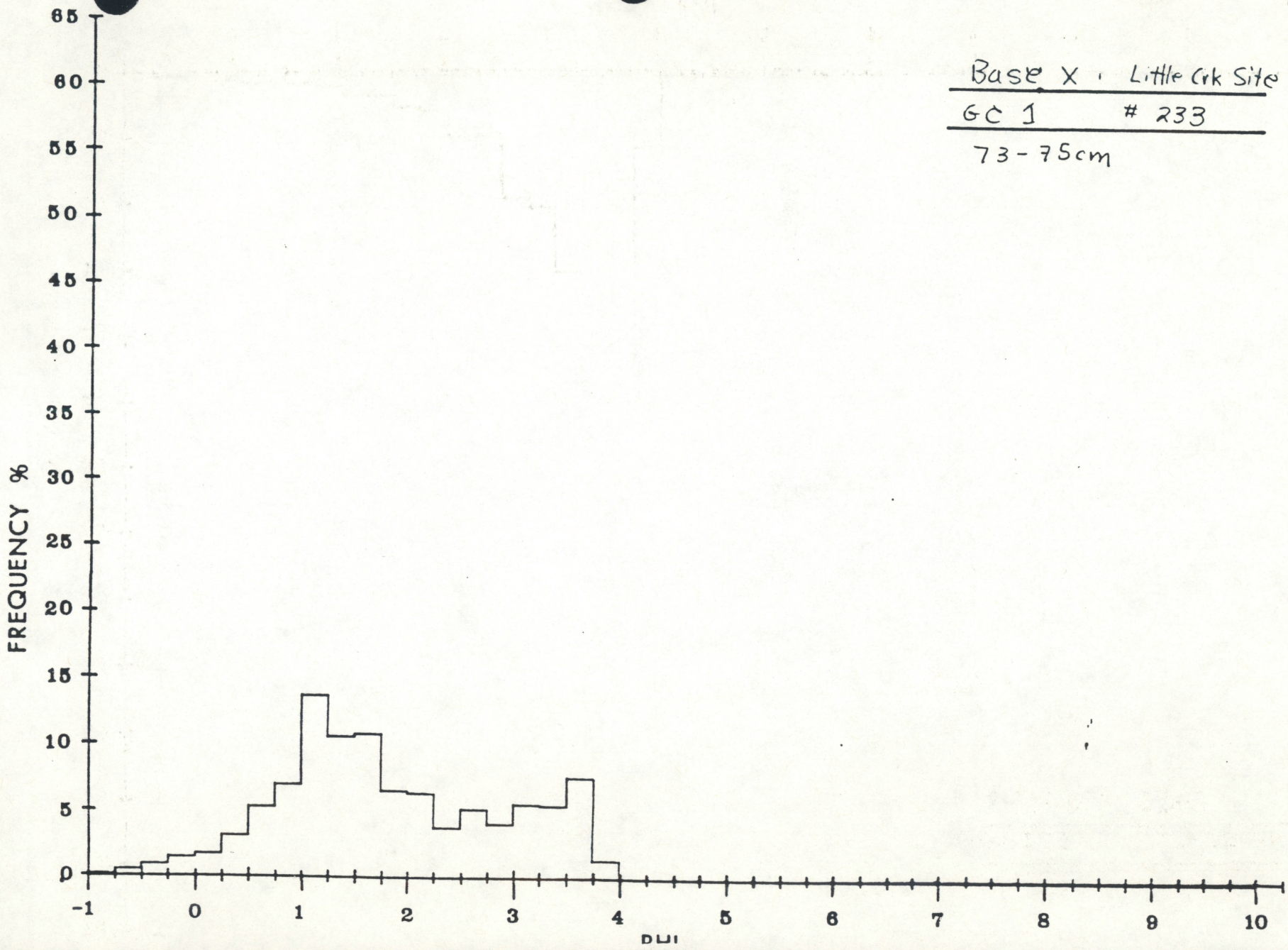

BASE X : GC 1

235 83-85cm

Little Crk Site.

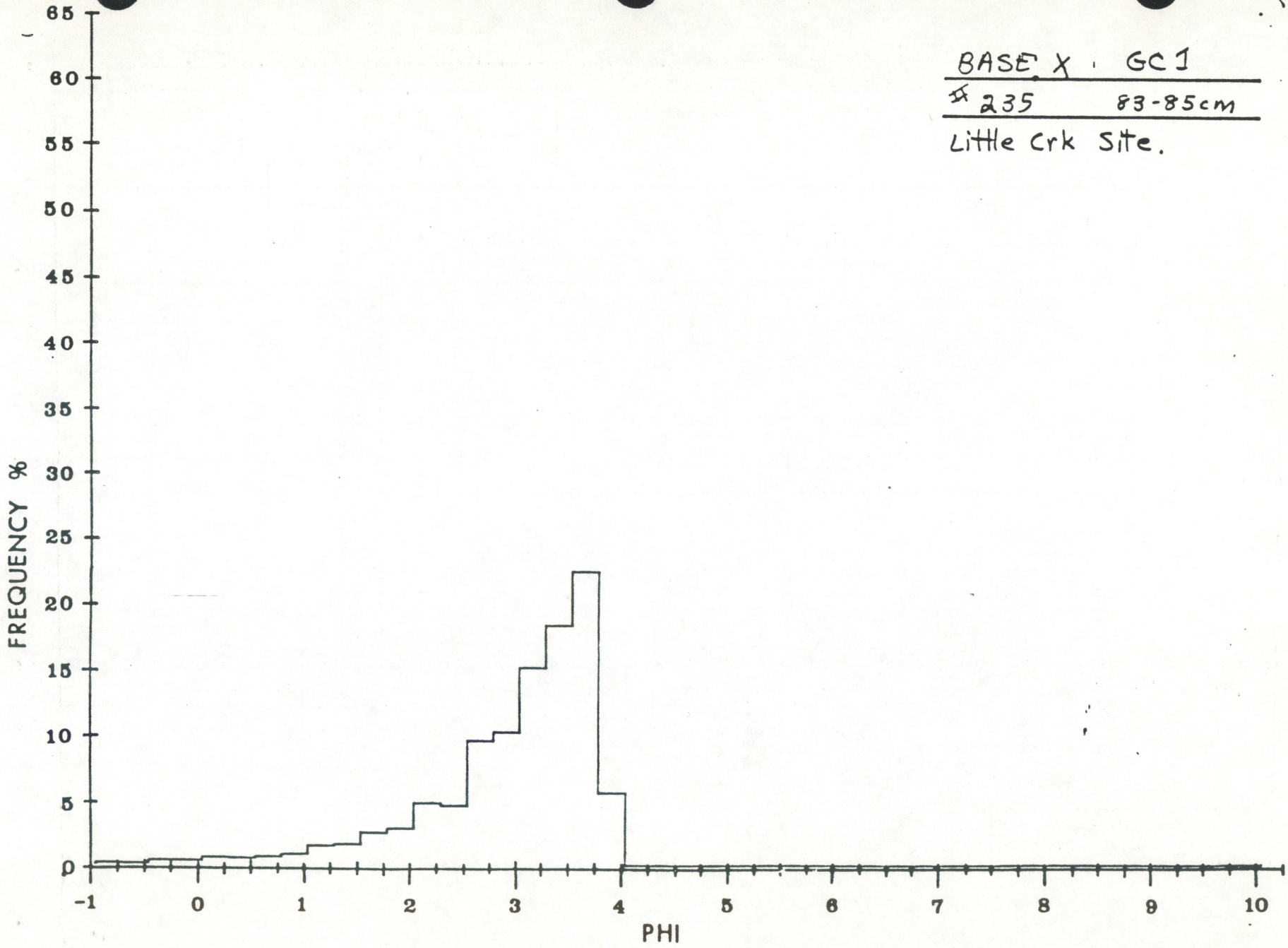

AOML OCD

GEOTECHNICAL / TEXTURE SUMMARY TABLE

PROJECT: BASE X
Bridge/Tunnel Site

CORE/SAMPLE: ShipEK Sample 1
Station 2

DEPTH (cm)	WATER (%)	BULK DENSITY (g/cc)	POROSITY (%)	SAND (%)	FINE (%)	CARBONATE %	
						TOTAL	SAND
N/A	N/A	—	—	95.86	4.14	0.74	0.77

SAND SIZE SUMMARY TABLE

PROJECT: BASE X
Bridge / Tunnel Site

CORE/SAMPLE: Shipek Sample 1
Sta: 2

PHI CLASS	MICRON SIZE	WEIGHT % PER 1/4 PHI CLASS INTERVAL	INTERVAL	INTERVAL	INTERVAL	INTERVAL
		N/A				
-1.0	2000	0.13				
-0.75	1690	0.06				
-0.50	1410	0.06				
-0.25	1190	0.08				
0.00	1000	0.10				
0.25	840	0.06				
0.50	710	0.06				
0.75	590	0.06				
1.00	500	0.08				
1.25	420	0.04				
1.50	351	0.04				
1.75	297	0.14				
2.00	250	0.47				
2.25	210	2.57				
2.50	177	7.62				
2.75	149	29.87				
3.00	125	13.65				
3.25	105	22.29				
3.50	88	15.43				
3.75	74	6.01				
4.00	63	1.29				

PARTICLE SIZE HISTOGRAM

Base X.

Shipek Sample 1

Station 2

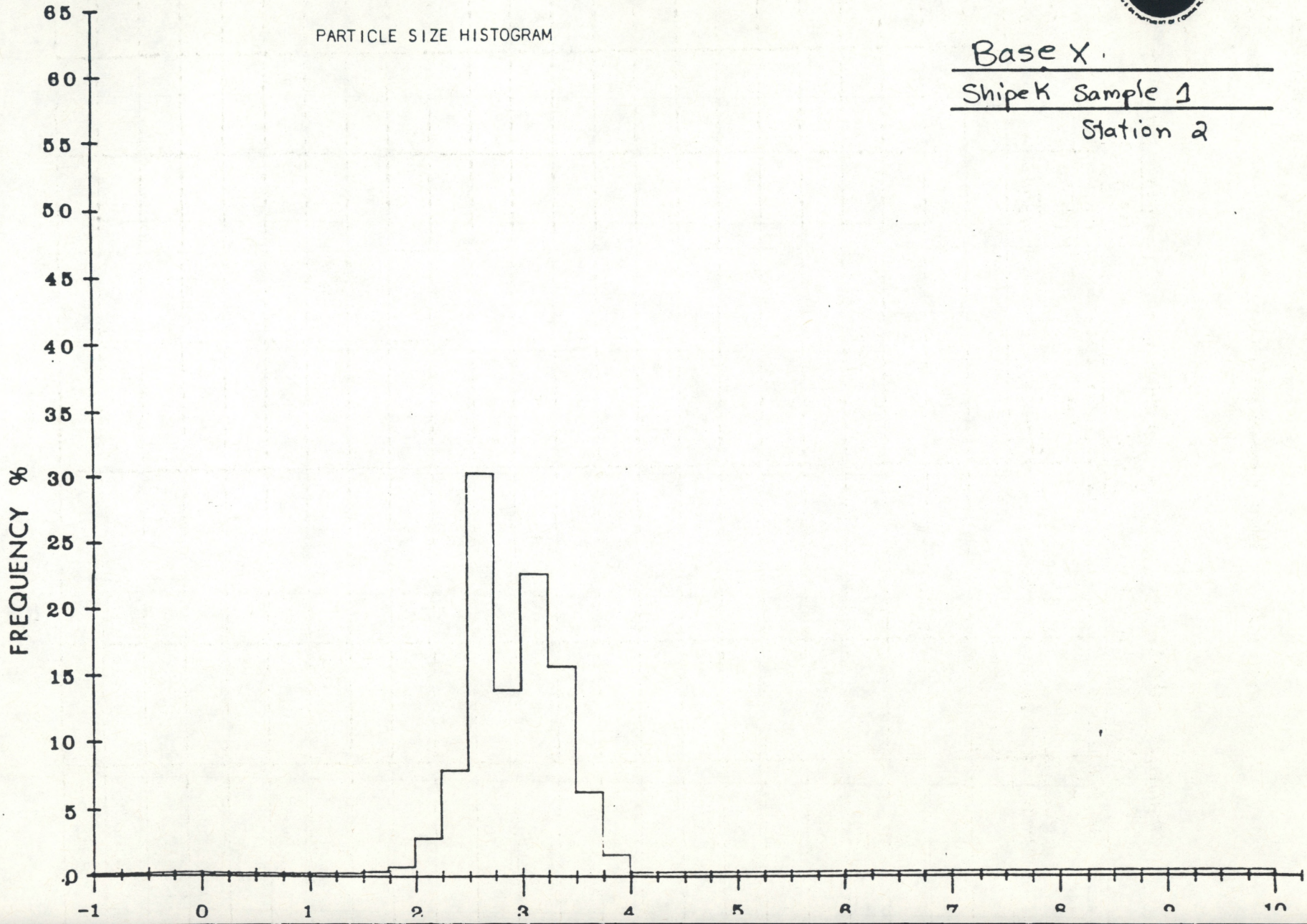

AOML OCD

GEOTECHNICAL / TEXTURE SUMMARY TABLE

PROJECT: BASE X CORE/SAMPLE: Anchor Sample

Thimble Shoals Channel Site Station 3

DEPTH (cm)	WATER (%)	BULK DENSITY (g/cc)	POROSITY (%)	SAND (%)	FINE (%)	CARBONATE %	
						TOTAL	SAND
N/A	N/A			51.50	48.50	1.11	2.16

SAND SIZE SUMMARY TABLE

PROJECT: BASE X CORE/SAMPLE: Anchor Sample

Thimble Shoals Channel Site Station 3

PHI CLASS	MICRON SIZE	WEIGHT % PER 1/4 PHI CLASS				
		INTERVAL	INTERVAL	INTERVAL	INTERVAL	INTERVAL
		N/A				
-1.0	2000	C.13				
-0.75	1690	C.10				
-0.50	1410	0.13				
-0.25	1190	C.15				
0.00	1000	C.18				
0.25	840	0.18				
0.50	710	C.21				
0.75	590	C.31				
1.00	500	C.33				
1.25	420	C.44				
1.50	351	C.49				
1.75	297	C.66				
2.00	250	0.54				
2.25	210	0.62				
2.50	177	C.76				
2.75	149	3.91				
3.00	125	6.25				
3.25	105	17.32				
3.50	88	29.58				
3.75	74	28.66				
4.00	63	9.18				

PARTICLE SIZE HISTOGRAM

BASE X

Anchor Sample Sta 3

272

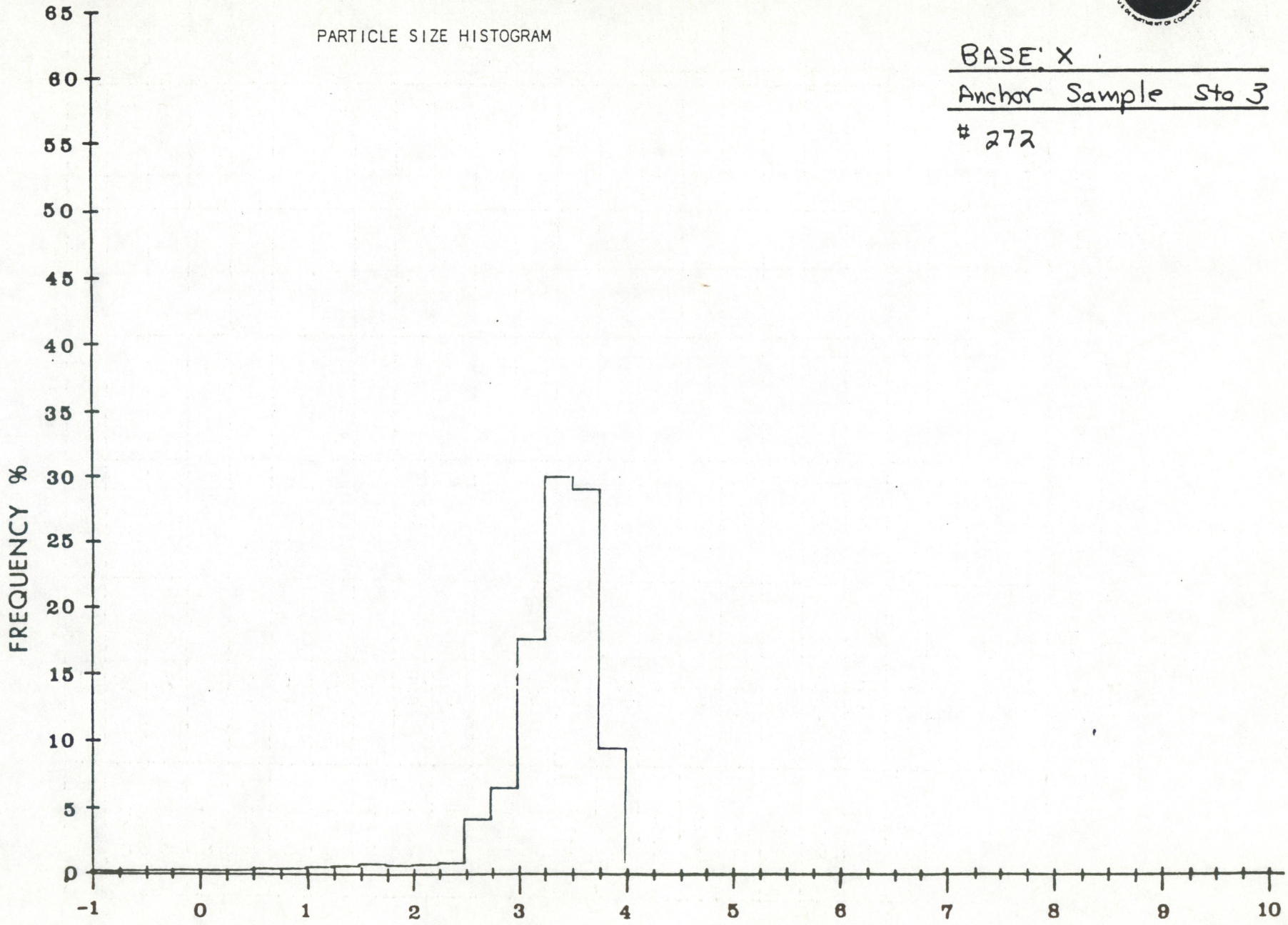

AOML OCD

GEOTECHNICAL / TEXTURE SUMMARY TABLE

PROJECT: BASE X CORE/SAMPLE: Box Station 3

@ Thimble Shoals Channel Site

DEPTH (cm)	WATER (%)	BULK DENSITY (g/cc)	POROSITY (%)	SAND (%)	FINE (%)	CARBONATE %	
						TOTAL	SAND
N/A	N/A			98.25	1.75	1.30	1.33

SAND SIZE SUMMARY TABLE

PROJECT: BASE X CORE/SAMPLE: Box Core

Thimble Shoals Channel Site Station 3

PHI CLASS	MICRON SIZE	WEIGHT % PER 1/4 PHI CLASS INTERVAL	INTERVAL	INTERVAL	INTERVAL	INTERVAL
		N/A				
-1.0	2000	0.02				
-0.75	1690	[illegible]				
-0.50	1410	3.86				
-0.25	1190	4.[illegible]				
0.00	1000	[illegible].78				
0.25	840	7.21				
0.50	710	7.6[illegible]				
0.75	590	9.04				
1.00	500	10.14				
1.25	420	13.57				
1.50	351	10.[illegible]9				
1.75	297	10.74				
2.00	250	[illegible].56				
2.25	210	3.53				
2.50	177	1.[illegible]3				
2.75	149	[illegible].15				
3.00	125	0.45				
3.25	105	0.45				
3.50	88	0.30				
3.75	74	0.20				
4.00	63	0.10				

PARTICLE SIZE HISTOGRAM

Base X

Box Core Sta 3

Pan # 271

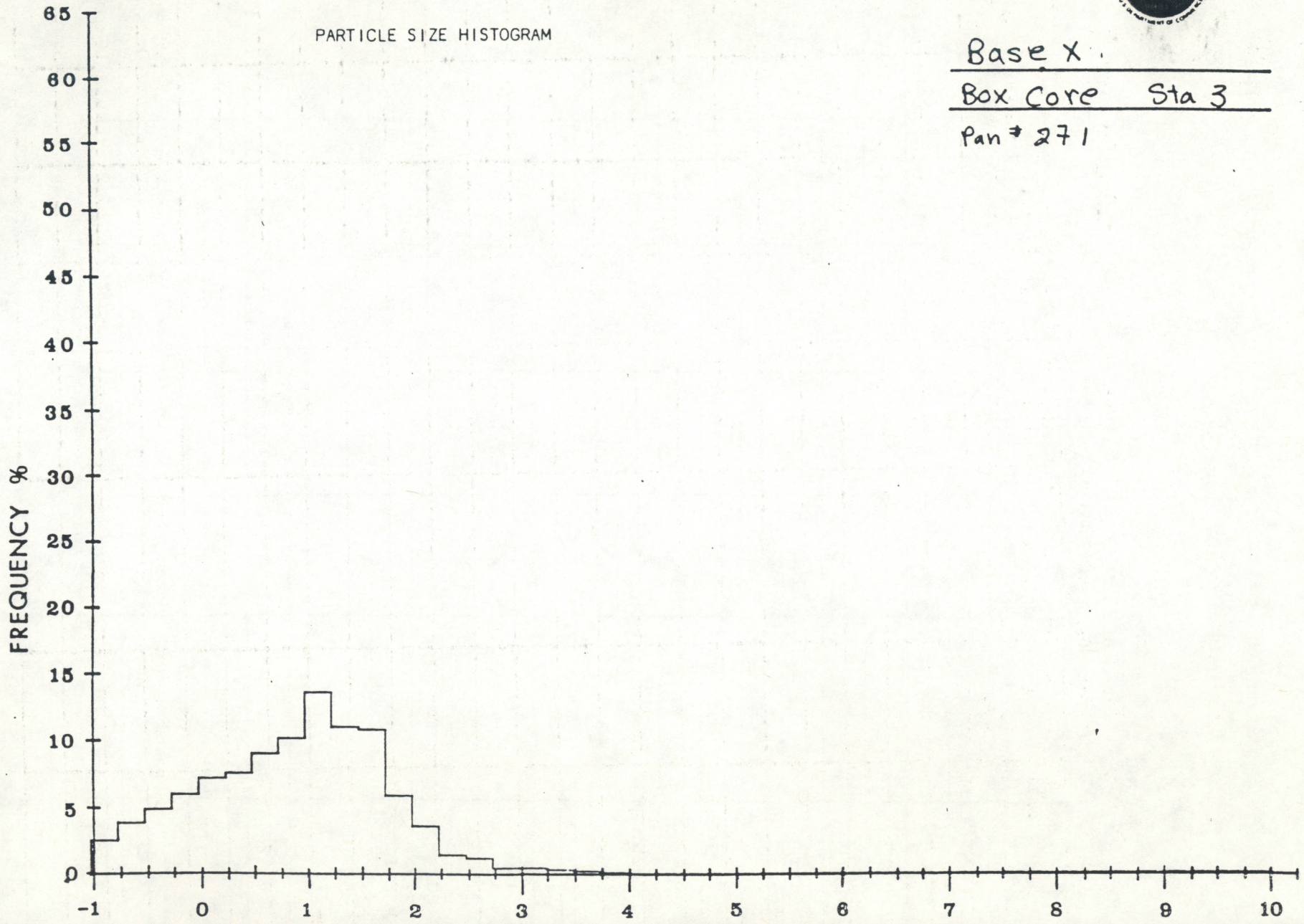

AOML OCD

GEOTECHNICAL / TEXTURE SUMMARY TABLE

PROJECT: BASE X
Middle Ground Site

CORE/SAMPLE: Box 1 Station 4

DEPTH (cm)	WATER (%)	BULK DENSITY (g/cc)	POROSITY (%)	SAND (%)	FINE (%)	CARBONATE %	
						TOTAL	SAND
N/A	N/A			98.91	1.09	2.36	2.39

PROJECT: BASE X CORE/SAMPLE: Box 1 Station 4

Middle Ground Site

PHI CLASS	MICRON SIZE	WEIGHT % PER 1/4 PHI CLASS INTERVAL	INTERVAL	INTERVAL	INTERVAL	INTERVAL
		N/A				
-1.0	2000	0.39				
-0.75	1690	[illegible]				
-0.50	1410	0.58				
-0.25	1190	0.51				
0.00	1000	0.38				
0.25	840	0.38				
0.50	710	0.25				
0.75	590	40				
1.00	500	0.61				
1.25	420	0.41				
1.50	351	0.43				
1.75	297	0.80				
2.00	250	0.65				
2.25	210	1.05				
2.50	177	2.53				
2.75	149	13.52				
3.00	125	17.06				
3.25	105	24.11				
3.50	88	20.02				
3.75	74	13.48				
4.00	63	2.71				

PARTICLE SIZE HISTOGRAM

BASE X
Box 1 Station 4
270

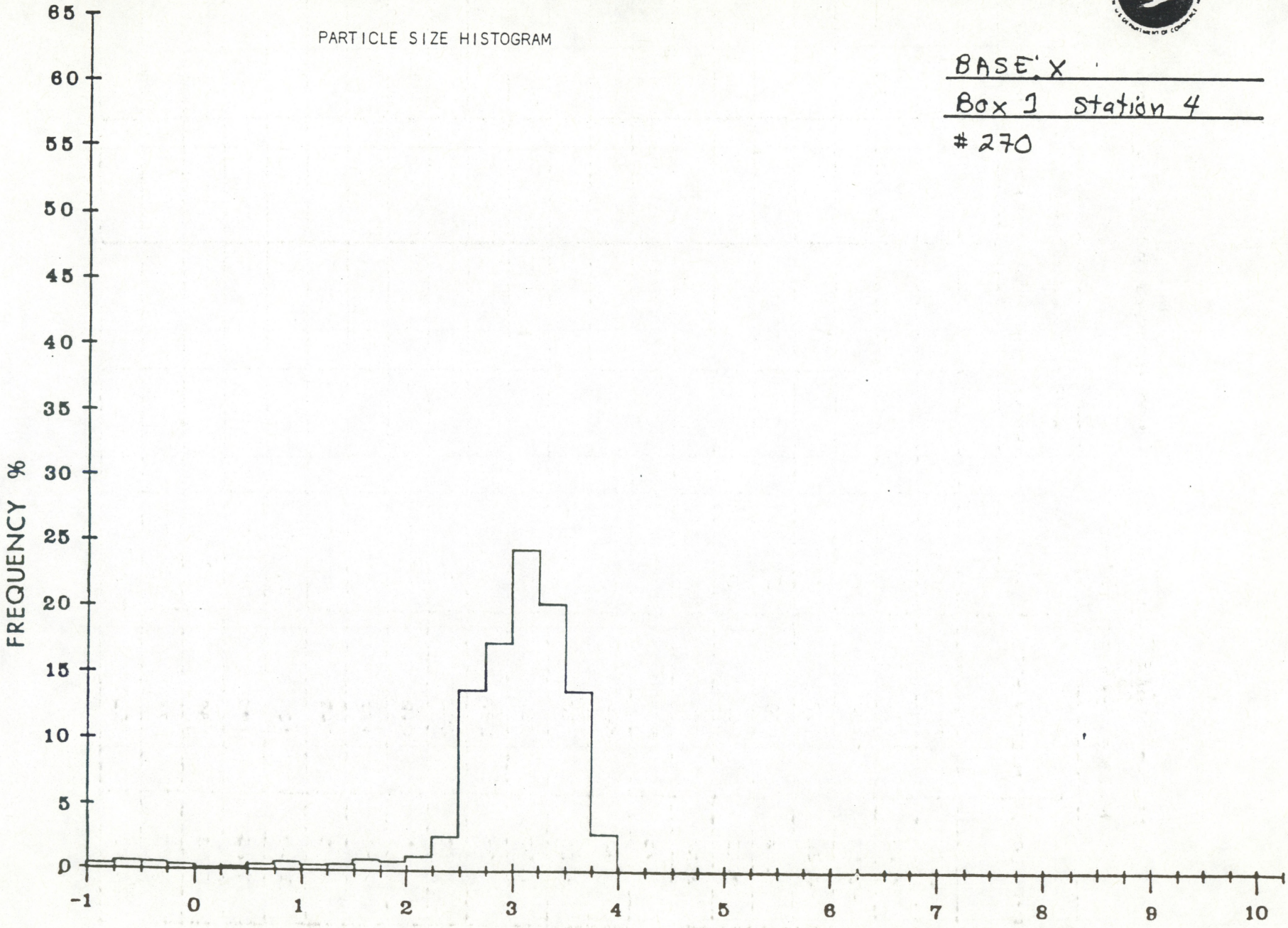

AOML OCD

GEO[illegible]NICAL / TEXTURE SUMMARY TABLE

PROJECT: BASE X CORE/SAMPLE: GC 2

Middle Ground Site. Chesapeake Bay

DEPTH (cm)	WATER (%)	BULK DENSITY (g/cc)	POROSITY (%)	SAND (%)	FINE (%)	CARBONATE %	
						TOTAL	SAND
0-2	28.91	1.953	43.9	89.54	10.46	1.94	2.17
6-8	34.05	1.886	47.9	67.38	32.62	0.93	1.37
12-14	44.06	1.777	54.3	72.90	27.10	0.57	0.78
17-19	30.64	1.925	45.6	75.09	24.91	1.42	1.89
22-24	31.38	1.925	45.6	79.23	20.77	7.47	5.43
27-29	34.62	1.874	48.6	67.88	32.12	0.65	0.95
32-34	42.12	1.797	53.1				
37-39	32.59	1.899	47.1	69.44	30.56	0.46	0.67
42-44	30.88	1.925	45.6				

PROJECT: Base X CORE/SAMPLE: GC 2

Chesapeake Bay

PHI CLASS	MICRON SIZE	WEIGHT % PER 1/4 PHI CLASS INTERVAL 0-2cm	INTERVAL 6-8	INTERVAL 12-14	INTERVAL 17-19	INTERVAL 22-24
-1.0	2000	0.07	0.05	/	/	/
-0.75	1690	0.05	0.08	0.00	0.00	0.00
-0.50	1410	0.10	0.04	0.72	0.00	0.00
-0.25	1190	0.29	0.02	0.11	0.00	0.00
0.00	1000	0.38	0.00	0.11	0.01	0.00
0.25	840	0.05	0.04	0.04	0.00	0.00
0.50	710	0.07	0.04	0.14	0.01	0.00
0.75	590	0.31	0.08	0.22	0.03	0.03
1.00	500	0.55	0.11	0.33	0.06	0.05
1.25	420	0.34	0.08	0.51	0.06	0.06
1.50	351	0.55	0.11	0.58	0.11	0.15
1.75	297	0.86	0.15	0.87	0.34	0.35
2.00	250	0.74	0.23	0.83	0.34	0.41
2.25	210	1.25	0.34	1.16	0.71	0.61
2.50	177	2.40	0.84	1.59	1.11	1.02
2.75	149	15.78	5.82	10.18	6.61	5.64
3.00	125	16.29	10.89	12.23	9.62	9.83
3.25	105	25.19	22.38	22.52	25.06	26.99
3.50	88	19.38	26.72	25.44	28.21	27.78
3.75	74	12.07	24.59	18.66	20.63	20.82
4.00	63	3.36	7.42	4.44	7.09	6.23

PROJECT: Base X

CORE/SAMPLE: GC 2
Chesapeake Bay

PHI CLASS	MICRON SIZE	WEIGHT x PER 1/4 PHI CLASS				
		INTERVAL	INTERVAL	INTERVAL	INTERVAL	INTERVAL
		27-29	37-39			
-1.0	2000	—	—			
-0.75	1690	0.00	0.00			
-0.50	1410	0.00	0.00			
-0.25	1190	0.00	0.00			
0.00	1000	0.00	0.00			
0.25	840	0.00	0.03			
0.50	710	0.00	0.03			
0.75	590	0.00	0.03			
1.00	500	0.03	0.03			
1.25	420	0.03	0.03			
1.50	351	0.03	0.03			
1.75	297	0.06	0.10			
2.00	250	0.06	0.14			
2.25	210	0.16	0.31			
2.50	177	0.67	1.41			
2.75	149	5.40	8.48			
3.00	125	10.62	14.07			
3.25	105	21.62	25.09			
3.50	88	28.33	27.08			
3.75	74	25.96	17.88			
4.00	63	7.00	5.25			

BASEY Chesapeake Bay
GC-2 0-2 cm
#237

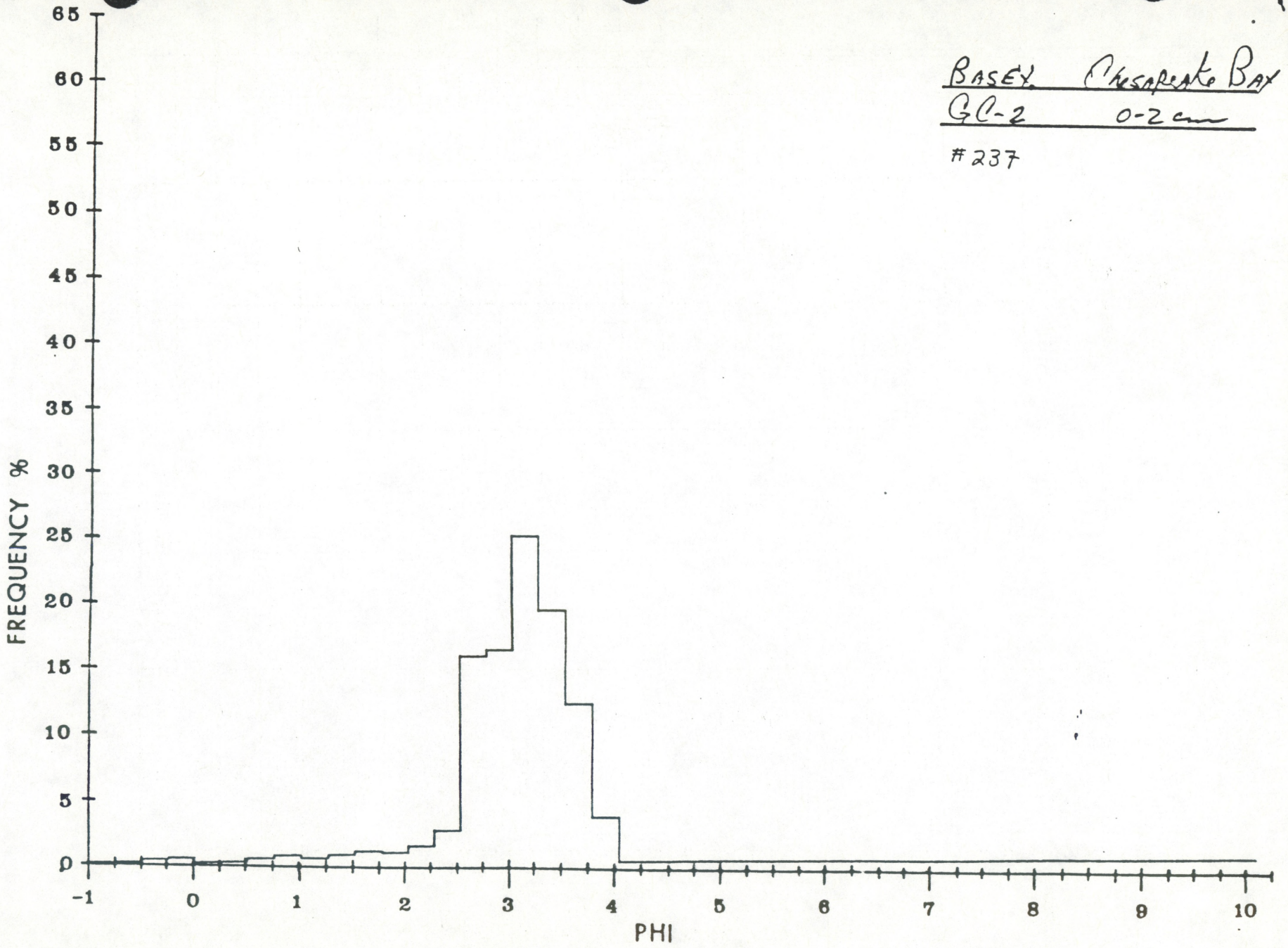

Basin: Chesapeake

GC-2 6-8cm

238

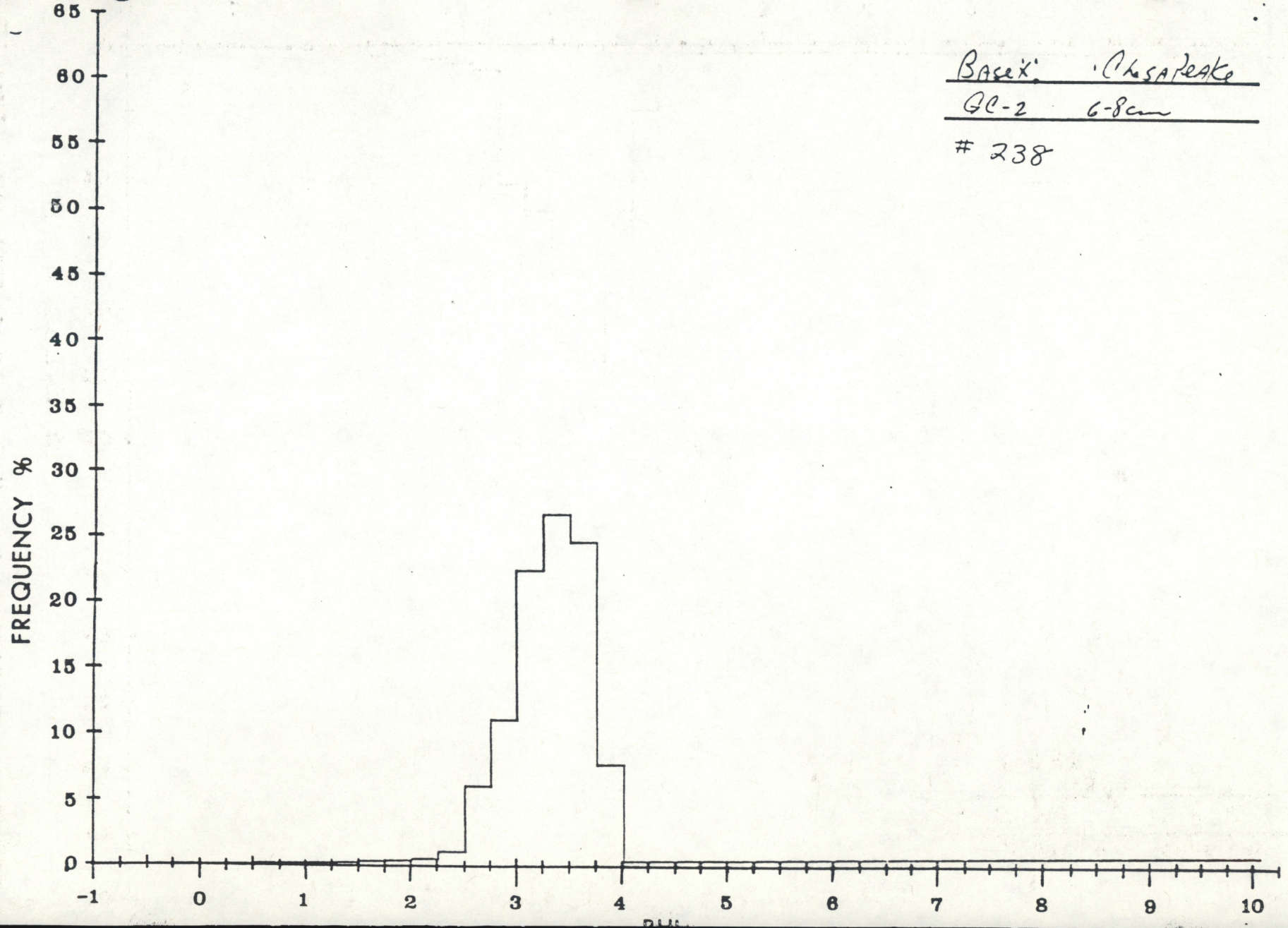

BASE X. Ches. Bay

GC-2 12-14 cm

239

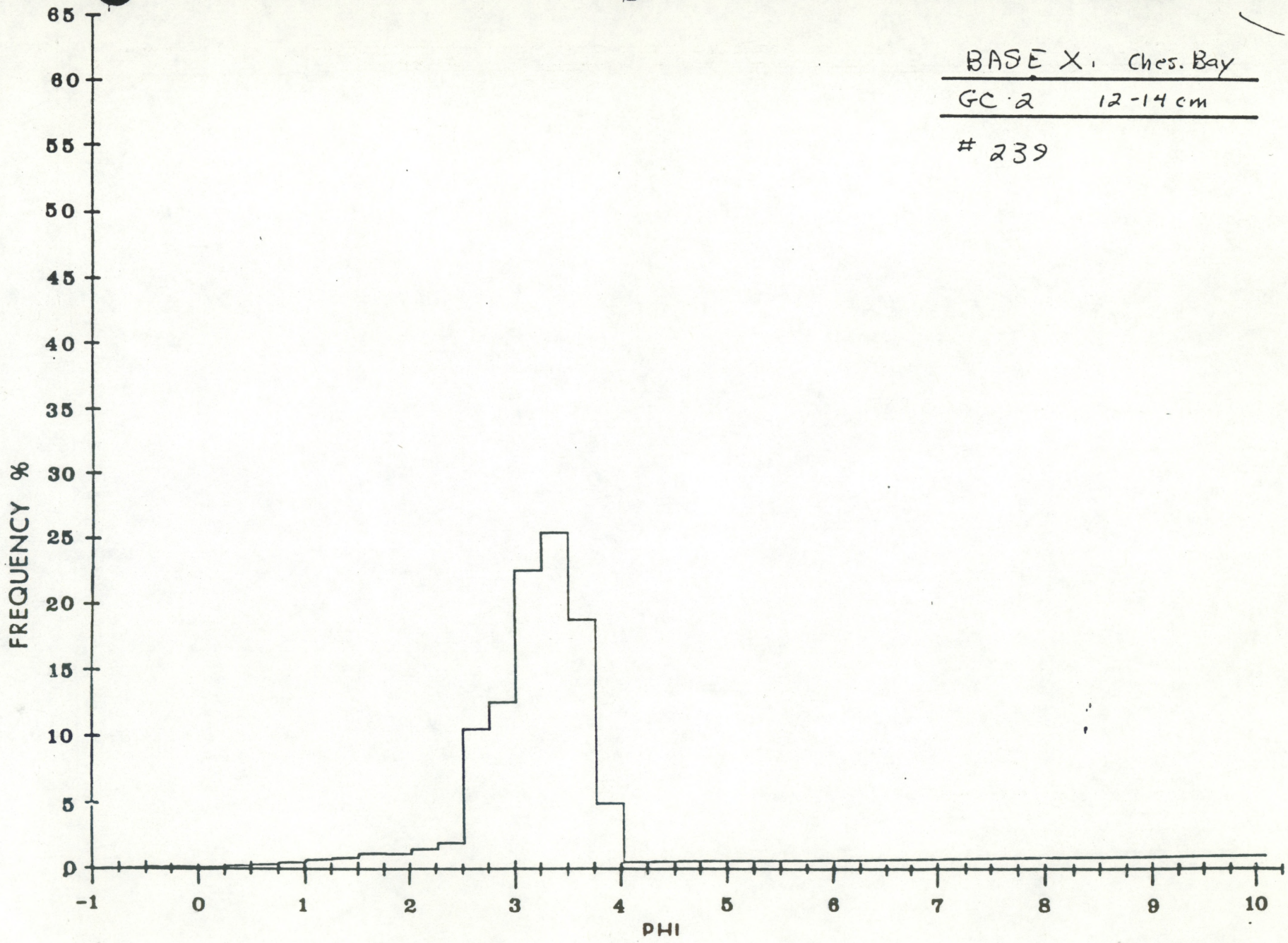

Base 'X' Ches Bay

GC 2 # 240

17 - 19 cm

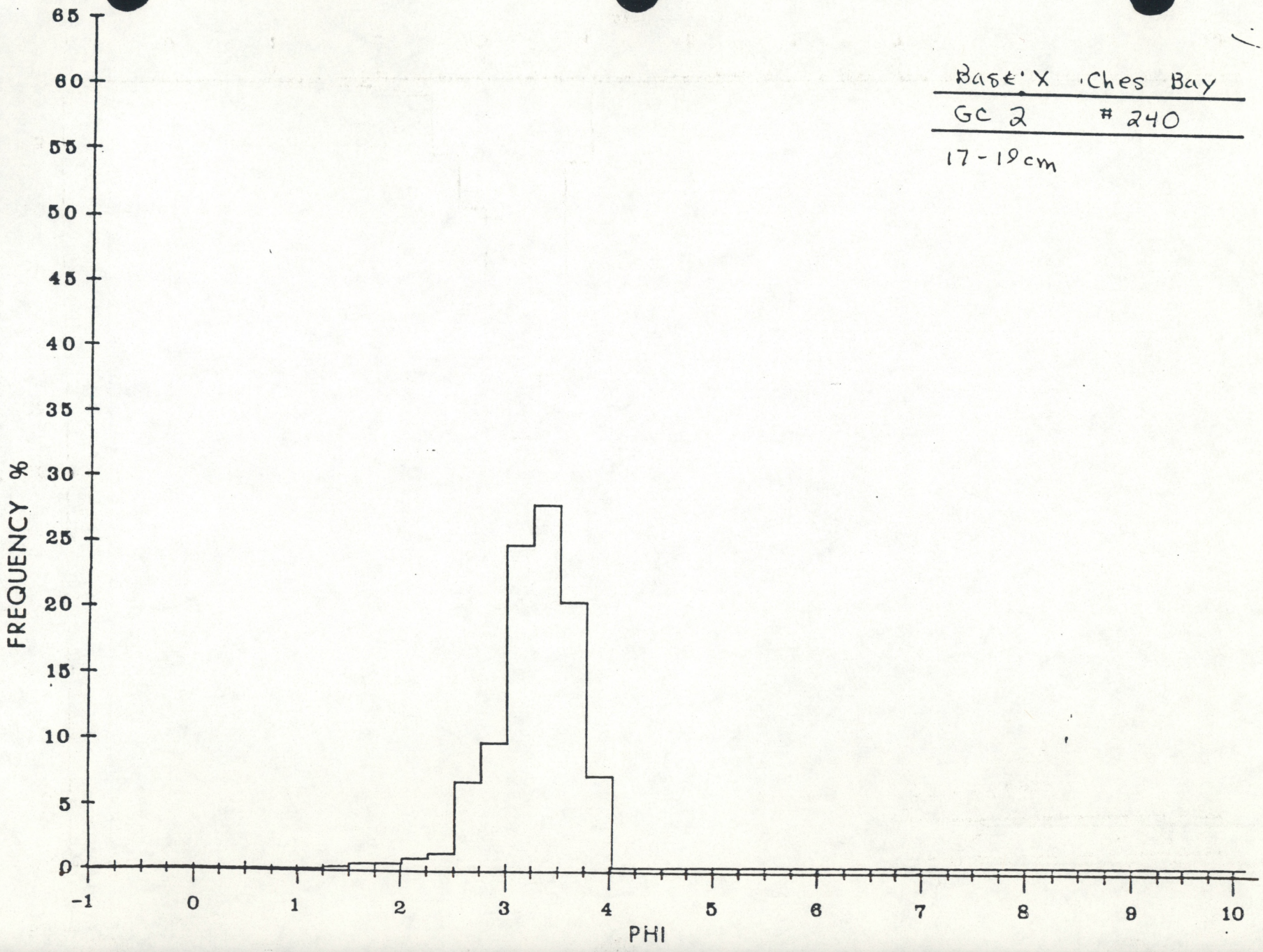

Base: X . Ches. Bay

GC 2 # 241

22 - 24 cm

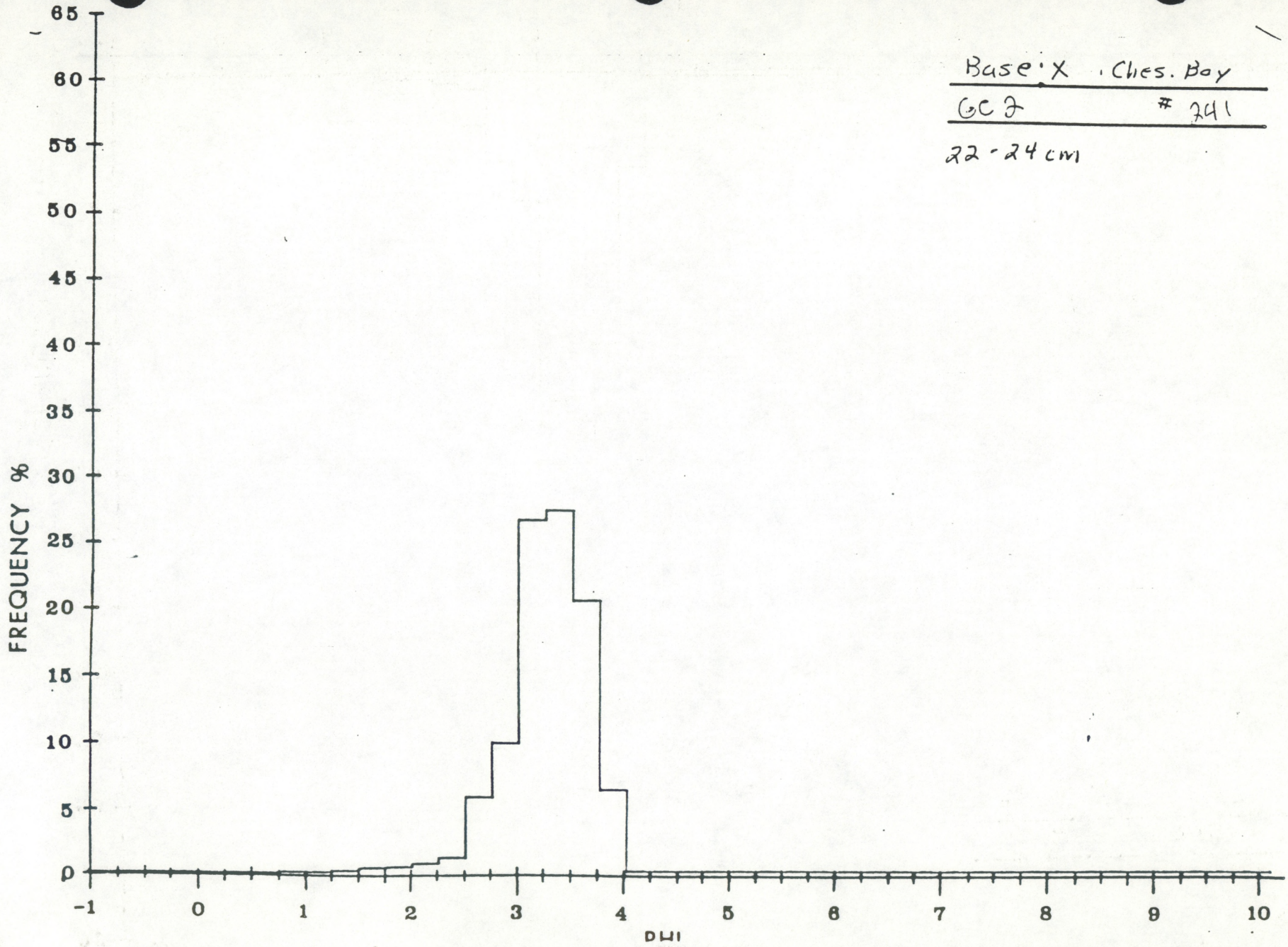

Base X
GC 2 Ches. Bay
27-29 cm #242

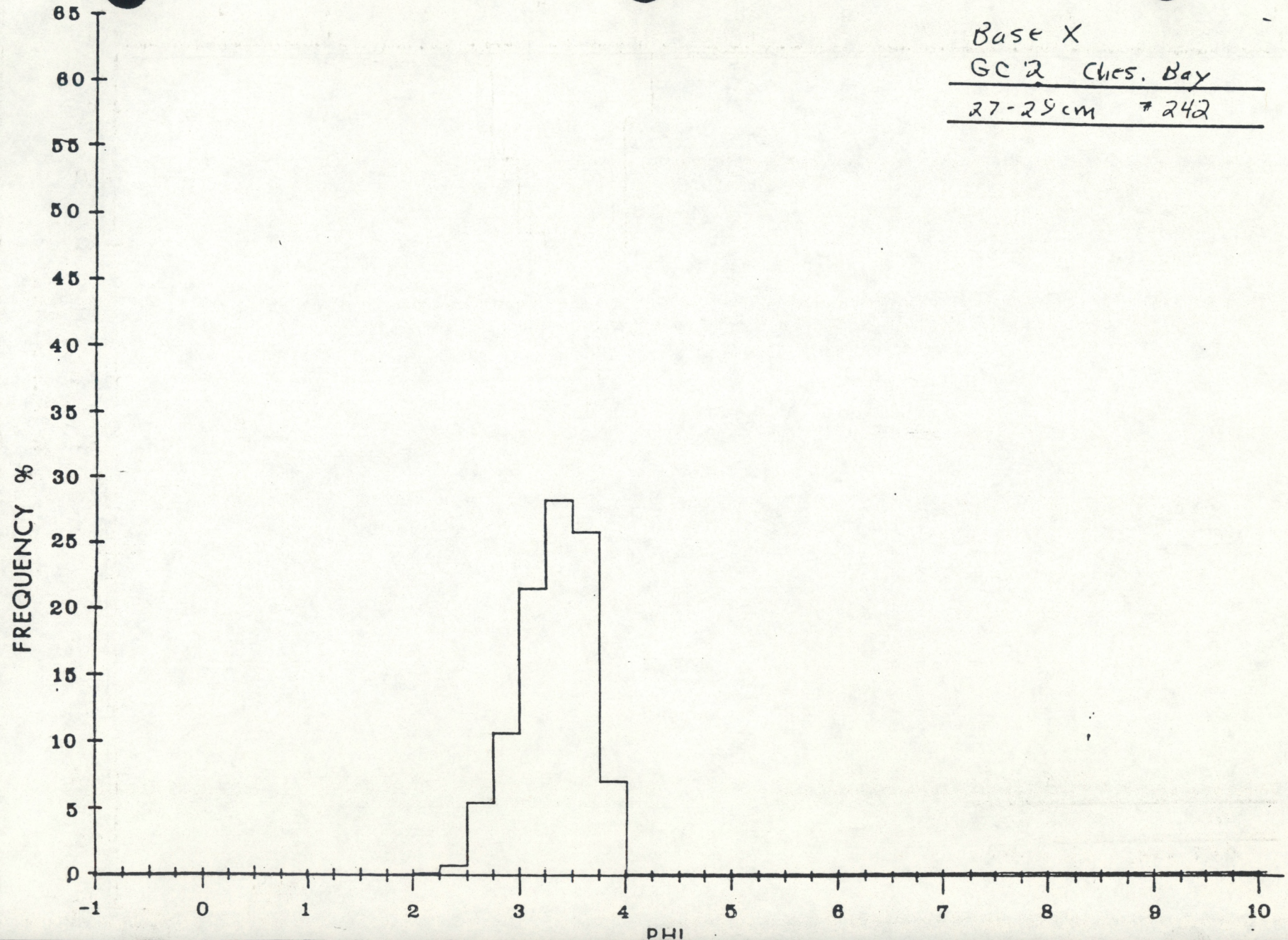

Base 'X Ches Bay
GC 2 # 244
37-39 cm

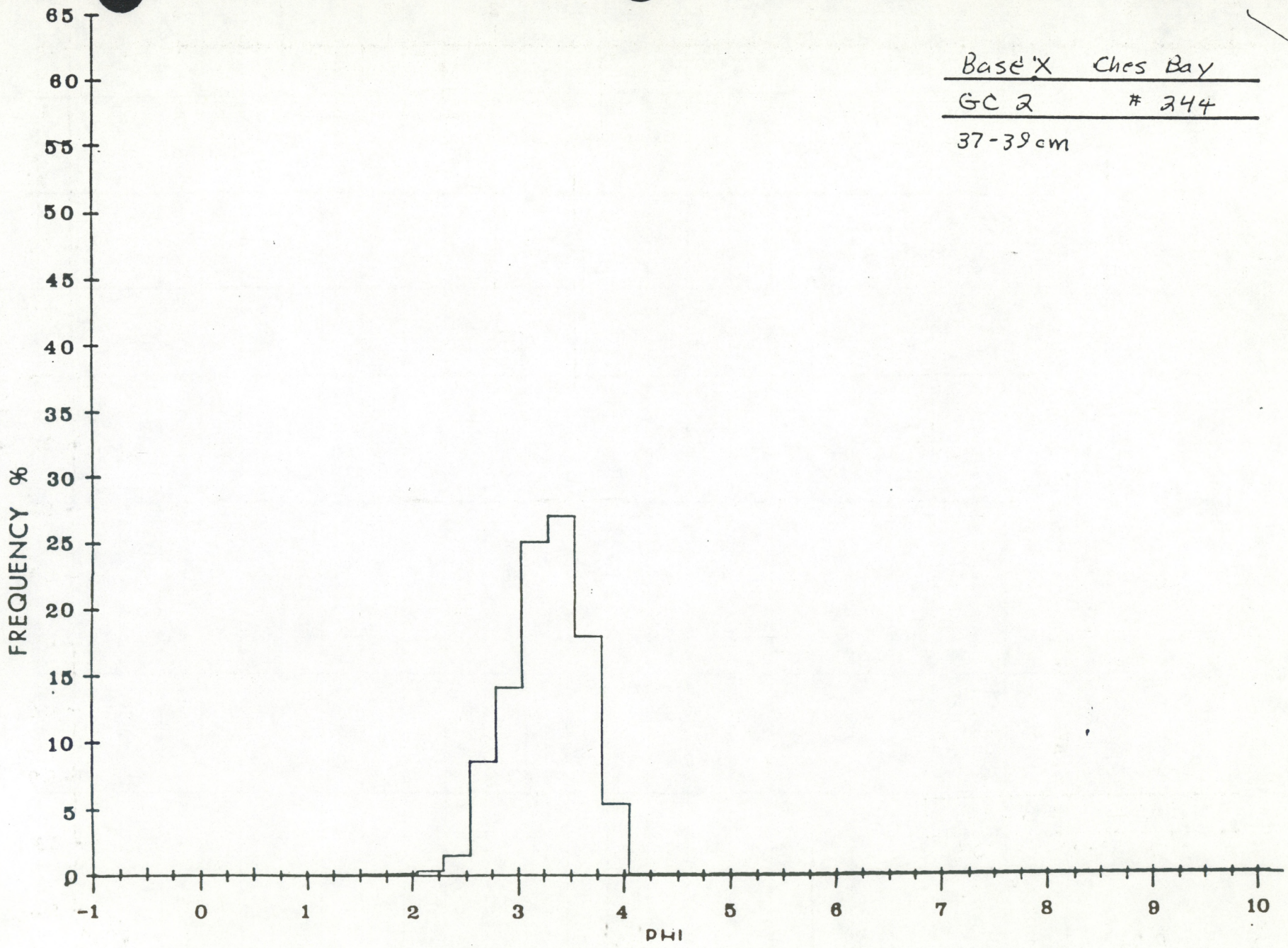

AOML OCD

GEOTECHNICAL / TEXTURE SUMMARY TABLE

PROJECT: BASE X
Dodge Island

CORE/SAMPLE: GC 3

DEPTH (cm)	WATER (%)	BULK DENSITY (g/cc)	POROSITY (%)	SAND (%)	FINE (%)	CARBONATE %	
						TOTAL	SAND
1-3	107.87	1.434	74.4	20.70	79.30	6.69	32.34
4-6	101.02	1.456	73.5	31.88	68.12	22.67	71.11
11-13	62.07	1.636	62.6	59.74	40.26	39.76	66.56
17-19	96.64	1.470	72.2	33.72	66.28	21.29	63.14

PROJECT: Base X CORE/SAMPLE: GC3
Dodge Island

PHI CLASS	MICRON SIZE	WEIGHT % PER 1/4 PHI CLASS INTERVAL 1-3	INTERVAL 4-6	INTERVAL 11-13	INTERVAL 17-19	INTERVAL
-1.0	2000	0.15	0.25	2.26	0.27	
-0.75	1690	1.19	2.14	5.28	1.68	
-0.50	1410	2.08	3.09	6.60	0.34	
-0.25	1190	1.79	2.85	4.72	5.21	
0.00	1000	2.38	3.56	5.09	3.53	
0.25	840	0.89	1.90	4.53	3.36	
0.50	710	1.79	3.33	4.72	3.87	
0.75	590	3.57	4.75	4.15	4.71	
1.00	500	3.57	3.80	4.53	4.54	
1.25	420	4.17	4.99	6.42	6.89	
1.50	351	4.76	6.65	6.42	6.39	
1.75	297	8.63	7.84	8.87	9.41	
2.00	250	8.04	6.65	8.49	8.40	
2.25	210	10.42	9.03	9.81	10.08	
2.50	177	7.44	5.46	4.91	5.55	
2.75	149	8.63	6.41	4.53	6.39	
3.00	125	5.36	4.51	2.64	3.87	
3.25	105	6.25	5.46	3.02	3.70	
3.50	88	5.66	5.23	1.89	3.19	
3.75	74	8.63	7.84	2.08	5.55	
4.00	63	4.76	4.51	1.32	3.36	

BASE: Dodge Island

32-3 4-6 cm

#254

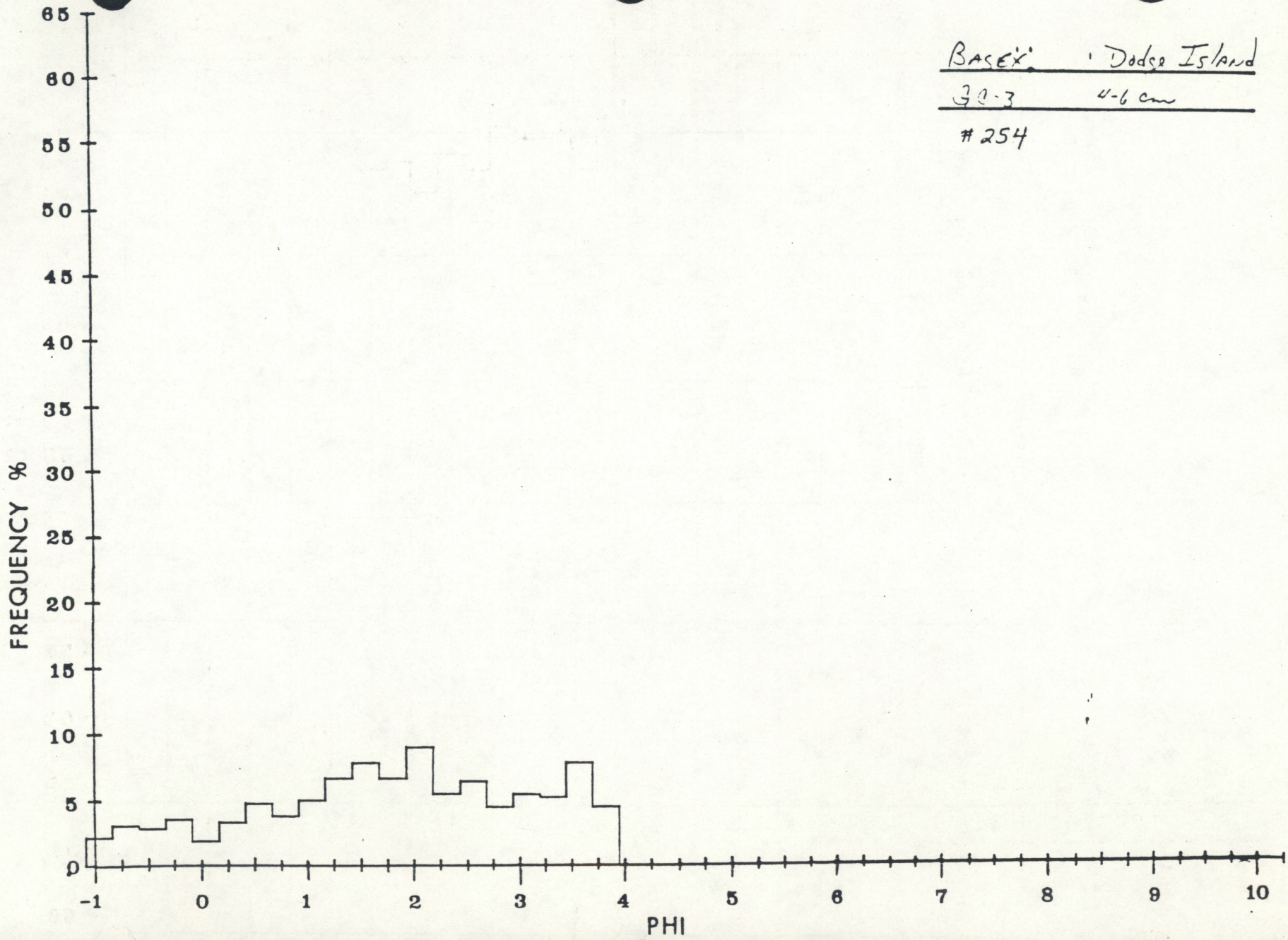

BASE: Dodd Island

G11-3 1-3 cm

#253

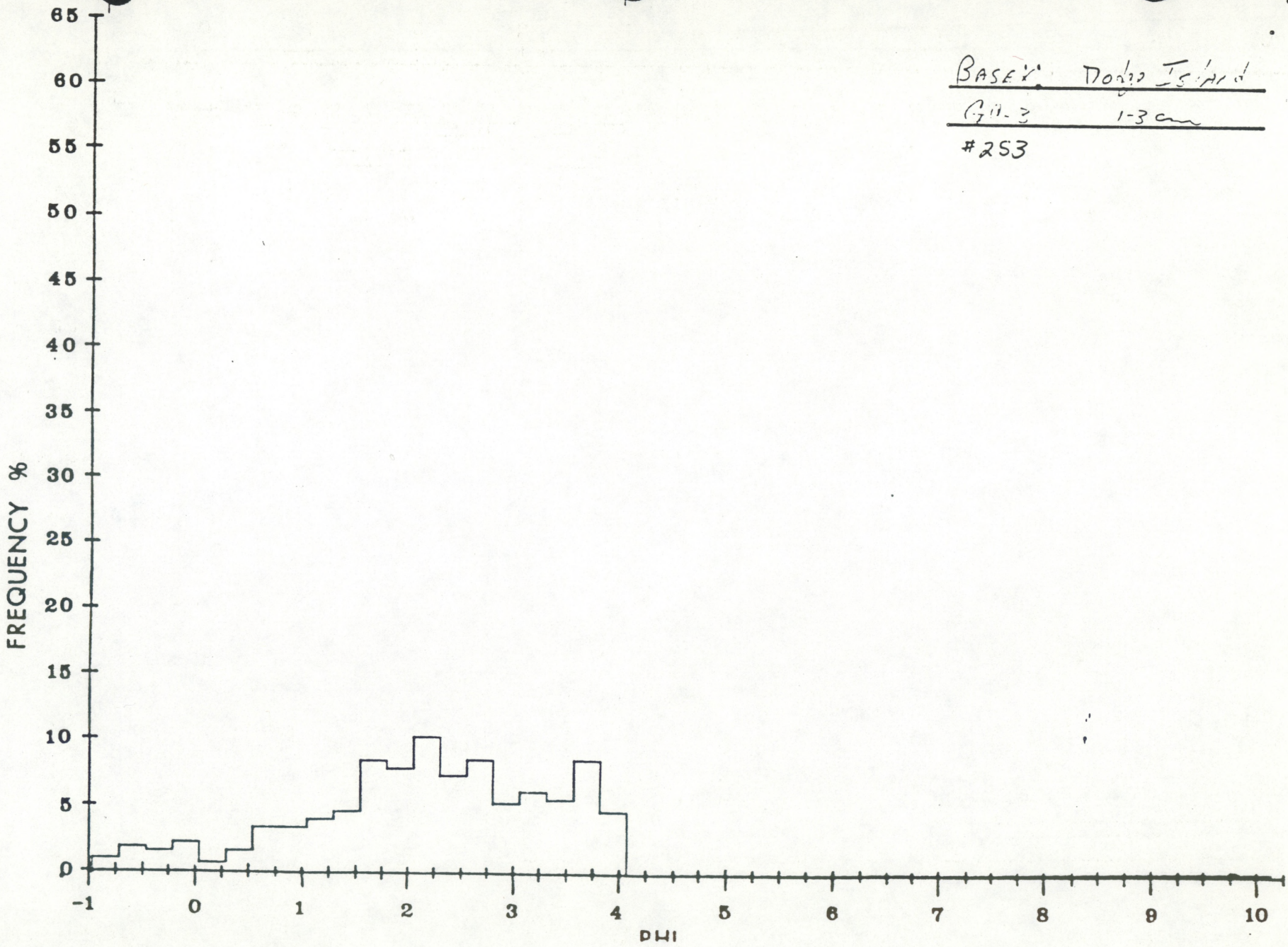

BASE X.

GC3: 11-13 cm

#255

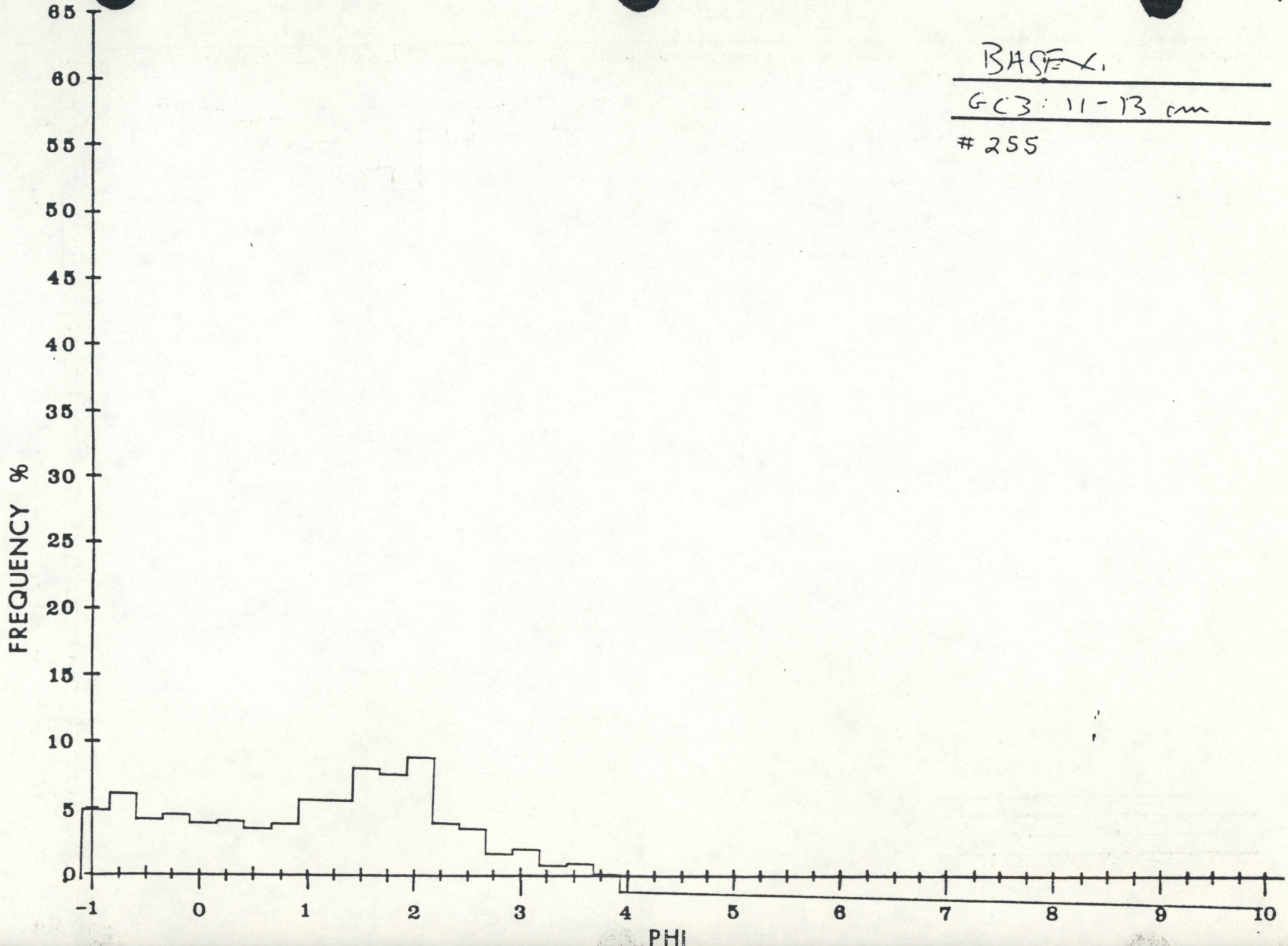

BASEY: Dodge I.

+?-? 17-Aug

#256